DISCRETE ELEMENT MODELING OF GEOGRID REINFORCED GRANULAR MEDIA

by

ASHEESH PRADHAN

Presented to the Faculty of the Graduate School of

The University of Texas at Arlington in Partial Fulfillment

of the Requirements

for the Degree of

DOCTOR OF PHILOSOPHY

THE UNIVERSITY OF TEXAS AT ARLINGTON

August 2015

Acknowledgements

I would like to begin this thesis by thanking my advisor Dr. Xinbao Yu for his incessant support and motivation in my research work. His analytical evaluations and constructive suggestions were of immense importance in guiding my work in the right direction to producing this result. I will ever be thankful for his eagerness to work with his students, “knock on my door any time” policy for students, and patience.

Also, I express my sincere gratitude to Dr. Anand Puppala for always being supportive towards me and his friendliness towards his students regardless of his excellent achievements and stature.

I also thank Dr. Haiying Huang and Dr. D. J. Seo who are my committee members. I thank them for providing valuable suggestions in better organizing my research work, and possible improvements.

I also thank several of my colleges and friends Brett DeVries, Nan Zhang, Felicia, Dipak Tiwari, Raju Acharya, Ujwal Patil, Aravind Pedrala, and Tejo Vikash Bheemasetti for valuable discussions I had with them. I specially thank Tejo Vikash Bheemasetti for his professional and personal support.

March 30, 2015

Abstract

DISCRETE ELEMENT MODELING OF

GEOGRID REINFORCED

GRANULAR MEDIA

Asheesh Pradhan, PhD

The University of Texas at Arlington, 2015

Supervising Professor: Xinbao Yu

Geogrids have proven to be economical solution in improving ground conditions for construction in foundations, retaining walls, railway tracks, and pavements. Hence researchers have started studying the geogrid reinforcement in detail to understand the working of geogrid and parameters affecting it. Following the advent of faster computers and efficient algorithms researcher have started using discrete element method (DEM) to study geogrid reinforcement since DEM provides particulate level of interaction and understanding and is the closest resemblance of the physical phenomenon. However, the research works are widely spread lacking comprehensive review of factors that can affect such models. This research studies geogrid reinforcement experimentally by testing geogrid reinforced glass beads in a triaxial setup and develops a 2D DEM model to establish important effect factors. By comparing the trends of the data obtained from the experimental and numerical simulations, the study provides conclusions and recommendations.

Table of Contents

List of Illustrations

List of Tables

Chapter 1

Introduction

1.1. General background

Geogrids are used in civil engineering construction projects for increasing the strength of soil in pavement construction, railway tracks, retaining walls, mechanically stabilized walls and foundations where granular soils are used (Zornberg and Gupta) . Their chief contribution is sought into decreasing use of construction materials and maintenance cost and increasing load bearing capacities of such structures. The increase in strength is due to several factors which involves complex interaction between geogrid and soil. Hence the understating of such factors is of immense importance in developing efficient geogrids and designing improved reinforced systems.

Discrete Element Method known as DEM in short is being used in understanding the interaction between geogrid and soil elements. DEM is gaining its popularity in this particular modeling as the interaction between the geogrid and soil is basically particulate in nature. With developing DEM algorithm and computer efficiency more complex models of geogrid reinforced soil systems have become possible. Many researchers have been working in understanding such complex systems but due to plethora of factors involved it is impossible to encompass all of them in one work. However, it is also important to understand basic parameters such as reinforcement mechanisms in two dimensions (2D) and three dimensions (3D), loading rates, boundary types, and particles shapes that can significantly affect a DEM model.

1.2. Scope of work

This research work aims at understanding the behavior of geogrid reinforced 2D DEM samples. The understanding obtained from the work is expected to be applicable to modeling of any reinforced granular material. Behavior of reinforced samples were

studied at both macro and micro level meaning, bulk behavior and particulate level behavior were studied. More emphasis was placed on understanding the reinforcement phenomenon than on direct modeling. The thesis explains works performed with the following scopes.

(a) Perform experimental works to aid numerical model.

(b) Develop an understanding of how basic parameters such as loading rates, boundary types, and particles shapes affect a DEM model.

(c) Understand the effect of abovementioned parameters on a geogrid reinforced 2D DEM sample.

(d) Understand the reinforcement mechanism of geogrid in 2D DEM sample.

(e) Compare experimental results and 2D models for trends

1.3. Thesis outline

Chapter 1 discusses the general background of the research work and the scope of the work. It also presents the structure of the thesis.

Chapter 2 discusses pertinent literature available in the numerical modeling of geogrid reinforcement. The chapter also provides general background into the concept and evolution of Distinct Element Method (DEM) along with some pertinent specifics of the commercial software that was used in the research.

Chapter 3 explains the experimental testing program undertaken and the rationale behind it.

Chapter 4 provides the numerical simulations performed and the results obtained in terms of micro and macro behavior. It also draws brief comparison between the experimental works and numerical modeling.

Chapter 5 concludes the dissertation discussing chief points that were observed during the research work and provides further recommendations and improvement for further research work.

Chapter 2

Literature review

2.1 Introduction

Distinct element method (DEM) has now become a multidisciplinary subject and is used in areas such as geotechnical engineering to study granular soils, pharmaceuticals for handling and processing powder, in agriculture for handling grains and design of efficient silos, in mining industries to study slopes and rock topples, for example. As such there are ever increasing researches being performed using DEM models with equal number of scientific papers being published.

Due to such large volume of scientific papers in such multidisciplinary areas, it is beyond the scoped of this research to include them all comprehensively. However, it is imperative that researches that are pertinent to this research are reviewed in this section. Additionally, DEM modelling being relatively new application in geotechnical problem solving and analysis, a brief review of the fundamental idea in DEM modelling have also been provided.

The literature review will be structured with four parts with brief introduction to DEM, followed by specific introduction to the PFC2D and PFC 3D. The third part will discuss pertinent research works briefly.

2.2 General background

2.2.1 Evolution

Distinct Element Method or Discrete Element Method, DEM in short, was first proposed by Cundall in 1971 with application in rock mechanics. The theory was later applied to soils in 1979 by Cundall and Strack (Itasca Consulting Group 2008).

Most of the researches involving DEM is in non-cohesive material as in granular soils and rock toppling. In soil DEM is mostly suitable in modeling problems involving

granular soil with particle sizes of more than 100 micro meters at which inertial forces dominate (O'Sullivan 2011).

2.2.2 Particles

As the name suggests, a fundamental unit in DEM is a particle. Particles in general to be used in DEM can of any shape. Intuitively, a disc would the simplest representation of a particle in two dimensions, in short 2D and likewise a sphere in three dimensions, in short 3D. These are simplistic shapes in such 2D and 3D dimensions based on the ease of detecting contact between such particles. More complex shapes are possible increasing complexity of model. Because of simplicity of using disc or spherical particles and most researches are sufficed by such particles, discs in 2D and spheres in 3D DEM modelling are post popular.

More complex shapes are possible in DEM. Simple shapes such as discs and spheres can be combined in different ways and numbers to represent complex shapes (Ferellec and McDowell 2010; O'Sullivan 2011). Figure 2-1 is a scanned 3D image of an aggregate particle. A DEM representation was created for the 3D image with spherical particles, several spherical particles combined together to represent the surface texture and undulations. Due to advanced techniques of 3D scanning and digitization soil particles can be scanned and their representative numerical model can be used in modeling (O'Sullivan 2011; Tutumluer et al. 2012).

Figure 2-1 3D image

Figure 2-2 DEM sample

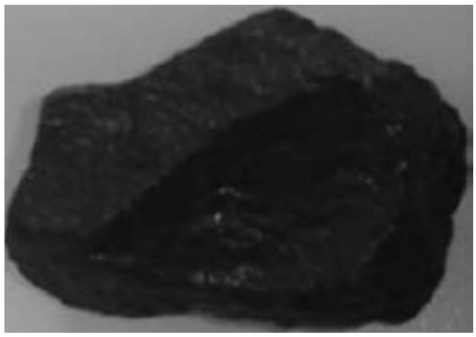

Figure 2-3 Ballast particle

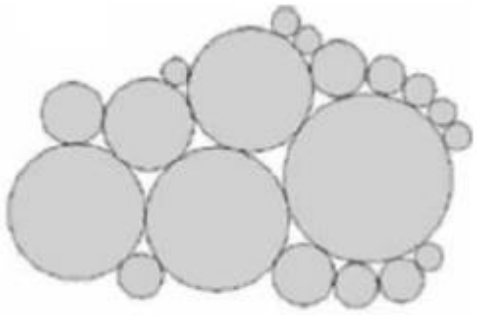

Figure 2-4 DEM representation

Figure 2-1 Scanned image of real ballast particle, Figure 2-2 DEM representative image with several number of small spheres combined (Ferellec and McDowell 2010); Figure 2-3 Ballast particle passing 53 mm and retained on 45 mm sieve, Figure 2-4 2D DEM representation of the ballast in Figure 2-3 with several circular particles combined together (Indraratna 2010).

2.2.3 Particle properties

Particle can be attributed with certain physical properties in DEM models. These properties are mainly of two types – geometrical properties and physical properties. Properties that can be assigned to particles can be but not limited to as follows.

- Geometrical properties such as radius
    - Radius

        - Diameter
        - Major and minor axes for elliptical particles
- Physical properties
        - Density
        - Stiffness
        - Coefficient of surface friction
        - Shear modulus
        - Coefficient of restitution

The geometrical properties can change according to the shape and size of particles used. The physical properties are dependent on kind of model to be set up which in turn depends on the desired behavior of model such as properties associated with non-linear behavior of discrete particles are null and void when modeling with linear behavior for example. The physical properties can be assigned to particles by calibrating the model by the process of indirect modeling or by directly specifying the properties based on laboratory measurements by the process called direct modeling (Chung and Ooi 2007; Johnstone 2010).

2.2.4 Contact Models

Contact models define how the particles interact with each other and with other elements that are present in a model including the geometric and physical properties prescribed to the particles. These contacts come into existence when particles are in contact with each other however, the contact always is not physical contact. Particles can be considered in contact when they are at certain predefined distance from each other or overlapping. A simplistic linear model can be conceived of two particles connected by a linear spring system as in Figure 2-5, for example. In Figure 2-6 and Figure 2-7 'F' is the force generated in the spring due to compression or tension and δ is the displacement.

Several different types of contact models are being used by researchers such as linear model and Hertz-Mindlin and Deresiewicz model, a comparison between which has been provided by Renzo and Maio (Di Renzo and Di Maio 2004).

Figure 2-5 Contact model

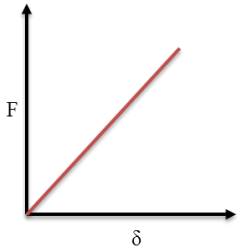

Figure 2-6 Linear Force development

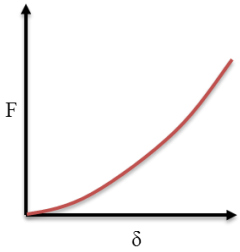

Figure 2-7 Nonlinear force development

Figure 2-5 Contact model with a spring; Figure 2-6 Force vs displacement relationship if the spring in Figure 2-5 is linear; Figure 2-7 Force vs displacement relationship if the sprint in Figure 2-5 is nonlinear.

Several possible scenarios exist for particle-particle interactions. Particles can move towards each other and overlap pushing into each other. Particles can interact in shearing where contacting particles move along each other in opposite directions or roll against each other causing shearing. Forcers developing between interacting particles have characteristic according to the defined contact models. For example the force developed between the particles can be linear as in Figure 2-6 or nonlinear as in Figure 2-7 if the spring is nonlinear. As discussed previously such linear and nonlinear force and displacement relationships are possible in shearing direction also.

2.2.5 Boundary

Boundary confines DEM particles in a model or defines the extent of a DEM model. Boundaries are also used in introducing changes in model such as application of

load or deformation. Walls and DEM particles themselves can be used as boundary. Boundary can be periodic too.

2.2.6 Operation

DEM simulation operates on cyclic operation cycle that typically includes the following in a cyclic order after creations of particles.

- Detection of particles
- Finding contacts between particles
- Calculate forces acting on particles due to inter particle interaction
- Find the resultant forces acting on particles due to forces applied externally and interparticle interaction
- Move particles according to the resultant forces acting on them
- Update positions of particles
- Repeat the process by detecting the particles again

2.2.7 PFC2D and PFC3D

This section briefly introduces the commercial DEM software used in the research. A detailed elaboration about the software elements pertaining to the model used in the research will be explained in related sections while discussing the models. However, detailed explanation of every aspect of the software is not provided as it is not the objective of this manuscript.

PFC2D and PFC3D are commercial DEM software in two dimensions and three dimensions respectively from Itasca Consulting Group. This research used version 4.0 for both 2D are 3D. These software has been classified as distinct element code and are specific application of DEM. In future texts PFC will be used in general discussion referring to PFC2D and PFC3D for version 4.0 used in this research.

2.2.8 PFC2D and PFC3D elements

PFC has two major elements – particles and walls. The basic particle shape possible in PFC is a disc or a sphere in two dimensions and a sphere in three dimensions. In PFC2D there exists possibilities of using either discs/cylinders or spheres. If discs/cylinders are used they are of unit length into the plane of viewing as shown in Figure 2-9. If spheres are used the spheres are aligned such that their centroids are aligned on a vertical plane as shown in Figure 2-10. In both the cases the view of such particles would be only circular in orthogonal as shown in Figure 2-8. Figure 2-11 shows random particle assembly of spheres in PFC3D.

Figure 2-8 PFC2D view of particles

Figure 2-9 Cylinders/Discs in PFC2D

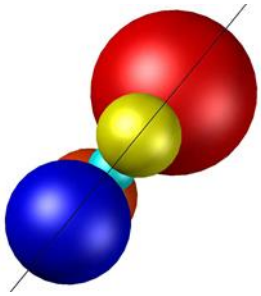

Figure 2-10 Coplanar spheres in PFC2D

Figure 2-11 Spheres in PFC3D

More complex shapes are possible in PFC by combining particles together. When the particles are combined together they can be joined with breakable or unbreakable bonds. Particles joined with unbreakable bonds are called clumps and are considered rigid body where the constituent particles do not break away from each other irrespective of forces acting on them. Lu and McDowell approximated a single railway ballast with ten larger balls clumped together in pyramidal shape with eight smaller balls joined to the pyramidal group as asperities as shown in Figure 2-12. The clumped balls do not break apart from each other whereas the smaller balls representing asperities

break away from the larger balls when subjected to certain force. Particles can be attributed with properties such as discussed in section 2.2.3.

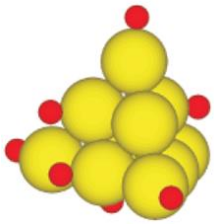

Figure 2-12 DEM approximation of a single railway ballast with a clump and breakable asperities (Lu and McDowell 2010).

Walls are another important element in PFC. Walls can be used as boundary for confining particles and loading samples in terms of application of displacements. Walls can be attributed with several properties except mass. Hence walls do not have inertia in PFC. However, particles can themselves be used as boundary and are capable of applying force too whereas walls can be used for applying load in terms of displacement only.

2.2.9 Contact approach in PFC

PFC uses soft contact approach. There are generally two main contact approaches in DEM. Soft contact approach and hard contact approach. In soft contact approach as in PFC particles are allowed to overlap each other for a small distance which results in generation of contact forces based on contact models used. In hard contact approach particle do not overlap and contacts between particles are instantaneous. Hard contact approach is suitable for modeling dilute systems like gas particles with binary collisions. However, in soil there are several particles in contact with one particle at a time and hence soft contact approach is more suitable in the latter case (Itasca Consulting Group 2008).

2.2.10 Contact Models

PFC has built in linear and nonlinear contact models. In linear contact model particle interactions are assumed to be linear in behavior with linear springs in normal and tangential direction as shown in Figure 2-5 and force has linear relationship with displacement, displacement meaning the amount of overlap between particles represented by δ in Figure 2-13.

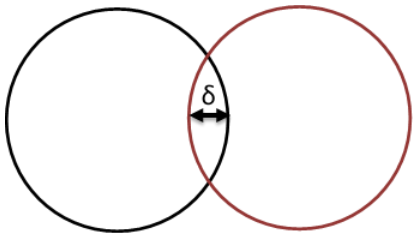

Figure 2-13 Overlap between particles.

Hertz-Mindlin is a nonlinear contact model built into PFC. This model is mostly used in simulating dynamic systems as opposed to linear model which is used in quasi static models.

Particles can be bonded together in PFC in different ways as follows.

- Clumping
- Contact bond
- Parallel bond

Figure 2-14 Normal stiffness

Figure 2-15 Contact bond model

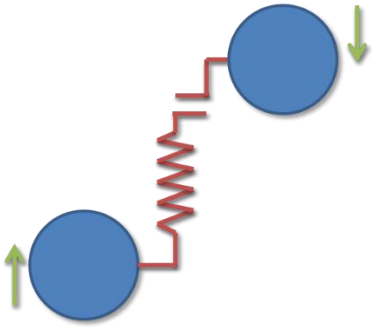

Figure 2-16 Shear contact model

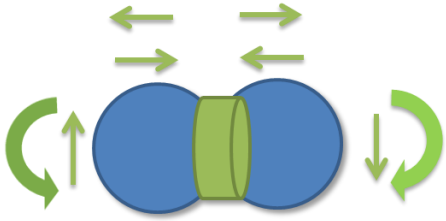

Figure 2-17 Parallel bond model

As described in section 2.2.8 particles can be combined or joined together by clumping where they do not break away from each other. Another way of joining particles together in PFC is by using contact bond. In contact bond particles are envisioned to be joined together by an imaginary rubber band. When particles joined as such move away from each other they develop tension forces between them. A third way of joining particle is by using parallel bond. When there are no contact bonds between particles they interact as shown in Figure 2-14 and Figure 2-16. The particles develop compressive forces when they overlap each other as shown in Figure 2-6 or Figure 2-7 but do not develop any tension force. Similar is the interaction between particles in such case when they move in shearing direction as in Figure 2-16. When a contact bond is installed between particles they develop tension force as in Figure 2-15 in conjunction with the model in Figure 2-14 and Figure 2-16. Contact bond however, does not resist moment and hence particles can roll over each other. Parallel bond on other had can resist moment and develop tension forces as well. Parallel bond is envisioned as an extra

material that holds together connected particles and has certain cross sectional area providing bending stiffness as see in Figure 2-17.

2.2.11 PFC calculation cycle

PFC calculation cycle is a cyclic calculation process in which contacts are detected, forces are applied, new positions are assigned, and contacts are detected again. During the cycling process changes can be introduced without interruption. In simplistic form the calculation cycle is similar to that discussed in section 2.2.6.

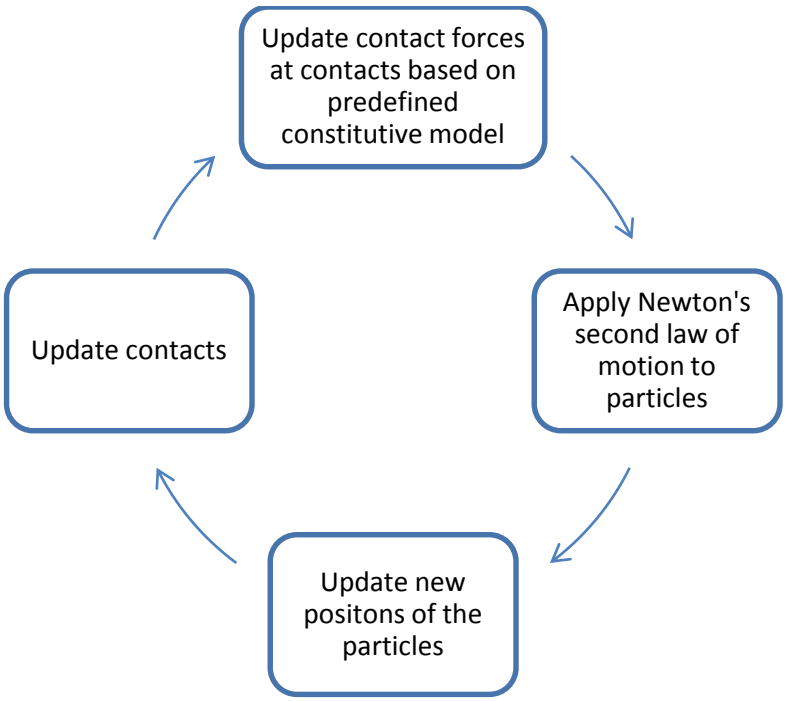

Figure 2-18 Calculation cycle in PFC

Figure 2-18 explains the calculation cycle in PFC. After particle creation contacts are detected. Base on the contacts forces are applied to particles and summed up with externally applied forces for resultant forces. The particles then move according to

Newton's second law of motion for a defined time step. At the end of the time step the positions of particles are updated again and so are the contacts.

2.3 Experimental study of geogrid reinforcement

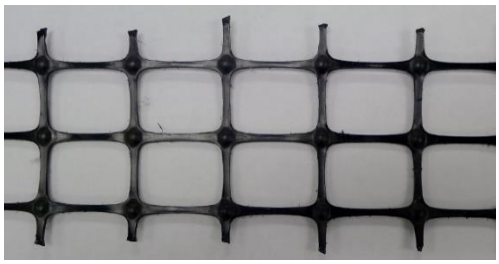

Figure 2-19 BX1100

Figure 2-20 Geogrid reinforcing aggregate (Geosynthetics 2015)

Figure 2-21 Geogrid reinforcement of railway ballast (Tensar 2015)

Figure 2-22 Geogrid reinforcement of backfill of retaining wall (Litertystone 2015)

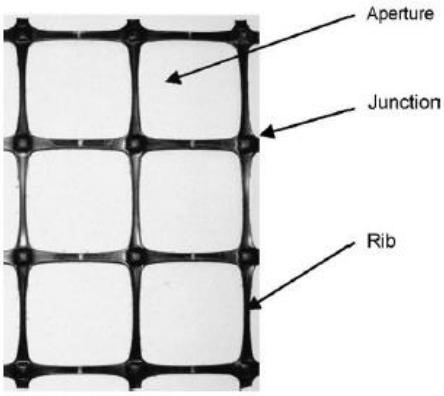

Figure 2-23 Technical description of geogrid structures (Brown et al. 2007)

Geogrid is a polymer with apertures that helps improve strength of soil for construction. Robert Koerner defines geogrid as ‘a geosynthetic material consisting of connected parallel sets of intersecting ribs with apertures of sufficient size to allow strike-through of surrounding soil, stone, or other geotechnical material (Koerner 2005).’ The specific definition of geogrid structural parts are shown in Figure 2-23. Figure 2-19 is a section of BX1100 geogrid from Tensar International Corporation and Figure 2-20 shows use of geogrid for reinforcing aggregates. Figure 2-21 and Figure 2-22 shows application of geogrid reinforcement in railway ballast and in retaining wall backfill respectively.

Holtz et al. mentions three ways geogrids and geotextiles provide reinforcement as follows.

- Lateral restraint as in Figure 2-24
- Increase in bearing capacity as in Figure 2-25 and
- Membrane effect as in Figure 2-26

Lateral restraint is due to the interlocking between reinforced soil and geogrid. The bearing capacity increase in soil comes due to the fact that presence of geogrid

modifies the shear failure envelope and force it to pass along the stronger and reinforced soil as in Figure 2-25. In membrane tension mechanism the geogrid or the geotextile acts as a structural support for load by transmitting the load along the geogrid itself as tension force. These reinforcement mechanisms are mobilized at different levels of deformation and in the context of present criteria of serviceability the lateral restraint mechanism of reinforcement is the most important (Zornberg and Gupta). In lateral restraint mechanism the particles and geogrid interact and interlock due to friction resistance between them and the interface is called ‘shear-resisting interface (Perkins 1999).

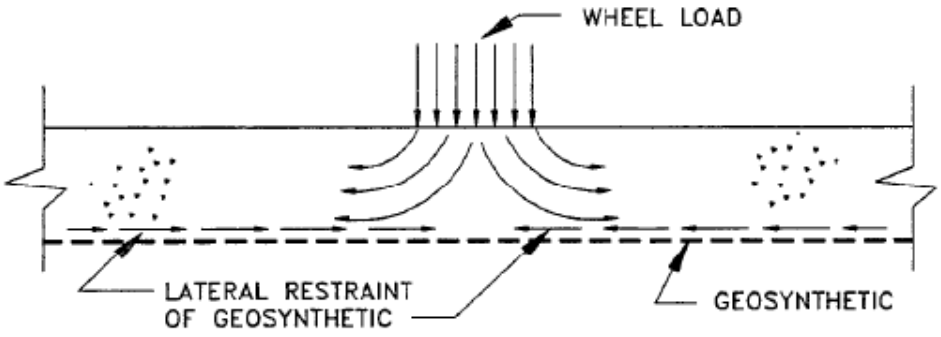

Figure 2-24 Lateral restraint (Holtz et al. 1998)

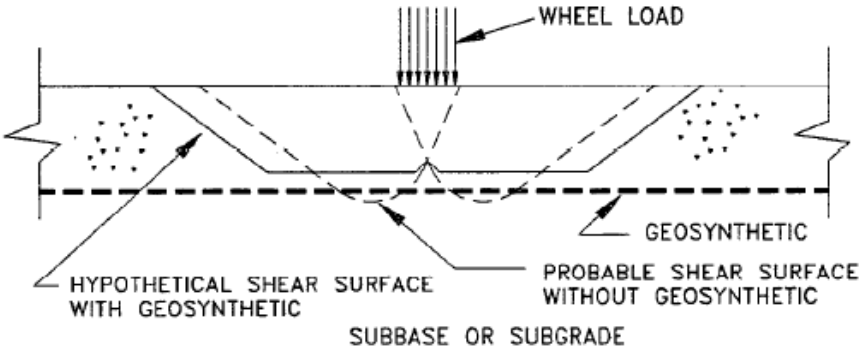

Figure 2-25 Bearing capacity increase (Holtz et al. 1998)

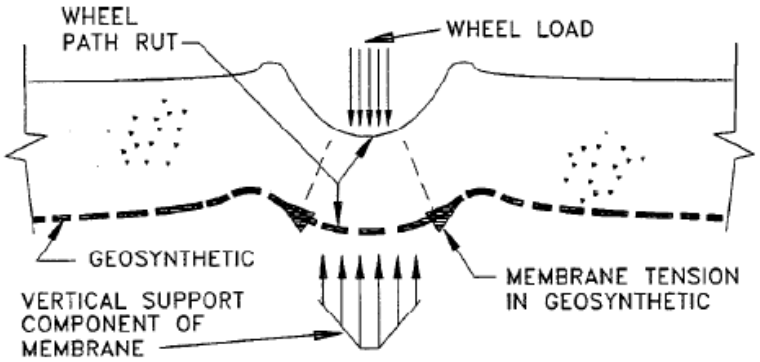

Figure 2-26 Membrane tension support (Holtz et al. 1998)

The behavior of geogrid reinforcement and geogrid reinforced aggregates have been extensively studied both experimentally and numerically. Experimental tests include various laboratory and filed tests in different scales. Laboratory test in element scale include direct shear box tests (Arulrajah et al. 2014; Bakeer et al. 1998; Palmeira 1987). Arulrajah et al (2014) studied the difference in interface shear strength of geogrid using standard and modified tests on construction and demolition aggregates with the modified tests yielding higher interface friction angle. The modified test sheared the sample 7 mm above the geogrid positioning to achieve higher peak and residual interface friction angle with the hypothesis that there is a stiffened zone present below the plane of shearing in standard direct shear test. Bakeer et al (1998) studied interface friction angle in light weight aggregates. Figure 2-27 and Figure 2-28 show the setup of bottom portion of direct shear test box and schematic of the setup respectively for work performed by Arulrajah et al (Arulrajah et al. 2014). Palmeria on the other hand studied scale factors along with geogrid reinforcement mechanism provided by various geotextiles.

Pullout tests were performed by Moraci et al (2006) and Wilson-Fahmy et al (1995). Moraci et al studied factors affecting pull out load in compacted granular soil such as reinforcement length and effect of dilatancy on pull out load. On the other had Wilson-Fahmy studied long term behavior of geogrid in pull out.

Triaxial tests were also performed to study the behavior of geogrid reinforced granular samples (Abu-Farsakh et al. 2012; Abu-Farsakh and Nazzal 2009; Chen et al. 2014; Indraratna et al. 1998) . Figure 2-31 and Figure 2-32 show triaxial set and triaxial sample of geogrid reinforced soil for the works performed by Abu Farsakh et al. in 2012. Abu-Farsakh et al (2009) and Abu-Farsakh et al (2012) studied the effect of geogrid type and location in a triaxial sample in a cyclic triaxial tests. Chen et al (2014) studied the

failure mechanism of geogrid reinforced mudstone triaxial sample with single and multiple layers of geogrids.

Researchers have performed large scale tests too using model box where geogrid sample is loaded using loading plates (Abu-Farsakh and Chen 2011; Qian et al. 2013). Qian et al (2013) studied performance of triangular aperture geogrids in terms reduction of settlement and vertical stress in the sample. Figure 2-29 and Figure 2-30 show the plate load testing box and schematic of the setup for testing geogrid reinforced sample for the works performed by Qian et al (Qian et al. 2013). Researchers have performed near filed condition load tests to evaluate performance of geogrid (Al-Quadi et al. ; Jersey et al. 2012). The works of Al-Quadi et al(Al-Quadi et al.) focused on studying improvement in thin flexible pavement due to geogrid reinforcement in terms of reduction in vertical stress and strains.

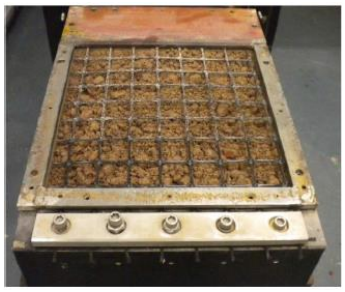

Figure 2-27 Lower half of shear box for modified direct shear test (Arulrajah et al. 2014)

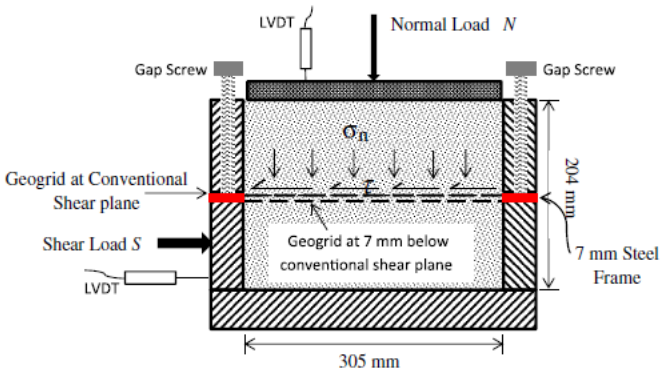

Figure 2-28 Shear box setup (Arulrajah et al. 2014)

Figure 2-29 Large scale plate load test box (Qian et al. 2013)

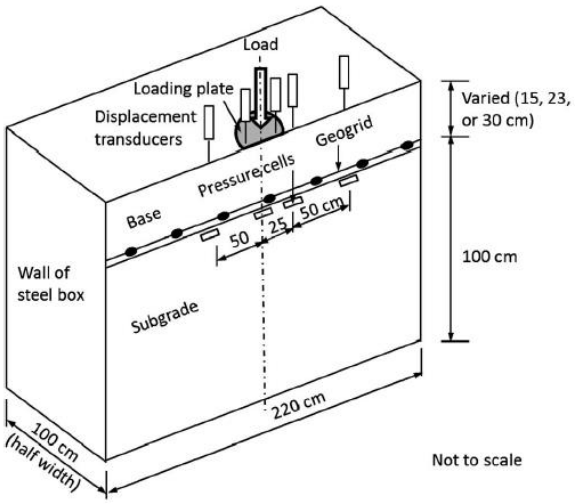

Figure 2-30 Plate load test box setup (Qian et al. 2013)

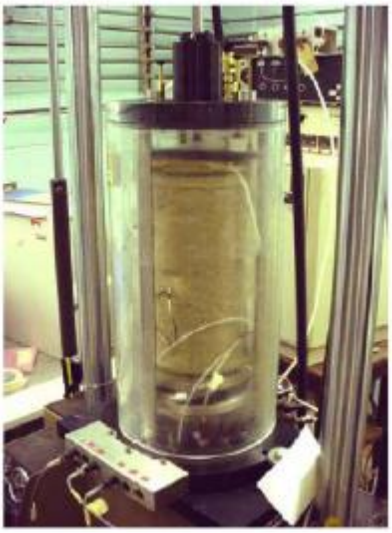

Figure 2-31 Triaxial testing set up of geogrid reinforced sample (Abu-Farsakh et al. 2012)

Figure 2-32 Geogrid reinforced triaxial sample (Abu-Farsakh et al. 2012)

An attempt to measure particulate level interaction of particle and geogrid in an experimental work was done by Schuettpelz et al(2009) in experimentally measuring the interlocking mechanism. The authors measured particle rotations along the elevation of a geogrid reinforced sample using microelectromechanical sensors (MEMS) using an experimental setup shown in Figure 2-33. P waves were generated at the surface of the sample which caused particle vibrations and the MEMS accelerometers placed along the elevation of the sample measure particle rotations. The measurement as can be seen in Figure 2-34 shows that the particle rotation in degrees, decreased in the adjacent vicinity of the geogrid.

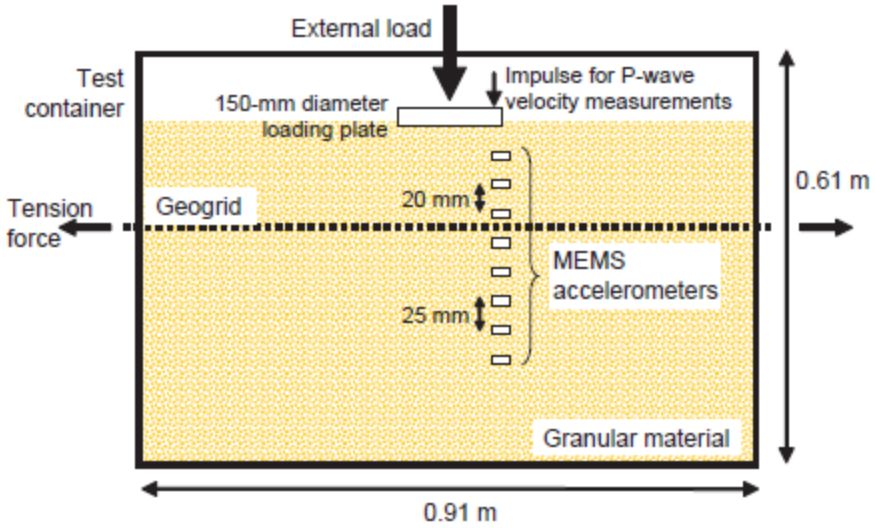

Figure 2-33 Schematic of test set up for measuring particle rotations

(Schuettpelz et al. 2009)

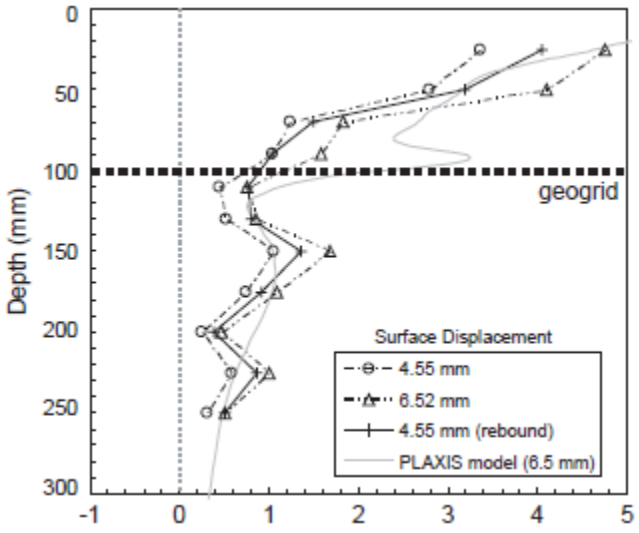

Figure 2-34 Rotation of particles along the elevation of geogrid reinforced sample (Schuettpelz et al. 2009)

Most of these laboratory small and large scale tests and field tests including several other tests mostly focused on the bulk behavior by observing loads, strains, and displacements which broadly included the following studies.

- Behavior of different types of geogrid such as biaxial and triaxial geogrids
- Behavior of geogrids based on flexural and rotational stiffness
- Performance of geogrids in different types of aggregates
- Difference in performance of geogrids evaluated using standard and modified test methods
- Factors affecting behavior of geogrid and geogrid reinforced samples
- Behavior of geogrid reinforced samples in static and cyclic loading conditions
- Volumetric dilation behavior of geogrid reinforced samples

These experimental studies draw conclusions on the behavior of reinforced samples and geogrids based on bulk behavior such as deviatoric stress versus axial or volumetric strain. These experimental studies bear the shortcoming in the study of fundamental mechanism of geogrid reinforcement, the interlocking effect. Additionally, the interlocking mechanism is a micro or particulate level interaction between soil and geogrid. As such any quantitative or qualitative measurement of such interaction is difficult to study in exclusively experimental works.

2.4 DEM study of geogrid reinforcement

Since the introduction of DEM in 1971 the number of publications using discrete element method have increased rapidly from few papers per year to 250 papers per year (O'Sullivan 2011) due to developments in DEM codes and computational efficiencies (Zhu et al. 2008). Currently several tens of thousands of particles can be simulated with some commercial DEM software with no limit for particle numbers as opposed to the capability of few thousand particles few years back (Ting et al. 1989). The chief computational effort in DEM simulation is invested in detecting contacts and as computers gain faster processors and large memories along with more efficient DEM algorithms the computational efficiencies increase increasing the ease of use of DEM. As such DEM has found research applications in wide areas that involve particulate media handling or processing such as manufacturing industries using hoppers, silos, and conveyor belt assemblies. However, the fundamental theory of modeling is common in all these applications. O'Sullivan (2011) has briefly described some development and applications in the field of DEM and Zhu et al (2007) has summarized theoretical developments in the application of DEM. A comprehensive review of theoretical development and application of DEM has been performed by Zhu et al (2008) describing several aspects of DEM sample preparation and processes acting on DEM samples

including particle-fluid interaction. However, limited number of papers have been published in studying geogrid reinforcement using DEM. Numerical models used in the study of geogrid reinforcement have mainly been DEM and finite element models. The study involved mainly static and cyclic triaxial and biaxial tests, and pull out tests in 2D and 3D.

Konietzky et al (2004) studied interlocking effects of geogrid using static and cyclic triaxial loading tests and pull out tests using three dimensional DEM. The 3D DEM models consisted of graded spherical particle assembly bounded with eight rigid vertical walls in octagonal shape as lateral boundary and horizontal walls on top and bottom as loading platens. The sample was tested with one and three geogrid layers, the geogrid being modeled with particles themselves. Figure 2-35 shows the particle size distribution of the DEM sample. The interlocking effect was evaluated in terms of a 'force ratio' called 'β' in the vicinity of geogrid defined as 'ratio of average force inside a brick, which covers in the horizontal direction the 4 intact meshes and a height of 2 cm to the average force in the same height interval but considering the full cross section.' Figure 2-37 is the DEM model of the geogrid used in the simulation. Figure 2-36 shows lower values of β at

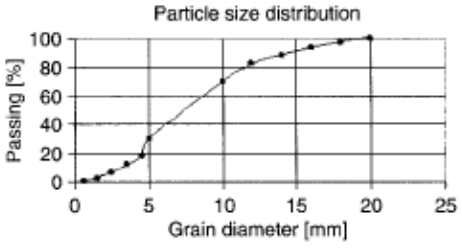

Figure 2-35 Particle size distribution (Konietzky et al. 2004)

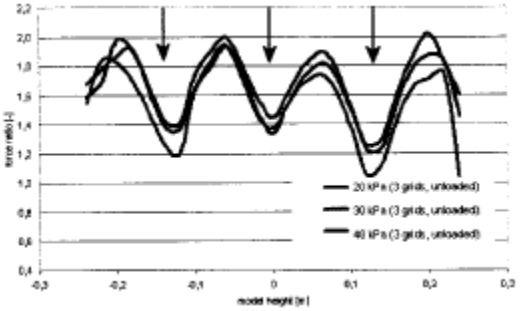

Figure 2-36 Force ratio along sample height (Konietzky et al. 2004)

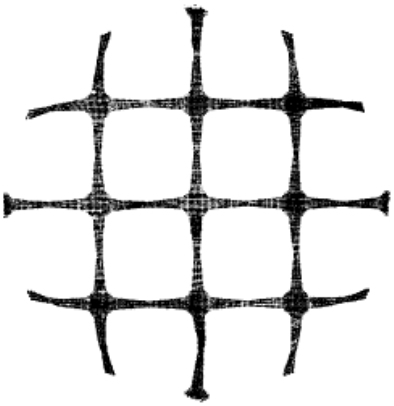

Figure 2-37 DEM model of geogrid (Konietzky et al. 2004)

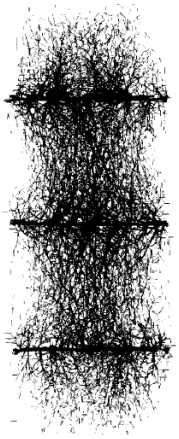

Figure 2-38 Contact force chain (Konietzky et al. 2004)

location of geogrids after partial unloading showing the presence of interlocking stress supported by the contact force chain diagram in Figure 2-38. The higher density of darker lines shows concentration of contact forces in the vicinity of geogrid. In terms of improvement the authors mention that the use of three layers of geogrid reduced radial and vertical displacement by approximately 50%. Similar reduction in settlement was observed using multiple layers in the triaxial test performed by Abu-Farsakh et al(2012). Similar work was performed by Chen et al (2012) using clumps shown in Figure 2-39 to represent aggregate particles in a box set up, the sides of the box being rigid walls, to test settlement of clump samples under cyclic loading conditions using biaxial (Figure 2-40) and triaxial geogrids. The geogrids were also modeled by bonding spherical particles together. The simulation was compared to results from a full scale 'Composite Element Test (CET)' apparatus. The experimental and numerical study revealed the fact that settlement was greatly reduced by using geogrid. However, the objective of the study was to find optimum location of geogrid in a box set up.

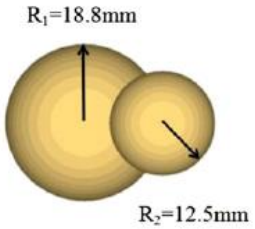

Figure 2-39 Clump made of two spherical particles

(Chen et al. 2012)

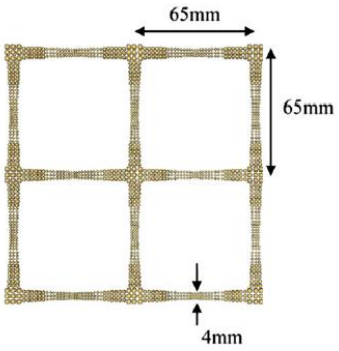

Figure 2-40 Biaxial geogrid model

(Chen et al. 2012)

Konietzky et al(2004), McDowell et al (2006), Ferellec and McDowell (2010), and Tutumluer et al (2012) studied geogrid reinforcement in granular soil using DEM model of pull out box. The pullout box consisted of four rigid vertical walls and top and bottom platens for loading. Konietzky and authors studied pull out using a 3D DEM model with rectangular parallelepiped sample with graded spherical particles. The study found that pull out load increased with increase in vertical load applied on the specimen. They also found out that with vertical load axial strain measured between front and end of geogrid increased which was in agreement with the experimental work performed by Moraci et al (2006). The sample displayed increased average contact force with higher vertical load and highest average contact forces during pull out for each vertical load. McDowell et al (2006) used similar set up but used clumped particles instead of single spherical particles shown in Figure 2-41. The particles were clumped by joining several spherical particles. The study showed results in agreement with that of Konietzky et al(2004). Further parametric study on the DEM model showed that increased thickness and stiffness of geogrid model caused peak load during the pull out to increase. The results were then compared to experimental test data with good agreement. However, the aim of the study

was not to investigate the effect of particle shape on geogrid reinforcement in pull out test. Ferellec and McDowell (2010) studied DEM model of pull out test using clumps to represent natural shape of aggregate more closely (Figure 2-42). The authors developed an algorithm to generate realistic shape by clumping several spherical particles with different sizes (Ferellec and McDowell 2010). However, the geogrid was modeled as a rigid structures and such that it did not experience any elongations but the fluctuation in the pull out load exhibiting formation of arching during pull out.

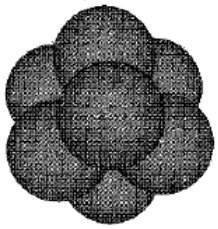

Figure 2-41 Clump particle (McDowell et al. 2006)

Figure 2-42 Clump particle representing realistic aggregate shape (Ferellec and McDowell 2010)

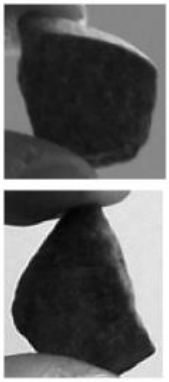

Figure 2-43 Aggregate used in experimental testing (Tutumluer et al. 2012)

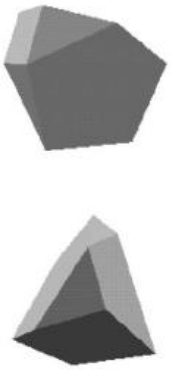

Figure 2-44 DEM representation of aggregate in 3D (Tutumluer et al. 2012)

Tutumluer et al (2012) studied geogrid reinforcement in direct shear box using experimental testing and DEM model. The authors used their proprietary DEM software to scan aggregates shown in Figure 2-43 in 3D and generate representative 3D model in DEM as in Figure 2-44. The DEM model was then used to study effect of aperture opening shape of geogrid with triangular and rectangular apertures. The results showed that triangular aperture provided higher pull out strength than rectangular aperture geogrid.

Biaxial testing of geogrid reinforced granular soils was carried out by Vinod et al (2011) in 2D DEM. The sample was set up in a rectangular box with rigid walls. The

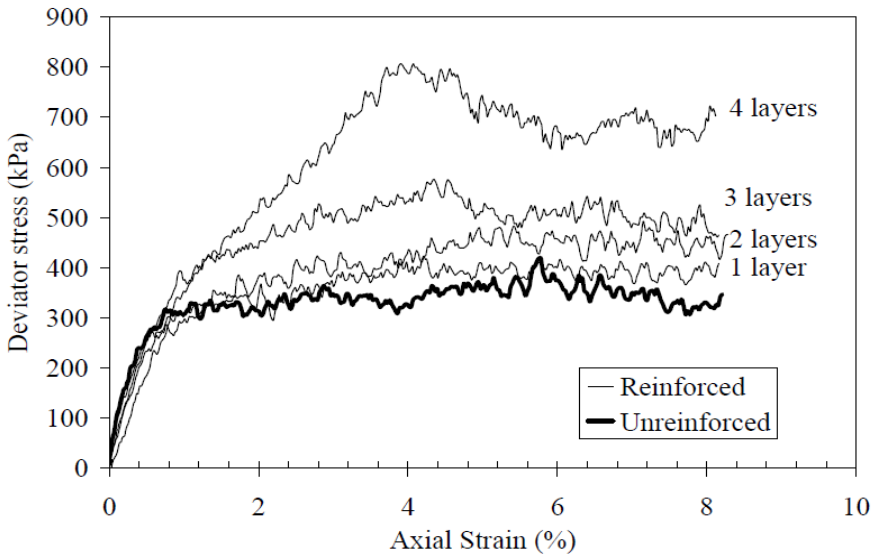

Figure 2-45 Stress – strain relationships of reinforced granular samples (Vinod et al. 2011)

authors studied the effect of thickness of geogrid material and multiple layers of geogrid reinforcement. The results showed insignificant improvement with single layer of reinforcement but significant improvement in strength in terms of peak deviatoric stress for multiple layers of geogrid reinforcement. Similar results were found by Yu and Pradhan (2014). The thickness and internal structural arrangement of geogrid particles

did not show any impact on strength of the samples. Pullout test simulation was performed by Zhang et al (2009) using DEM in two dimensions. The geogrid was modeled as a strand with junctions as shown in Figure 2-46.

Figure 2-46 2D DEM geogrid model (Zhang et al. 2009)

The numerical models discussed in previous section studied DEM modeling of geogrid reinforced aggregates by employing triaxial tests, biaxial tests, and pull out tests in 2D and 3D. The studies are spread over the effect of several external factors such as loading conditions and types and internal factors such as particle shapes and number of geogrid reinforcement layers. It has been shown in several studies that factors such as loading rates (Cheng et al. 2003; Lanier and Jean 2000; Liu and Zhang 2011; Markauskas and Kačianauskas 2006), boundary conditions (Cheung and O'Sullivan 2008; Tannant and Wang 2007), particle shapes (Rothenburg and Bathurst 1992; Thomas and Bray 1999), particle rotations (Ting et al. 1989) can have significant effect on behavior of DEM sample.

Lanier and Jean(2000) showed that by altering loading rate on a DEM rock sample can have significant effect on the stress vs. strain behavior as shown in Figure 2-47. Boundary conditions can be an important consideration in studying geogrid reinforcement in DEM. Flexible boundary conditions are relatively better representation of realistic compression tests (Tannant and Wang 2007) in terms of ability of the DEM sample in exhibiting bulging behavior. However Cheung et al(2008) in their studies have found slight deviation in the behavior of 2D DEM sample and even so less in a 3D DEM triaxial sample as can be seen in Figure 2-48 and Figure 2-49 respectively. Rothenburg

and Bathurst (1992) showed that increasing angularity in particles can alter the stress vs strain and volumetric strain behavior of a DEM sample as shown in Figure 2-50.

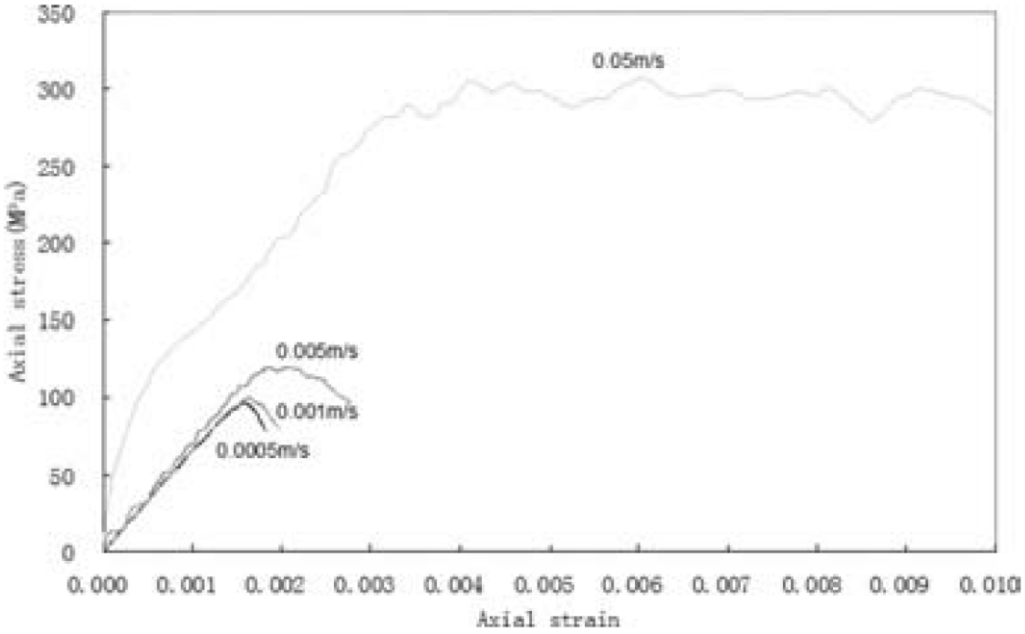

Figure 2-47 Stress vs strain behavior of DEM rock sample at varied loading rates (Lanier and Jean 2000)

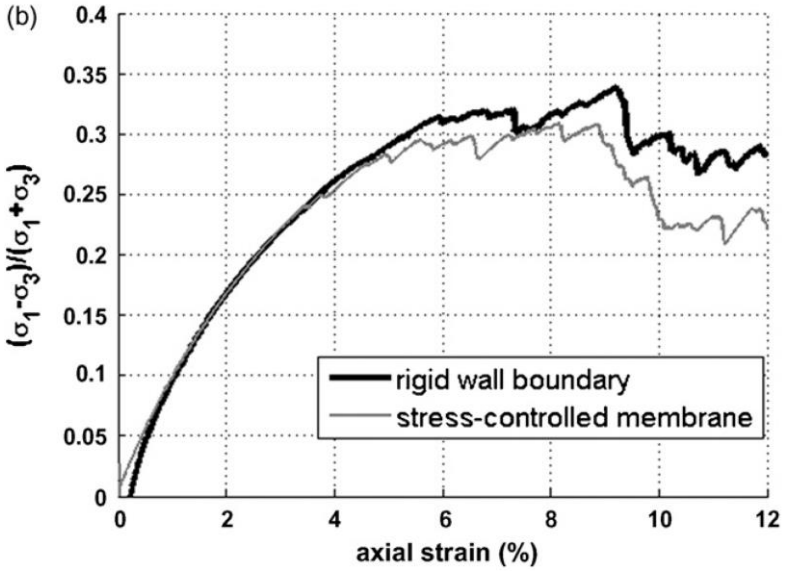

Figure 2-48 Bulk behavior of 2D DEM biaxial sample

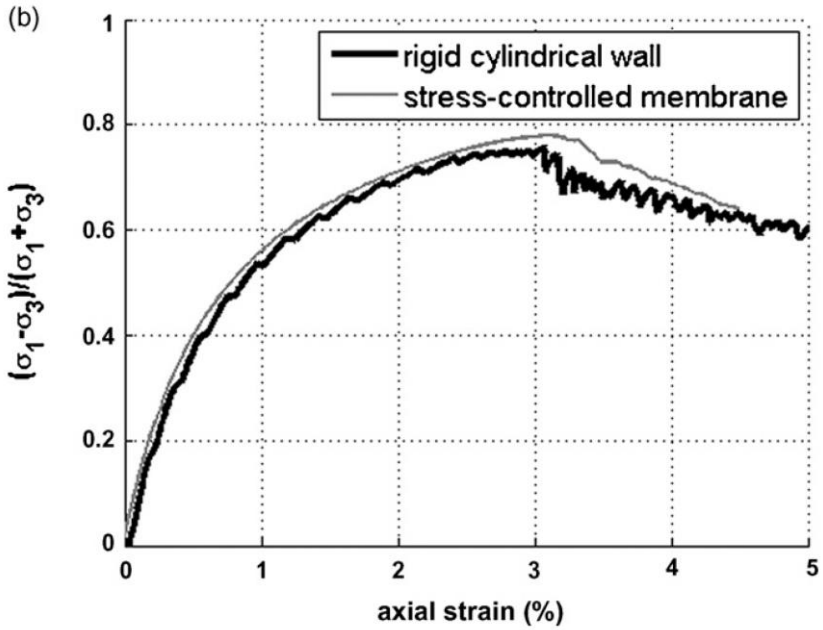

Figure 2-49 Bulk behavior of 3D DEM triaxial sample

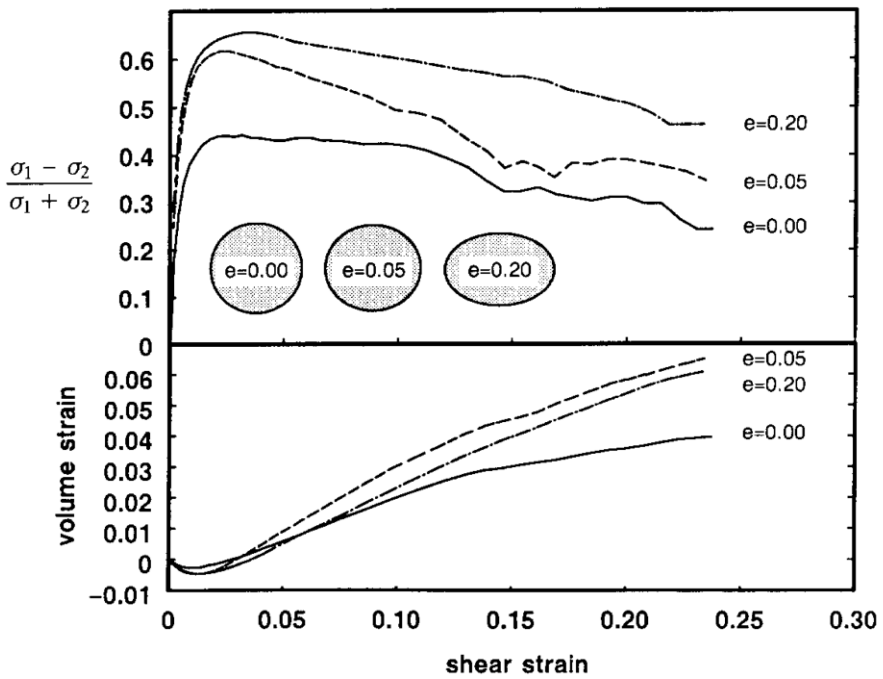

Figure 2-50 Effect of angularity on stress-strain and volumetric strain behavior (Rothenburg and Bathurst 1992)

2.5 Summary

Geogrid reinforcement was studied experimentally and numerically using DEM. However there is a lack of study of geogrid reinforcement that can comprehensively compare experimental and numerical results. The reinforcement mechanism in 2D and 3D have not been examined comparatively. Furthermore, the DEM study of geogrid reinforcement is spread over and lacks a unifying study on the important aspects such as effect of loading rates, boundary conditions, particle shapes, and particle rotations.

Chapter 3

Experimental Program

3.1 Introduction

Triaxial test was selected to study geogrid reinforcement behavior. The reasons for selecting triaxial test are as follows.

- It is a common method of testing soil,
- Previous experimental studies on geogrid reinforced have been performed using triaxial tests,
- And the equipment was available in the laboratory.

3.2 Materials

The materials for selected for testing were BX1100 geogrid from Tensar International Corporation, and glass beads shown in Figure 3-1 from Fox Industries produced as grinding media. BX1100 was used as it was readily available in the laboratory. The reasons for selecting grinding media of silicate and glass beads were as follows.

- The materials are hard and hence breakage can be avoided in testing
- It is not necessary to model breakage of soil in numerical model which also was not the scope. Inclusion of breakage in the simulation makes the numerical model more complex and requires a different set of study for calibration.
- The particles needed to have the possibility of being able to joined together to study effect of particle shape, the joining material also having the same property as the joined particles.

Clumped glass beads as shown in Figure 3-2 were produced by joining two similar sized glass beads together. The process involved placing two glass beads in an

arched holder shown in Figure 3-3 touching each other and heating them up to 2500 degrees Fahrenheit with a butane torch shown in Figure 3-4. Each clumped glass bead took approximately one minute for the fabrication process. Six thousands of the clumped glass beads were produced.

Figure 3-1 Glass beads

Figure 3-2 Clumped glass beads

Figure 3-3 Arched holder

Figure 3-4 Butane torch

The physical properties of the glass bead as provided by the manufacturer are presented in the following Table 3-1. However, basic tests were performed to verify the listed properties. The specification of BX1100 can be found on the manufacturer's website. In terms of tensile strength along the machine direction, the geogrid was rated at 8 kN/m at 5 % axial strain.

Table 3-1 Physical properties of the glass beads

Material	Properties	Value
Glass beads	Diameter	4.8 mm to 5 mm
	Specific density	2.5 g/cm^3
	Bulk density	1.5 g/cm^3
	Hardness	817 Hv

3.3 Test setup and sample preparation

Figure 3-5 shows the triaxial testing equipment FlowTrac II from GeoComp. The beads were poured into a split mold shown in Figure 3-6 lined with latex membrane layer by layer and compacted slightly by tamping with hand and without applying much effort. The samples were compacted in six layers. Figure 3-7 shows a completed sample in the split mold. Due to the cohesionless nature of the samples it was necessary to use a split mold. Also, even slight disturbance caused the samples to tilt and bulge rendering the samples useless and required several repetition for sample preparation. Additionally the split mold setup was modified to minimize disturbance to the samples when they were

being placed in the triaxial cell. The diameter of the mold was 71.12 mm. Sample heights varied between 153 mm to 162 mm.

For single layer of reinforcement, the geogrid was placed at the mid height of the sample, whereas for three layers of reinforcement, they were placed in such a way as to divide the sample into four equal parts as shown in Figure 3-8. Figure 3-9 shows a completed triaxial sample placed in a triaxial cell.

Figure 3-5 Triaxial testing equipment FlowTrac II from Geocomp

Figure 3-6 Position of geogrid in the sample

Figure 3-7 Split mold

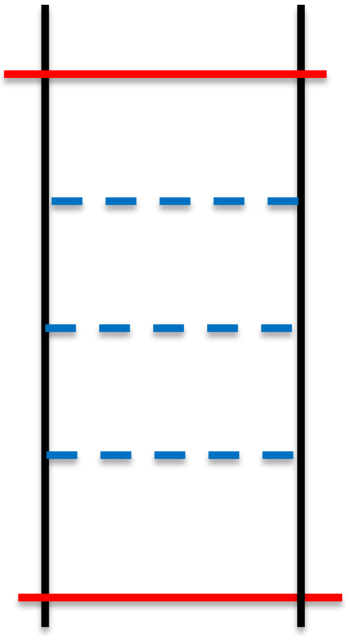

Figure 3-8 Three layers of geogrid reinforcement

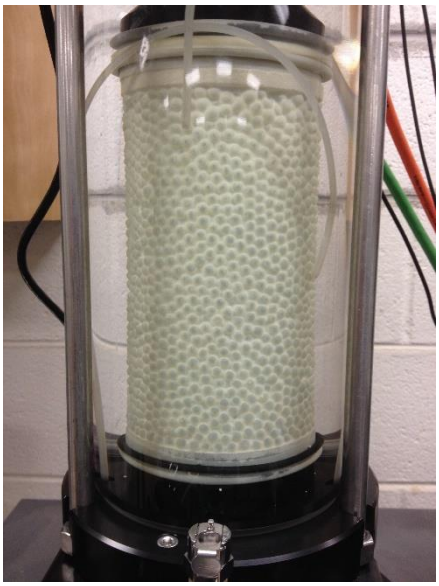

Figure 3-9 A triaxial sample of glass beads in a triaxial cell

3.4 Test program

The following Table 3-2 summarizes the number and type of triaxial tests performed. The unreinforced clumped glass bead assembly when tested at 100 kPa confinement produced large quantities of breakage. Each of the breakage was visually analyzed and the breakage took place at the joining section. Hence, the clumped glass beads were tested only at the confinement of 50 kPa. Each of the tests were run three times to check the repeatability of the test.

Table 3-2 Summary of experimental tests

Sample	Shape	Confinement (kPa)	Reinforcement
EC1	Circular	100	No
EC2	Circular	100	1 layer
EC3	Circular	100	3 layers
ECL4	Clump	100	No
ECL5	Clump	50	No
ECL6	Clump	50	1 layer
ECL7	Clump	50	3 layers

3.5 Results and discussions

The results of the experimental test program are summarized in the Table 3-3 below. The single glass bead assemblies had lower density than the clumped glass bead assemblies and was reflected in the porosity of the samples. The porosity in the clumped glass bead assemblies were lower than in the single glass beads assemblies.

Table 3-3 Summary of experimental results

Sample	Density (kg/m^3)	Confinement (kPa)	Porosity	Reinforcement	Mean peak deviatoric stress (kPa)	Reinforcement factor
EC1	1415.25	100	0.43	No	177.91	1.07
EC2	1410.41	100	0.44	1 layer	190.47	
EC1	1415.25	100	0.43	No	177.91	1.11
EC3	1403.39	100	0.44	3 layers	197.13	
ECL4	1548.34	100	0.38	No	478.12	
ECL5	1547.99	50	0.38	No	237.53	1.10
ECL6	1578.30	50	0.37	1 layer	258.42	
ECL5	1547.99	50	0.38	No	237.53	1.49
ECL7	1546.54	50	0.38	3 layers	354.24	

The deviatoric stresses in clumped glass bead assemblies were higher than in the single glass bead assemblies for both the cases of reinforced and unreinforced samples. The peak deviatoric stresses for both types of assemblies increased with geogrid reinforcement however the increase was more significant for the clumped glass bead assemblies. Reinforcement factor defined as the ratio of peak deviatoric stress of unreinforced assembly and reinforced assembly was calculated for the reinforced and

unreinforced pairs. The reinforcement factor for single layer of reinforcement in single glass beads assembly was merely 1.07 but increased to 1.1 with three layers of reinforcement. The reinforcement factor however was much greater for clumped glass bead assemblies.

Chapter 4

DEM Biaxial compression test

4.1 Introduction

Biaxial samples are simpler to study their behavior. The simplicity is due to the confinement of forces and displacements in only two dimension. It is always important to understand basic underlying phenomenon before undertaking complex models. This section explains the studies undertaken to understand necessary parameters of generation of a model and parametric analysis. The following table presents the summary of test runs performed for circular and clump biaxial samples. Several aspects of the models will be explained in detail in the coming sections.

Table 4-1 Summary of samples and test runs

Sample	Shape	Boundary	Confinement (kPa)	Reinforcement	Loading rate (m/s)
C1	Circular	Flexible	100	No	0.005
C2	Circular	Flexible	100	No	0.05
C3	Circular	Flexible	100	Yes	0.005
C4	Circular	Flexible	100	Yes	0.05
C5	Circular	Flexible	50	No	0.005
C6	Circular	Flexible	400	No	0.005
C7	Circular	Flexible	50	Yes	0.005
C8	Circular	Flexible	400	Yes	0.005
C9	Circular	Rigid	50	No	0.005

Table 4.1—*Continued*

C10	Circular	Rigid	100	No	0.005
C11	Circular	Rigid	400	No	0.005
C12	Circular	Rigid	50	Yes	0.005
C13	Circular	Rigid	100	Yes	0.005
C14	Circular	Rigid	400	Yes	0.005
C15	Circular	Flexible	100	Yes, 3 layers	0.005
C16	Circular	Flexible	100	No	0.001
C17	Circular	Flexible	100	No	0.0005
C18	Circular	Rigid	1000	No	0.005
C19	Circular	Flexible	1000	No	0.005
CL1	Clump	Flexible	100	No	0.005
CL2	Clump	Flexible	100	No	0.05
CL3	Clump	Flexible	100	Yes	0.005
CL4	Clump	Flexible	100	Yes	0.05
CL5	Clump	Flexible	100	Yes, 3 layers	0.005

4.2 Model validation

Results from numerical model were compared with the results from the experimental work of Abu-Farsakh et al (2009) as shown in Figure 4-1. The aspects of the numerical model will be explained in detail in the coming sections. The dashed lines represent the experimental triaxial test on granular soil named as Limestone I which was crushed limestone. ‘LTRC – limestone I’ had one layer, ‘LTRC – limestone I reinforced’ had two layers and ‘LTRC – limestone I reinforced 2 layers’ had two layers of geogrid reinforcement. Triaxial tests were performed on the limestone sample with one and two

layers of geogrid reinforcement. Unreinforced biaxial sample C1, reinforced biaxial sample C3, and derivative of C1 with two layers or reinforcements were modeled to match the experimental stress – strain curves. The results show that a good match was achieved between the numerical models and experimental results showing the capability of the numerical models. However, the loading rates used in the numerical model were not optimized. Also, back calculation showed that approximately 937,063 particles were required to approximately resemble the gradation curve for the limestone sample in 2D model. Even though such number of particles in a model is possible the computational time however can increase significantly.

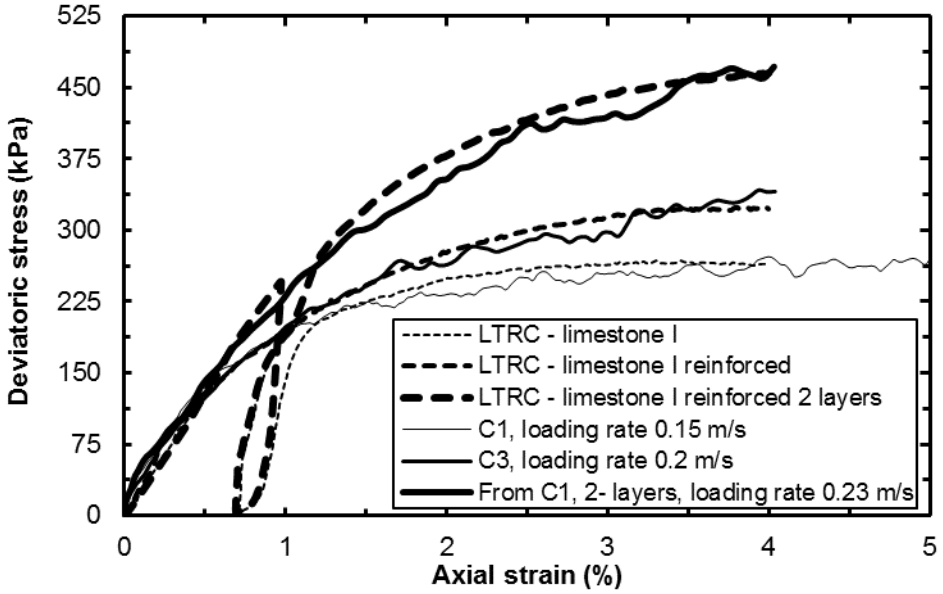

Figure 4-1 Comparison of PFC2D model and Limestone I from the works of Abu-Farsakh et. Al. (2009)

4.3 Sample generation

4.3.1 Circular particles

A biaxial sample of spherical particles was created by the method of random generation with a target initial porosity of 0.185 and reference boundary stress of 10 kPa. The target porosity and the reference boundary stress state act as a benchmark for creating future samples that can be thought of identical samples and be used in parametric analysis in such a way that the results are comparable between the samples. A boundary of four rigid walls was created, two vertical and two horizontal with height of 30 cm and width of 15 cm. Several particles of certain radius were created inside the boundary. The particle radius was then expanded to achieve desired porosity and boundary stress using the generalized particle generation algorithm provided in the software. The following Table 4-2 presents the micro properties and Figure 4-2presents the particle size distribution of the biaxial sample of circular particles. It is important to understand that the sample can be in fact achieved in lower porosity with the same particle number and gradation by first compacting them with much lower particle surface friction and shear stiffness. This is also possible by increasing the initial boundary stress higher than the reference stress state of 10 kPa.

Table 4-2 Properties of DEM Particles and Boundary Walls

Property	Value
Normal stiffness, Kn	1e8 N/m
Shear stiffness, Ks	8.5e7 N/m
Density of a particle	2600 kg/m^3
Friction coefficient of particle surface	0.55
Initial target porosity	0.185
Wall normal stiffness (vertical)	1e7N/m
Wall normal stiffness (platens)	1e8 N/m
Wall shear stiffness (vertical)	0
Wall shear stiffness (platens)	0
Loading platen surface friction	1
Vertical wall surface friction	0

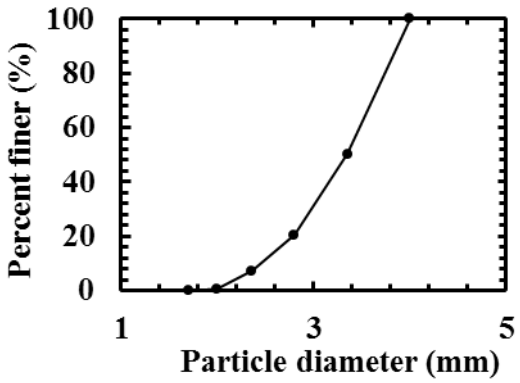

Figure 4-2 Particle size distribution of the biaxial sample

Figure 4-3 shows the 2D DEM biaxial sample used in the simulations. The sample was cycled to equilibrium to ensure that there was no unbalanced force in the sample. At equilibrium the ratio of unbalanced forces to maximum contact force in the

sample is in the order of 1^{-3}. However, the adequacy of this ratio is to be judged by the user. In order to achieve efficient equilibrium all the forces in the samples were reduced by a factor of 0.7. Such a method of achieving quick equilibrium is only valid for quasi static modeling where dynamic effects are not modeled.

Equation 1 relates force, mass, and acceleration of a particle. When quasi static simulation is required the F_i component is reduced by a quantity of F_i^d as shown in Equation 2. F_i^d is related to F_i as shown in Equation 3. The value of α is preset at 0.7 by default in PFC however, it can be change by the user.

$$F_i = M_i a_i \qquad \text{Eq 1}$$

$$F_i + F_i^d = M_i a_i \qquad \text{Eq 2}$$

$$F_i^d = \alpha F_i \qquad \text{Eq 3}$$

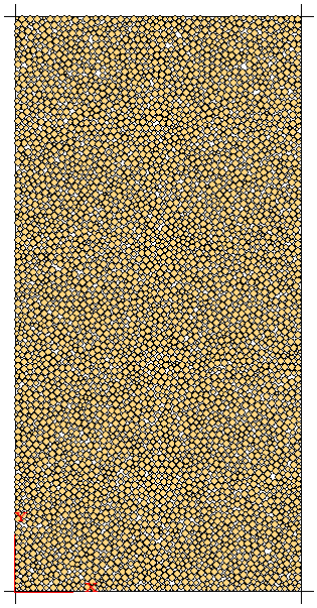

Figure 4-3 2D DEM biaxial sample

4.3.2 Clump particles

Clump particles were generated by replacing circular particles with two particle clump template as shown in Figure 4-4. The circular particles were replaced in the biaxial sample that was already in equilibrium before application of servo control. The particles were replaced in such a way that each clump particle had the same mass as the original particle that was replaced. As described in section 2.2.8 the constituent particles act as rigid bodies and do not break away from each other no matter the forces acting on them.

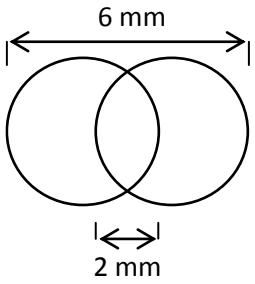

Figure 4-4 Two particles clump template

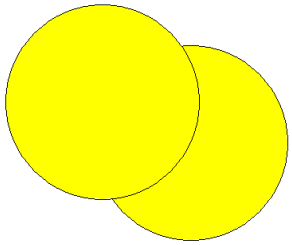

Figure 4-5 Clump particle from 2D DEM clump sample

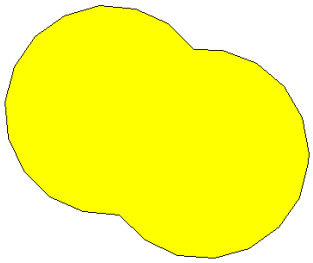

Figure 4-6 Clump particle from 2D DEM clump sample with outline boundary

After generation of clump particles, the sample was then cycled to equilibrium to reduce unbalanced forces.

4.3.3 Geogrid

Geogrid model was developed by joining circular particles together with contact bond and parallel bond. Contact bonds as described in section 2.2.10 are imagined as a piece of rubber band holding particles together. However the particles connected in such way can roll against each other as shown in Figure 4-7 and Figure 4-8. Initially particle ‘A’ and Particle ‘B’ are at the same level. When particle ‘A’s’ position is fixed but particle ‘B’ is allowed to move under gravity, it rotates around ‘A’ dropping down from the initial level.

Figure 4-7 Particles bonded with contact bond in initial position

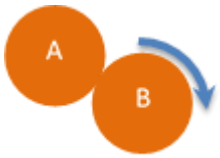

Figure 4-8 Particle bonded with contact bond after certain time

However, parallel bond can counter such effect by introducing an element with certain cross section between the two particles as shown in Figure 4-9. The element labeled as ‘C’ acts as a piece of cementation between the particles ‘A’ and ‘B’ and is able to generate moment, tensile, and shear forces.

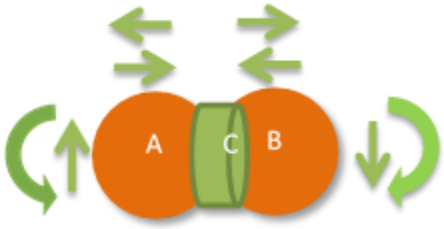

Figure 4-9 Parallel bond connecting two particles

Figure 4-10 shows the DEM geogrid model developed in two dimensions created by bonding circular particles together using contact bonds and parallel bonds. Due to the introduction of contact and parallel bonds the behavior of such particles become complex. Such interaction is explained in much detail in section 4.4. The presence of parallel bond was necessary in modeling the geogrid due to the fact that geogrids have flexural rigidity. In absence of parallel bond the geogrid would merely act as an elastic string.

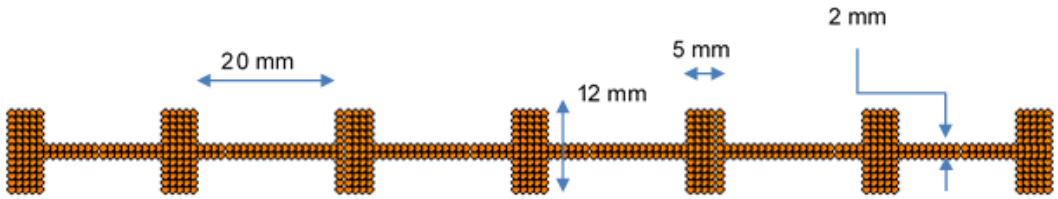

Figure 4-10 2D DEM geogrid model

4.3.4 Reinforced samples

Reinforced samples were created from samples at equilibrium shown in Figure 4-11. Reinforced sample were created by inserting geogrid in the sample for both circular and clump particles. For the insertion a gap was generated at the mid height of the sample as in Figure 4-12, geogrid was generated as in Figure 4-13, and the sample was then compacted back again as shown in Figure 4-14. For three layers of geogrid reinforcement the sample was divided into four equal parts by generating gap between them where the geogrid layers were generated. The sample was then compacted back again. Finally the samples were then cycle to equilibrium.

Figure 4-11 Sample at equilibrium after generation

Figure 4-12 Divided sample with gap

Figure 4-13 Geogrid in the gap

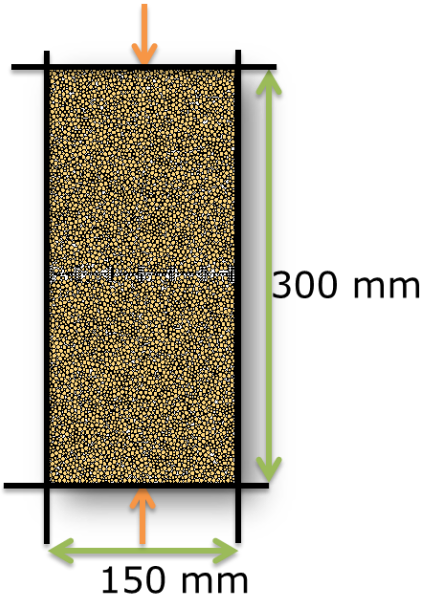

Figure 4-14 Recompacted sample with geogrid

4.3.5 Flexible and rigid boundary

Flexible and rigid boundary refer to the type of boundary confinement of the biaxial samples. Rigid boundary consisted of only one vertical wall on each left and right sides. The stresses are then averaged over the entire height of the wall lying between the position of top and bottom horizontal walls. Top and bottom walls are however always rigid as they are used for applying load in terms of constant displacement. For simulating flexible boundary each vertical walls were replaced with 50 segments of vertical walls. Each pair of vertical walls (a pair consisting of two walls, one on left and one on right at the same height) were independent of other pairs in terms of calculating stresses and strains thus performing as a flexible boundary. Such was the case for reinforced samples too for circular and clump particles.

4.4 Particle interaction

Circular particles, when there are no contacts bonds and parallel bonds between them, using linear contact model, interact according to the following Eq. 4 and Eq. 5 where F_i^n is the normal force between contacting particles, K^n is the normal contact stiffness, and U^n is the overlap between the contacting particles. In the shear direction, ΔF_i^s is the incremental shear force for the incremental shear displacement of ΔU_i^s related by the shear stiffness of K^s.

$$F_i^n = K^n U^n \quad \text{Eq. 4}$$

$$\Delta F_i^s = K^s \Delta U_i^s \quad \text{Eq. 5}$$

The shear force is accumulated for each incremental shear displacement, initially zero at the formation of contact, and is controlled by $F_{\max}^s$. When the accumulated shear

force exceeds this value, the contacting surfaces slide against each other setting the maximum shear force to $F_{\max}^{s}$. This is called ‘slip’ in PFC and is basically the failure mechanism between particles in the absence of contact bonds and parallel bonds.

When contact bond is present it supersedes the so defined slip behavior. Contact bond absolutely defines the contact normal strength in tension and contact shear strength in shear. Figure 4-15 and Figure 4-16 describes the contact and slip model in PFC. In tension, the slip behavior is always inactive and the contact bond breaks when it reaches the defined maximum value of F_n^c as in Figure 4-15. However, in shear the slip behavior is superseded by contact bond. The contact bond breaks in shear when the accumulated shear force exceeds defined maximum value of F_s^c as in Figure 4-16. Parallel bond if present acts in conjunction with the slip behavior and contact bond if present. It has no effect on the slip model and slip model is active even when parallel bond is present without contact bond. Parallel bond only provides the displacement and force behavior of the fictitious cementation material between the particles.

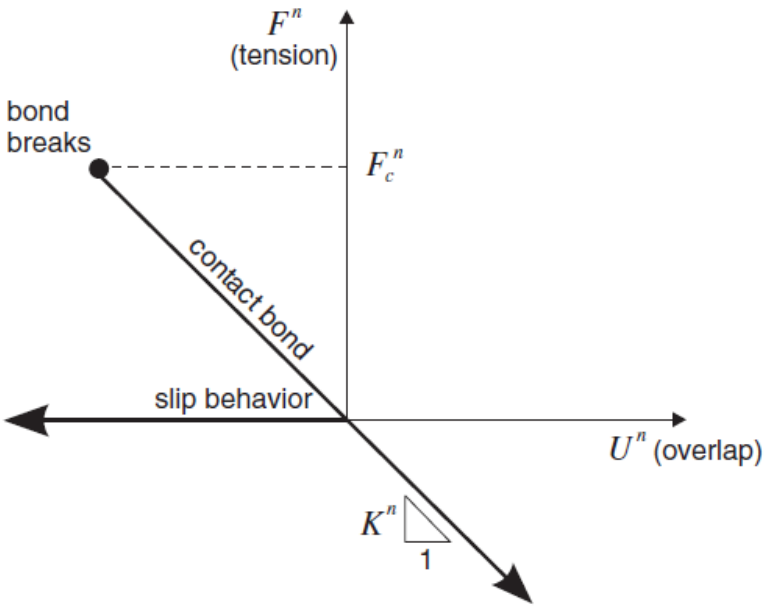

Figure 4-15 Contact bond behavior in normal direction(Itasca Consulting Group 2008)

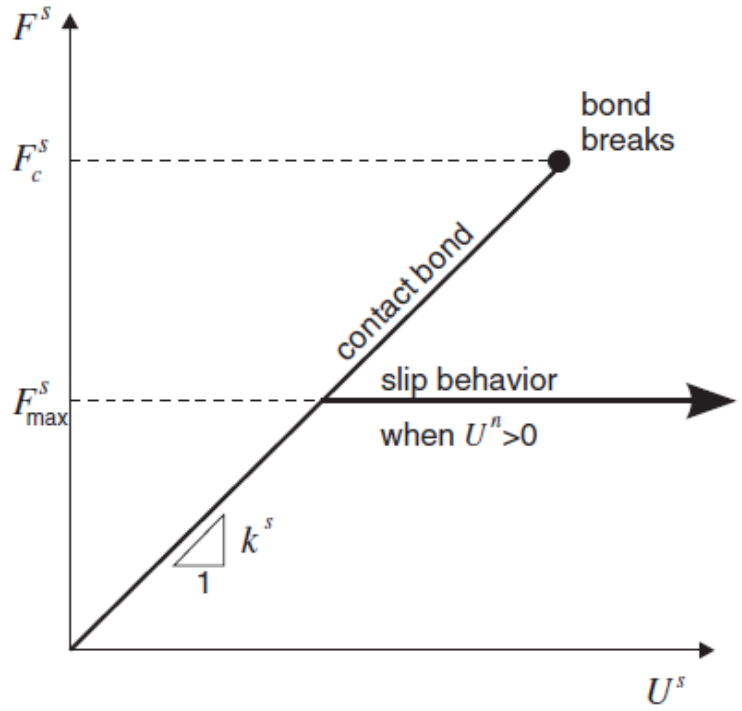

Figure 4-16 Contact bond behavior in shear direction(Itasca Consulting Group 2008)

4.5 Loading

The loading stage consisted two sub stages – application of servo control and application of load by applying constant displacement to the top and bottom walls. The procedure is explained in much detail in the following sections. All biaxial samples were loaded to axial strain of 5 %.

4.5.1 Calibration of geogrid

The geogrid was calibrated as BX1100 from Tensar Corporation to the tensile strength of 8 kN/m at 5% strain. The geogrid was extended at very slow rate by pulling at its either end as shown in Figure 4-17 to avoid any dynamic effect. The dynamic effects can cause non-linear behavior and higher tensile strength rating. The force required to pull the geogrid to 5 % of axial strain was recorded and when it was 8 kN the geogrid was considered calibrated with the BX1100. Figure 4-18 shows the calibration curve for the geogrid for tensile strength.

Figure 4-17 Set up for tensile test of geogrid

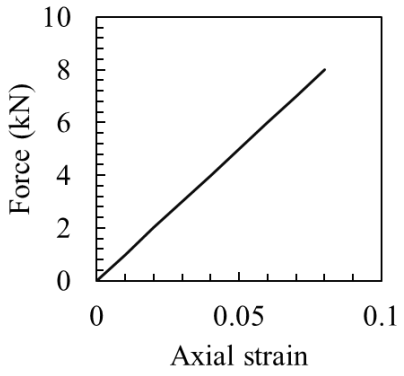

Figure 4-18 Calibration of geogrid

4.5.2 Loading of biaxial samples

After equilibrium was achieved following sample generation, uniform confining pressure was applied to the sample at equilibrium. The confining pressure was applied by numerical servo control that moves the four walls away from each other expanding the sample or towards each other compressing the sample at certain rate whichever was necessary to achieve isotropic confinement. When the prescribed confining pressure was achieved the sample was ready for loading.

The sample was loaded by applying constant rate of displacement to the top and vertical walls acting as loading platens meanwhile the numerical servo control kept the confining pressure at the prescribed level on the vertical boundary as shown in Figure 4-19. The sample was loaded until a pre-determined level of axial strain wash achieved. The entire process of sample generation and loading has been summarized in a flow chart in Figure 4-20 used in this study. Table 4-1 presents the summary of number and types of tests that were performed in the study of behavior of biaxial samples.

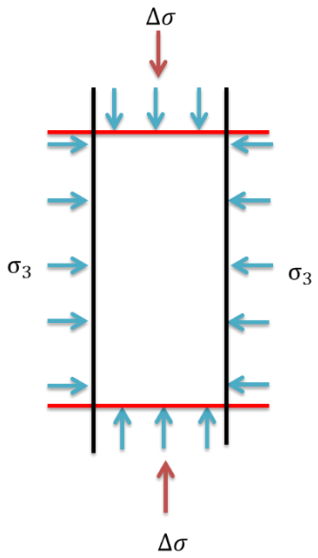

Figure 4-19 Loading of DEM biaxial sample

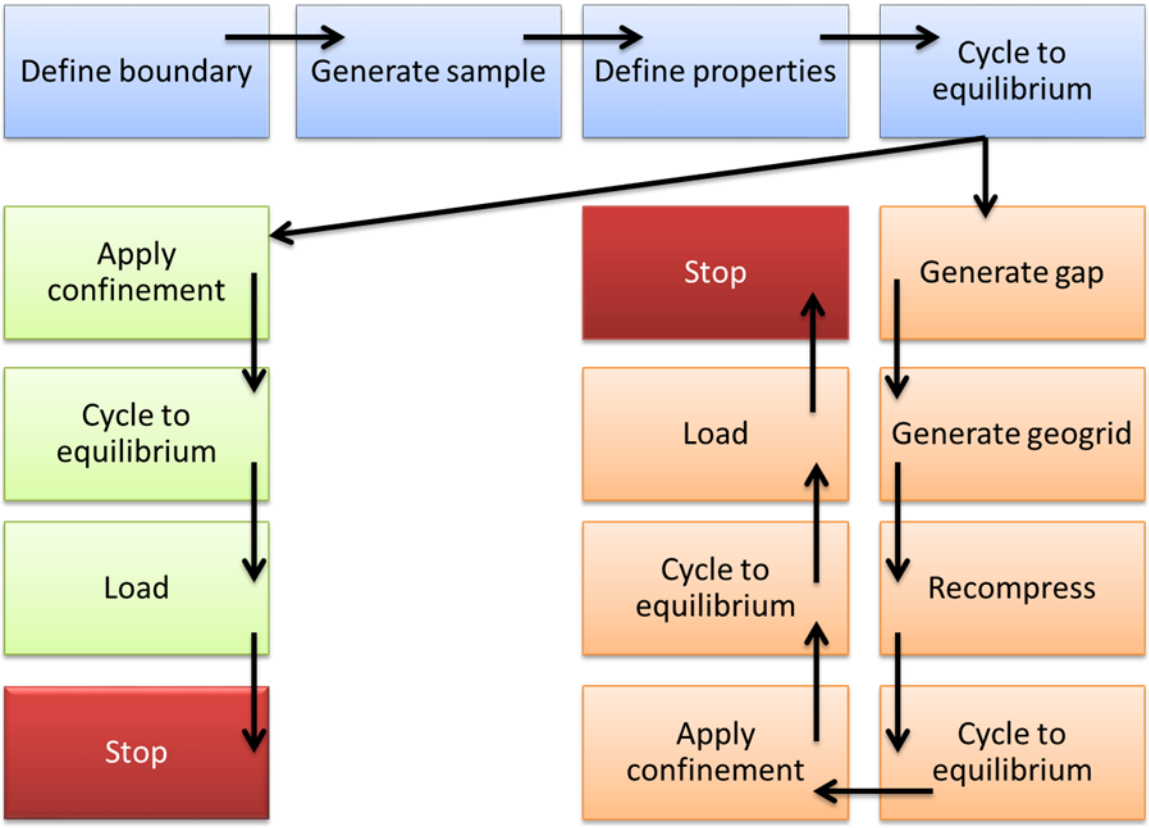

Figure 4-20 Flow chart for stages in 2D sample generation and testing

4.6 Results and discussions

4.6.1 Effect of loading rate

Loading rate is an important factor in assessing behavior of DEM samples and samples should always be loaded at their optimum loading to find their true behavior. Loading rate here means the velocity of loading platens. A safe way to ascertain correct loading rate is to load a sample at extremely slow speed however, this approach is time consuming when several tests are to be performed. Optimum loading rate is also necessary to ensure quasi static compression.

An efficient way of ascertaining optimum loading rate is to load a sample at several loading rates and select the fastest loading rate at which the behavior of the sample is similar to the slowest loading rate used. In this study four loading rates were used– 0.0005 m/s, 0.005 m/s, 0.001 m/s, and 0.05 m/s to determine the optimum loading rate. The samples were loaded to 5 % axial strain.

4.6.1.1 Unreinforced circular sample

Unreinforced biaxial samples of circular particles with flexible boundary were loaded at loading rates of 0.0005 m/s, 0.005 m/s, 0.001 m/s, and 0.05 m/s. The stress vs strain relationships for such a samples is shown in Figure 4-21. The fastest loading rate of 0.05 m/s produced significantly different stress-strain relationship than other slower loading rates. However, the relatively slower loading rates of 0.005 m/s, 0.001 m/s, and 0.0005 m/s produced similar results in terms of stress-strain relationship. It can be inferred from the results that 0.005 m/s is the optimum loading rate in terms of the loading rate beings fastest loading rate producing similar results as the slowest loading rate of 0.0005 m/s. It is important to note that the time-step in the mentioned simulations did not change.

Figure 4-22 shows the volumetric strain behavior of the samples for various loading rates. It is evident from the figure that fastest loading rate of 0.05 m/s produced highest compression of volume and slower volumetric dilations. All of the other slower rates of 0.005 m/s, 0.001 m/s, and 0.0005 m/s produced smaller volumetric compression and faster dilation with similar behavior.

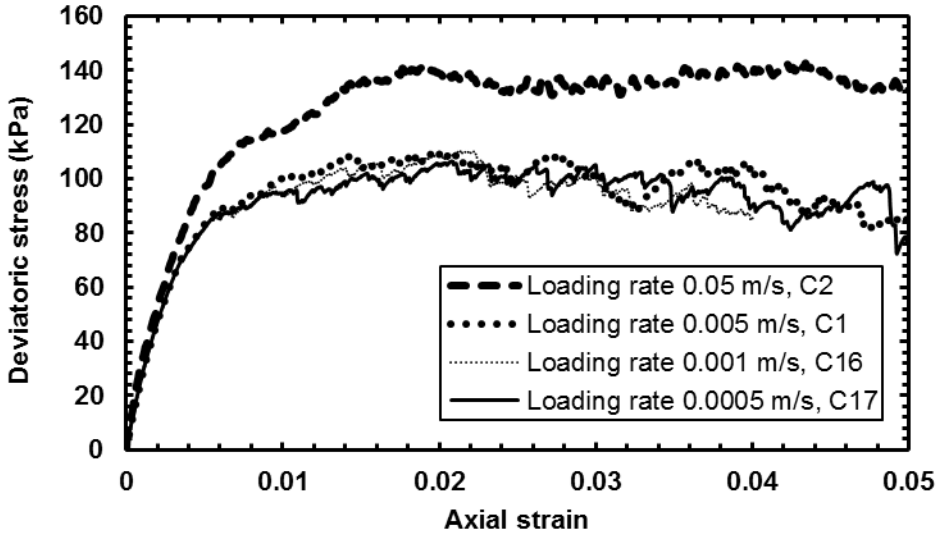

Figure 4-21 Deviatoric stress vs axial strain for various loading rates for unreinforced circular samples with flexible boundary

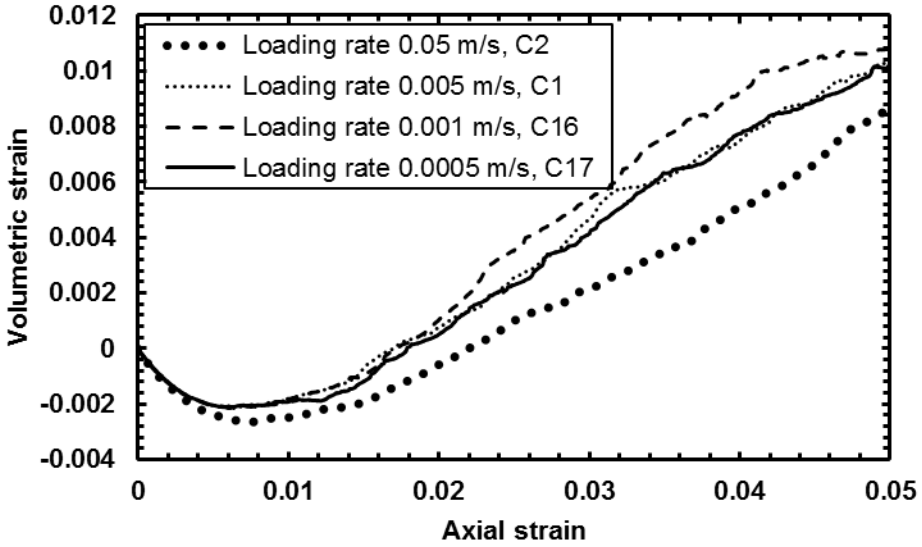

Figure 4-22 Volumetric strain vs axial strain for various loading rates for unreinforced circular samples with flexible boundary

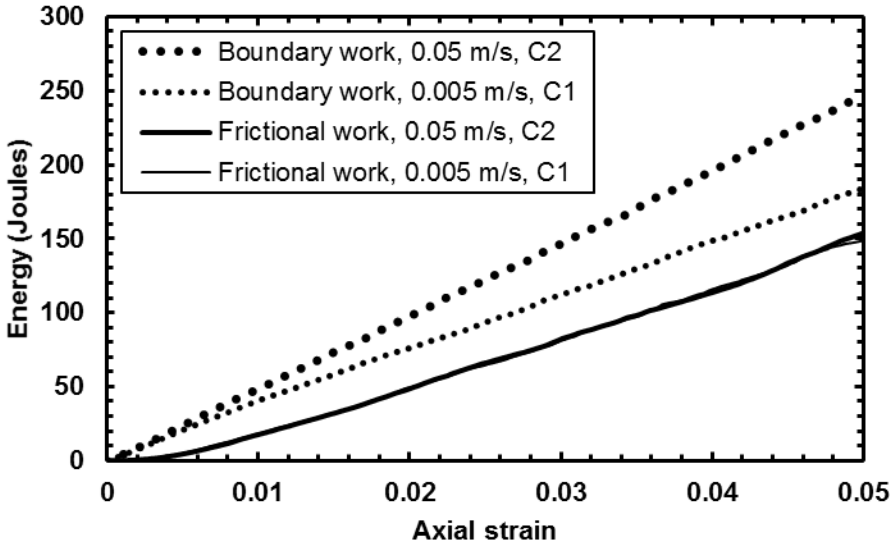

Figure 4-23 Boundary and frictional work for different loading rates

From energy considerations also, Figure 4-23 shows that frictional work done is almost identical for both the loading rates of 0.05 m/s and 0.005 m/s whereas the work done by boundary walls on the particles are significantly different. The boundary and frictional work on certain samples have been summarized in Table 4-4. The work done by boundary is the total accumulated work expressed in Eq. 6. E_W is accumulated work done by walls on the particles, N_w is the number of walls, F_i and M_i are the forces and moments acting on the wall, and ΔU_i and $\Delta\theta_i$ are applied displacement and rotations in every timestep. Similarly E_f in Eq. 7 is the energy dissipated due to slip at contacts with average shear force of F_i^s for average slip displacement of ΔU_i^s. The observation reveals that the walls experience higher forces and moments when loading rates higher than the optimum loading rates were applied, however, the energy dissipation by frictional slipping which is the only way of energy dissipation in such model stayed identical.

$$E_W \leftarrow E_W - \sum_{N_w} (F_{i\Delta U_i} + M_i \Delta\theta_i) \quad \text{Eq. 6}$$

$$E_f \leftarrow E_f - \sum_{N_w} (F_i^S \Delta U_i^S) \quad \text{Eq. 7}$$

The porosity of the samples at different locations within the samples were measured at different axial strains during the loading stage by setting up 144 measurement circles as shown in Figure 4-24. The circles were arrange in overlapping manner to average the porosity measurements throughout the sample without excluding contribution of particle inside the boundary of measurement circle arrangements.

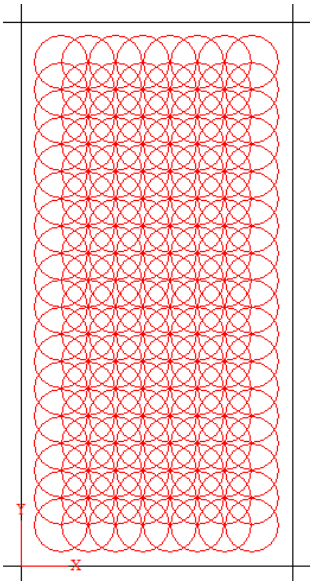

Figure 4-24 Measurement circles

The porosity measurements on the samples at different loading rates yielded similar results as shown in Figure 4-26 to Figure 4-31. The porosity was seen to be distributed in between 0.15 to 0.19 in the initial state just before loading the sample

although the target porosity was 0.18. As the loading progressed the areas of lower porosity can be seen progressing and coalescing, eventually forming shear bands in diagonal direction for both loading rates as shown inFigure 4-30 and Figure 4-31. However, in the slower loading rate a much better defined shear band spanning diagonally across the sample was seen for the optimum loading rate in Figure 4-31. The development of extended regions of lower porosity in the mid height of the sample seen in Figure 4-31 is in agreement with the bulging of the sample around its mid height as in Figure 4-25 which shows the failed sample at 5 % axial strain.

Figure 4-25 Unreinforced circular biaxial sample at 5 % axial strain with flexible boundary loaded at 0.005 m/s

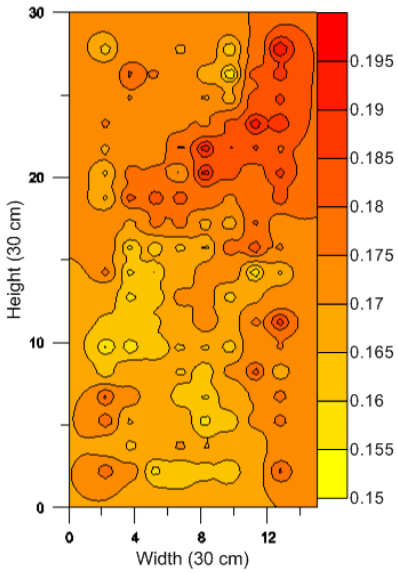

Figure 4-26 Porosity at 0.5 % axial strain (0.05 m/s)

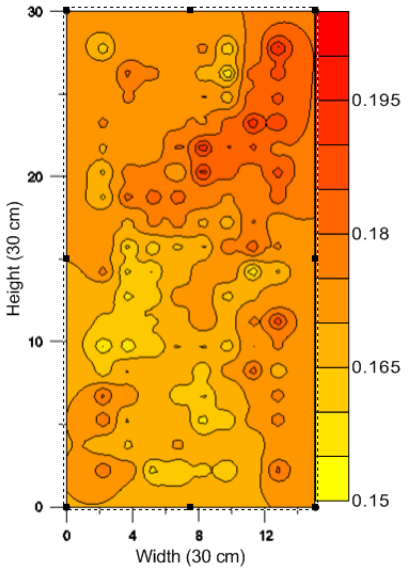

Figure 4-27 Porosity at 0.5 % axial strain (0.005 m/s)

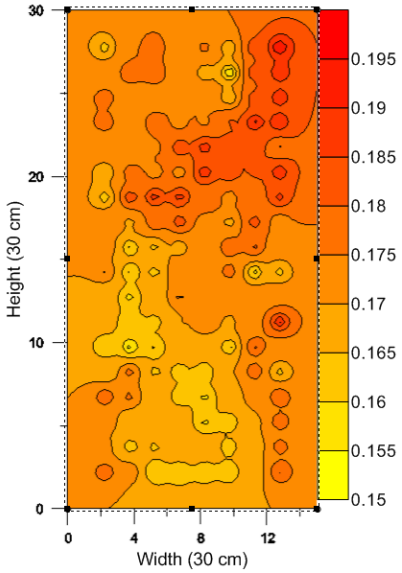

Figure 4-28 Porosity at 1.5 % axial strain (0.05 m/s)

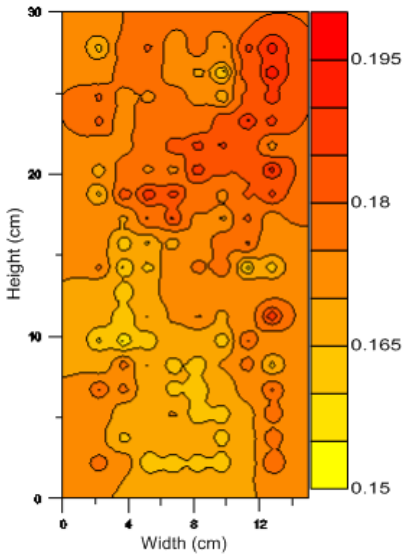

Figure 4-29 Porosity at 1.5 % axial strain (0.005 m/s)

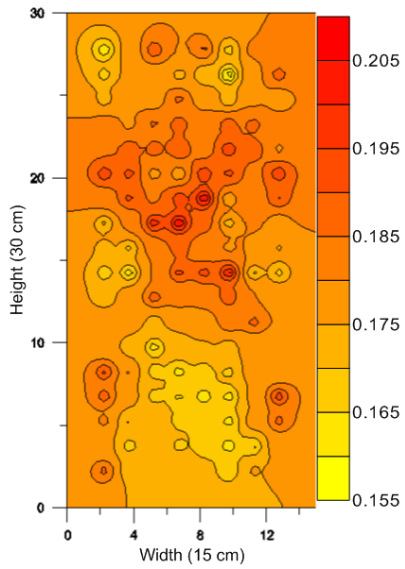

Figure 4-30 Porosity at 4.5 % axial strain (0.05 m/s)

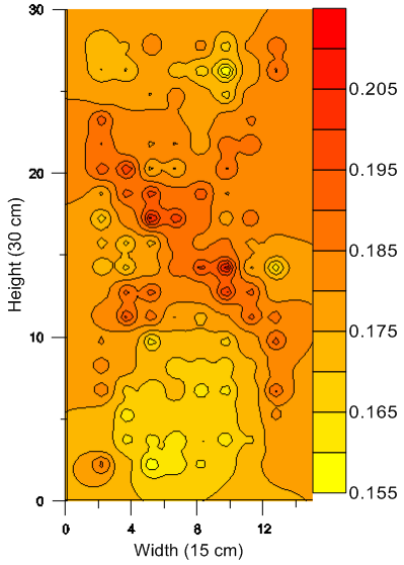

Figure 4-31 Porosity at 4.5 % axial strain (0.005 m/s)

Typical behavior was seen for both loading rates in terms of contact orientations, and normal and shear force orientations as seen in Figure 4-32 to Figure 4-36. The figures are polar plots of polar frequency distribution diagram with bin sizes of 10 degrees. In the contact orientation diagram in Figure 4-32 all other diagrams for contact orientation, the length of each bin size represents the frequency or the number of contacts oriented in the bin's direction. In Figure 4-33 to Figure 4-36 for normal force and shear force diagram and in all other such diagrams the length of each bin represents normal or shear force magnitudes at contacts and the orientation of the bin represents the orientation of their contacts. The normal forces are mostly aligned in vertical direction which is at it should be for the case of a vertically loaded sample. However the normal forces in the case of faster loaded sample of 0.05 m/s are higher than in the slower loaded sample of 0.005 m/s. However, the shear forces did not vary with loading rates as can be seen fromFigure 4-35 and Figure 4-36. Hence, the increased deviatoric stress in

the case for faster loading rate is due to the higher normal forces acting on the walls and particles rather than increased shear strength of assembly.

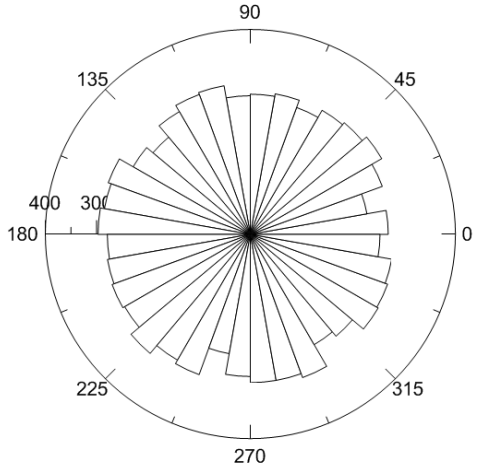

Figure 4-32 Contact orientation before loading

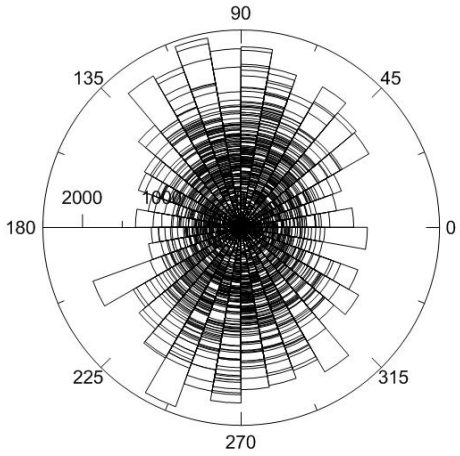

Figure 4-33 Normal forces at 1.5 % axial strain (0.05 m/s)

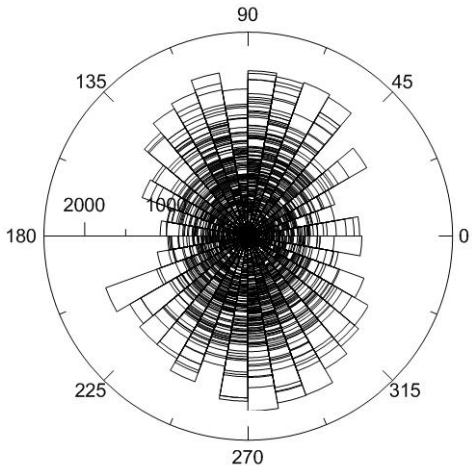

Figure 4-34 Normal forces at 1.5 % axial strain (0.005 m/s)

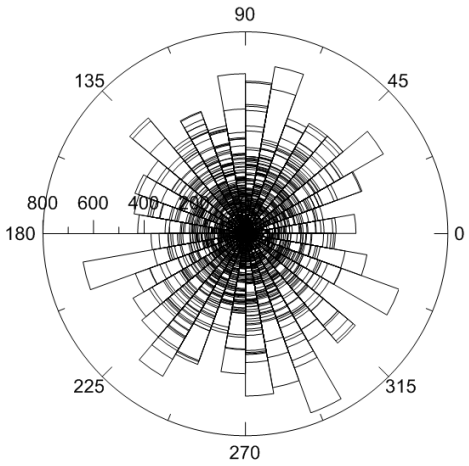

Figure 4-35 Shear force at 1.5 % axial strain (0.05 m/s)

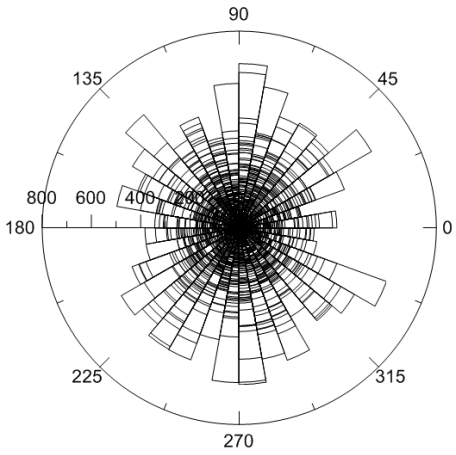

Figure 4-36 Shear force at 1.5 % axial strain (0.005 m/s)

4.6.1.2 Geogrid reinforced circular sample

The effect of loading rate was more significant on geogrid reinforced circular sample as shown in Figure 4-37 as compared to unreinforced sample amplifying the increase in deviatoric stress due to the presence of geogrid. The ‘UR’ and ‘RE’ represents unreinforced and reinforced sample respectively. The volumetric dilation was much different for reinforced samples from unreinforced samples as shown in Figure 4-38. The reinforced samples experienced significantly less volumetric dilation than the reinforced sample. But, the dilation behavior did not change with the loading rate. In terms of boundary work and frictional work as shown in Figure 4-39 , the observations were similar with the case of unreinforced samples. The frictional work was almost identical in both loading rates but the boundary work was higher in faster loading rate than in slower loading rate. Also, the maximum boundary work performed when compared to unreinforced case was higher in the reinforced sample for all loading rates including the frictional energy.

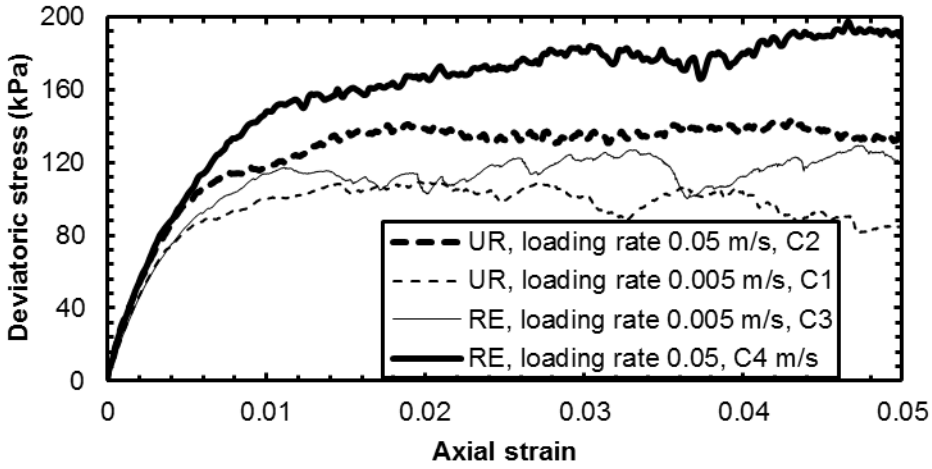

Figure 4-37 Deviatoric stress vs axial strain for various loading rates for reinforced circular samples with flexible boundary

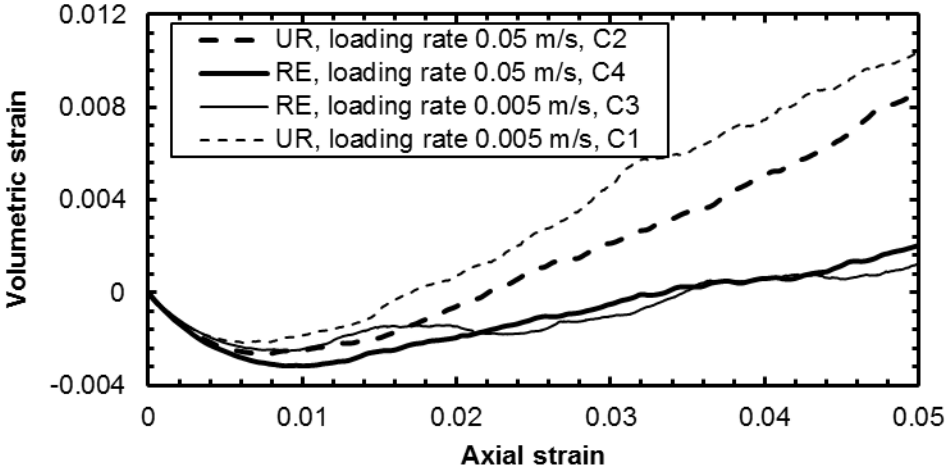

Figure 4-38 Volumetric strain vs axial strain for various loading rates for reinforced circular samples with flexible boundary

Figure 4-40 shows the failed reinforced circular sample at 5 % of axial strain with flexible boundary. Figure 4-41 to Figure 4-47 shows the evolution of porosity in the reinforced samples for the loading rates of 0.05 m/s on the left and 0.005 m/s on the right. The patterns of lower porosity in the middle height of the sample are due to geogrid

since the geogrid were modeled with a structured arrangement with fewer contacts compared to soil particles. In terms of loading rate no significant difference in porosity evolution was observed but extended areas of lower porosity were observed in the upper portion of the sample as seen in Figure 4-46 and Figure 4-47 which can be explained by the dilation of the sample observed in upper portion as shown in Figure 4-40.

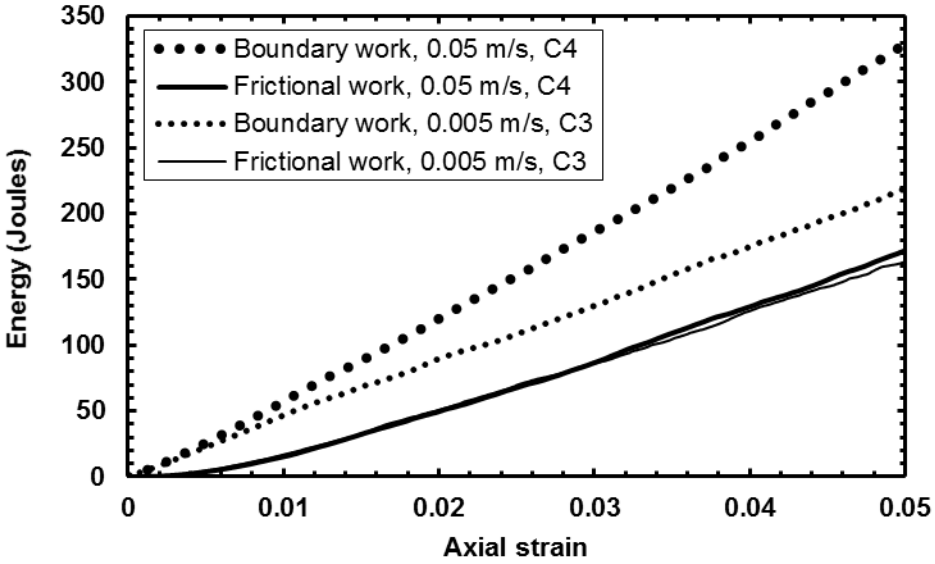

Figure 4-39 Boundary and frictional work for different loading rates for reinforced sample

The magnitude and orientation of contact forces in the slower and faster loaded samples at different stages have been presented in Figure 4-48 to Figure 4-57. The polar distribution of normal forces show that the faster loading rate produced higher normal contact forces oriented in vertical direction when compared to slower loading rate. The shear forces on the other hand showed specific diagonal orientation during loading phase for the sample loaded at optimum loading rate of 0.005 m/s as seen in Figure 4-55 and Figure 4-57.

Figure 4-40 Reinforced sample at 5 % axial strain loaded at 0.005 m/s

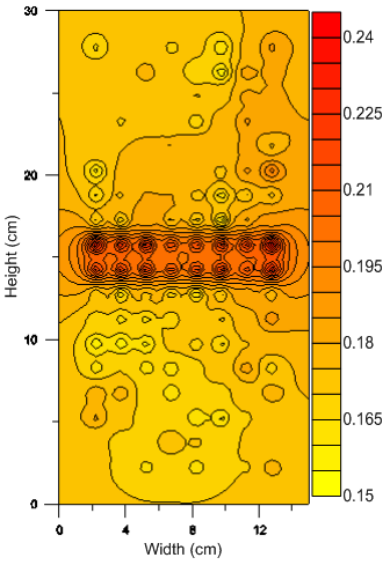

Figure 4-41 Porosity before loading

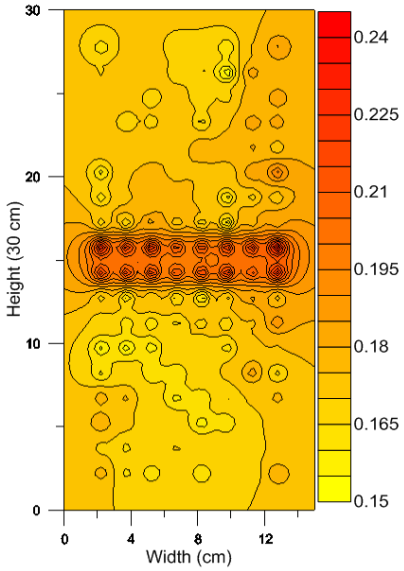

Figure 4-42 Porosity at 0.5 % axial strain (0.05 m/s)

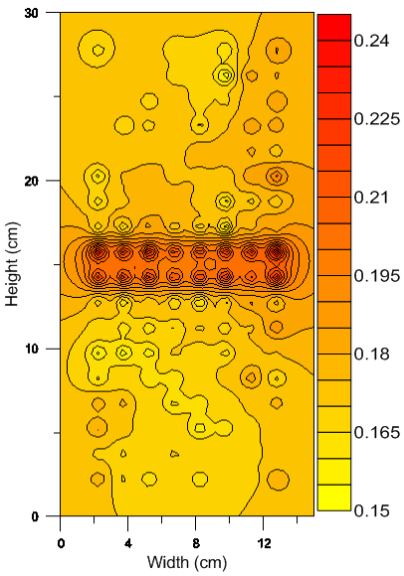

Figure 4-43 Porosity at 0.5 % axial strain (0.005 m/s)

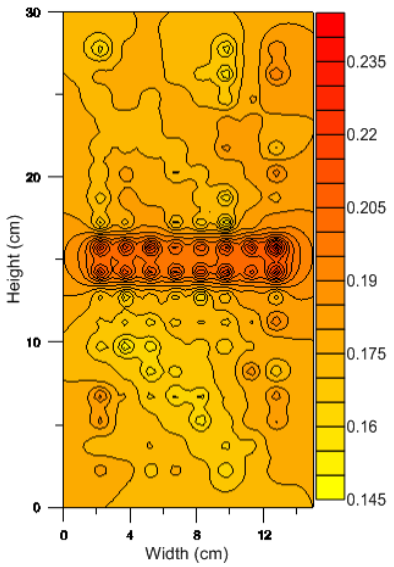

Figure 4-44 Porosity at 2.5 % axial strain (0.05 m/s)

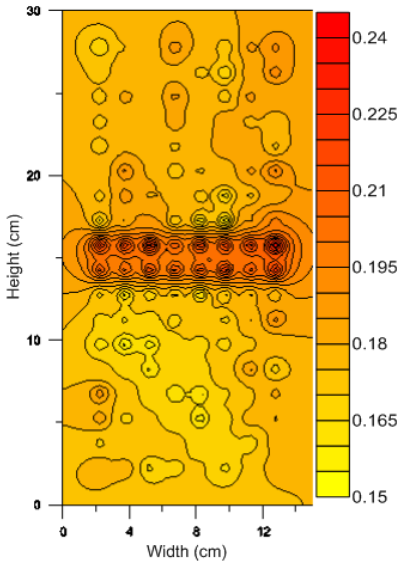

Figure 4-45 Porosity at 2.5 % axial strain (0.005 m/s)

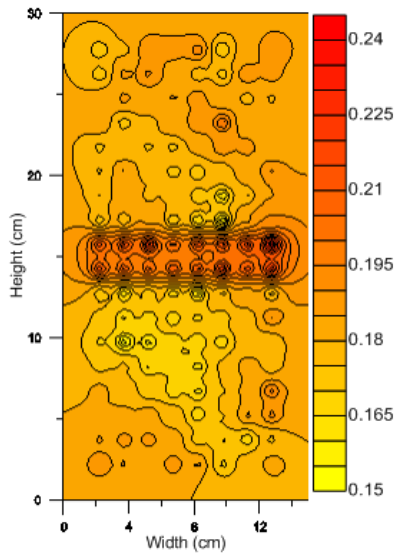

Figure 4-46 Porosity at 4.5 % axial strain (0.05 m/s)

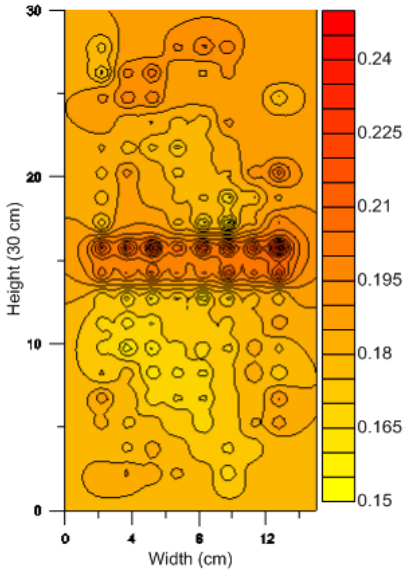

Figure 4-47 Porosity at 4.5 % axial strain (0.005 m/s)

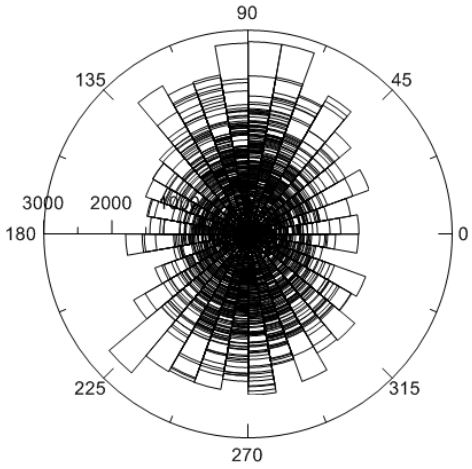

Figure 4-48 Normal force at 1.5 % axial strain (0.05 m/s)

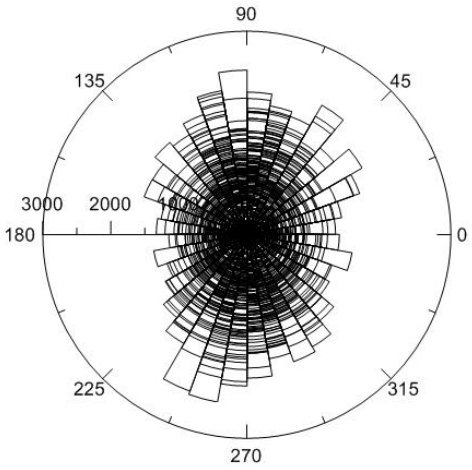

Figure 4-49 Normal force at 1.5 % axial strain (0.005 m/s)

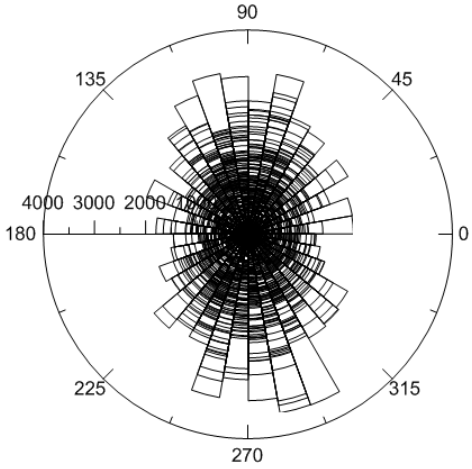

Figure 4-50 Normal force at 4.5 % axial strain (0.05 m/s)

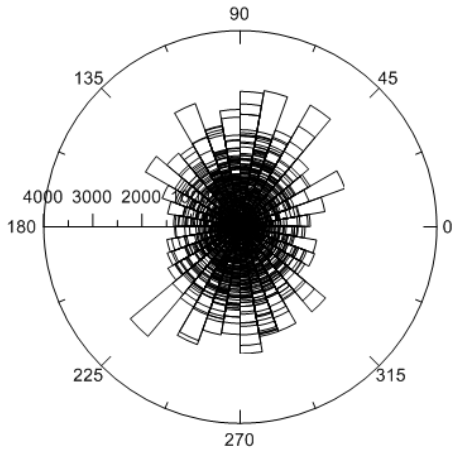

Figure 4-51 Normal force at 4.5 % axial strain (0.005 m/s)

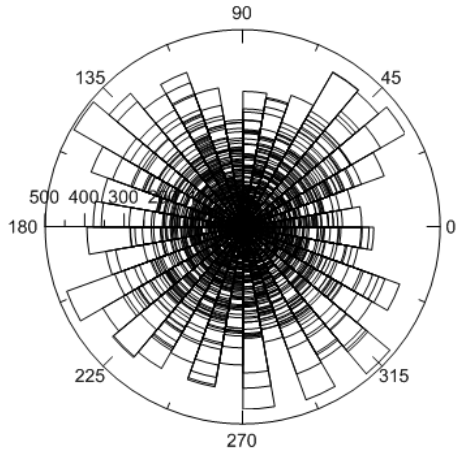

Figure 4-52 Shear force at 0.5 % axial strain (0.05 m/s)

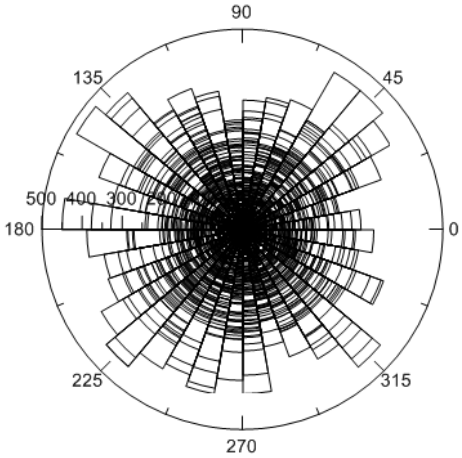

Figure 4-53 Shear force at 0.5 % axial strain (0.005 m/s)

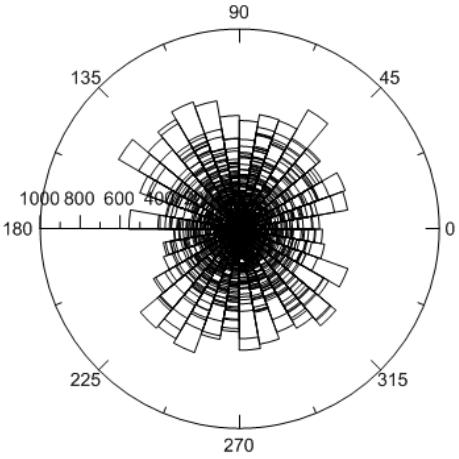

Figure 4-54 Shear force at 1.5 % axial strain (0.05 m/s)

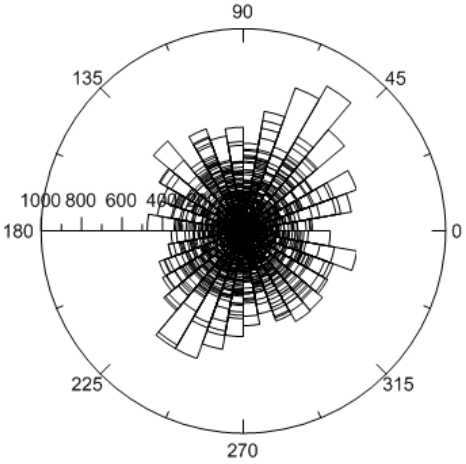

Figure 4-55 Shear force at 1.5 % axial strain (0.005 m/s)

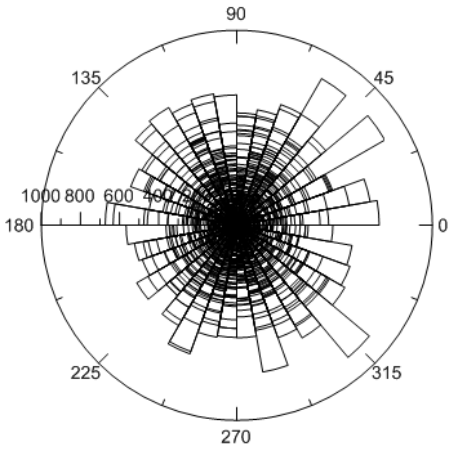

Figure 4-56 Orientation of shearing force at 4.5 % axial strain (0.05 m/s)

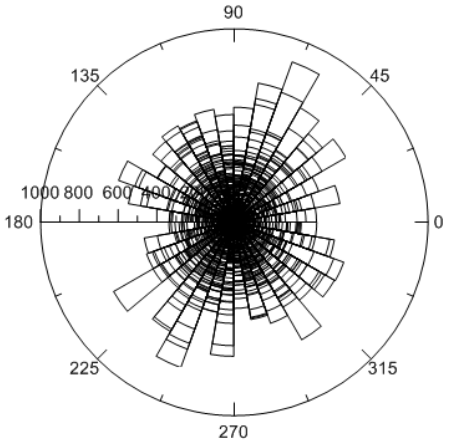

Figure 4-57 Orientation of shearing force at 4.5 % axial strain (0.005 m/s)

4.6.2 Effect of boundary type

4.6.2.1 Unreinforced circular sample

The stress – strain behavior varied insignificantly with rigid and flexible boundary as shown in Figure 4-58 and the confining pressures ranging from 50 to 1000 kPa. To study the effect of boundary the samples were loaded at optimum rate of 0.005 m/s. In terms of dilation behavior the flexible boundary samples exhibited similar volumetric dilation to that of rigid boundary samples as shown in Figure 4-59. The Energy tracing was performed in samples at confining pressure of 100 kPa. However, it was interesting to see slight deviation in boundary and frictional work in

Figure 4-60. The rigid boundary sample showed reduced boundary and frictional work when compared to flexible boundary. This can be explained by the fact that on rigid boundary stresses were averaged over the length of the boundary where as in flexible boundary, the boundary was able to react to local variation of stresses.

Figure 4-61 show the circular sample assembly at 5 % axial strain at 100 kPa confining pressure. The generation and evolution of porosity contours in rigid and flexile boundary are shown in Figure 4-62 to Figure 4-68 for samples loaded at optimum rate of 0.005 m/s at 100 kPa confining pressure. In the figures 'FB' represents flexible boundary and 'RB' represents rigid boundary. The contours show similarity in evolution of porosity in the samples but the sample with flexible wall produced a distinct diagonal section of high porosity representing shear band which was not as distinct in the sample with rigid boundary as shown in Figure 4-67 and Figure 4-68.

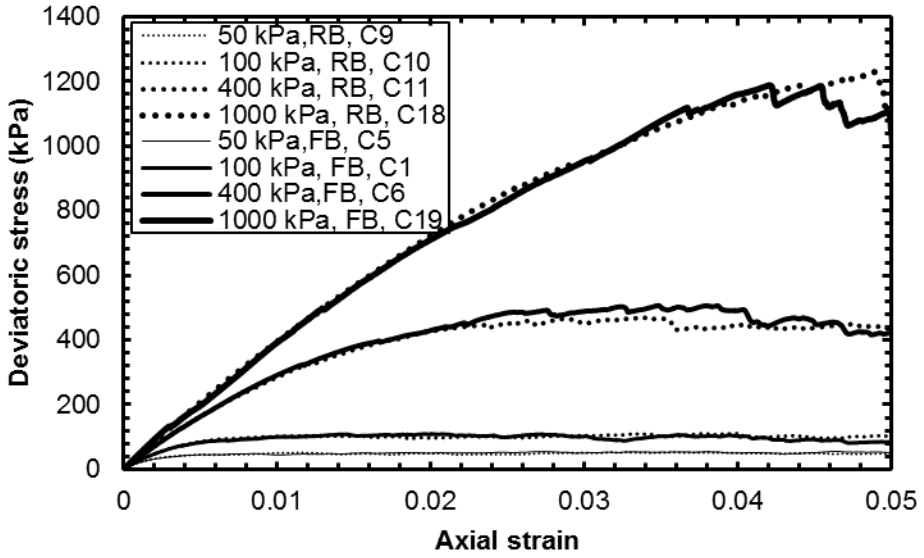

Figure 4-58 Deviatoric stress vs axial strain for optimum loading rate (0.005m m/s) for unreinforced circular samples with flexible (FB) and rigid (RB) boundary

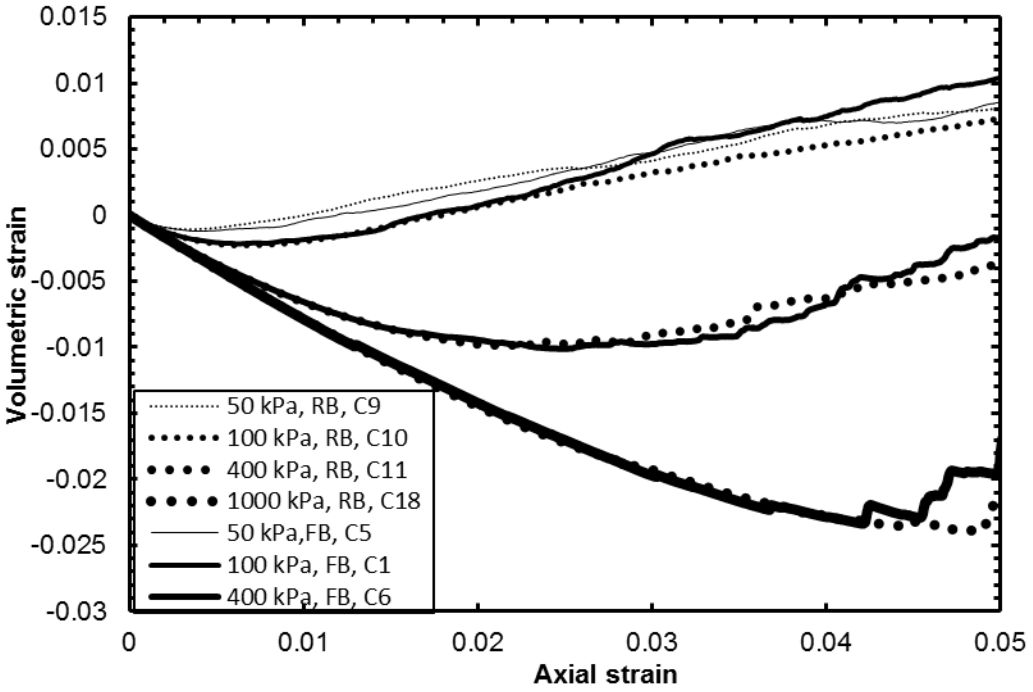

Figure 4-59 Volumetric strain vs axial strain for unreinforced circular samples with flexible (FB) and rigid (RB) boundary

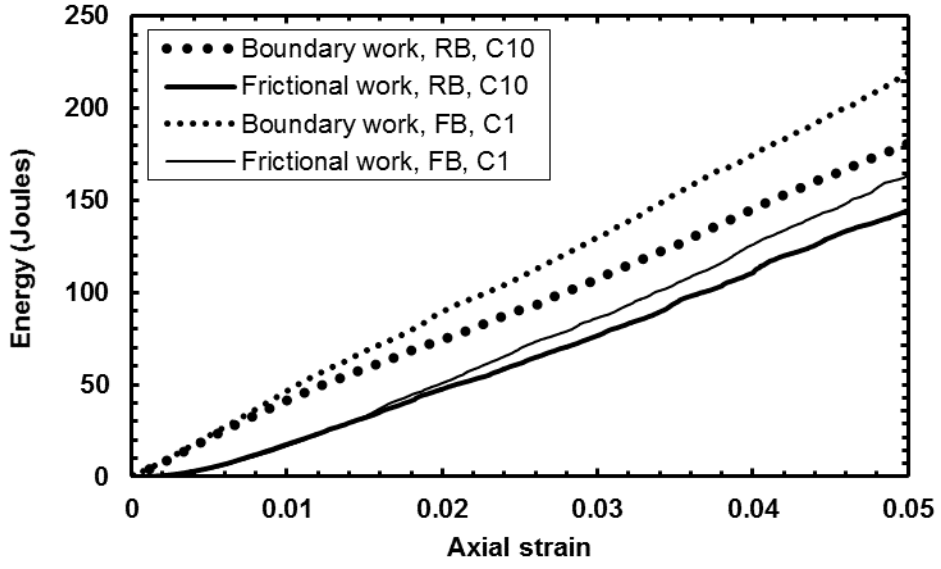

Figure 4-60 Boundary and frictional work for rigid and flexible boundary

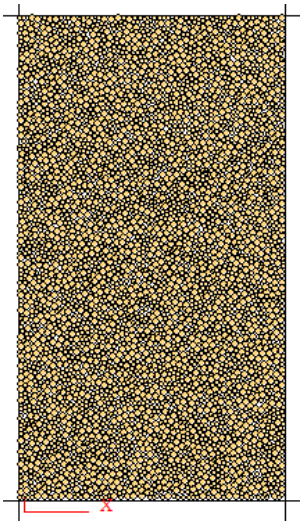

Figure 4-61 Unreinforced sample at 5 % axial strain with rigid wall

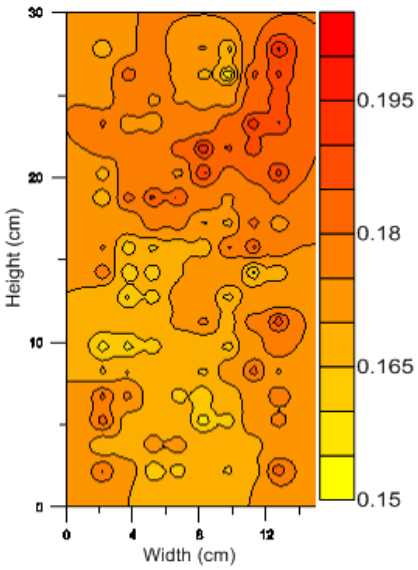

Figure 4-62 Porosity before loading with rigid boundary

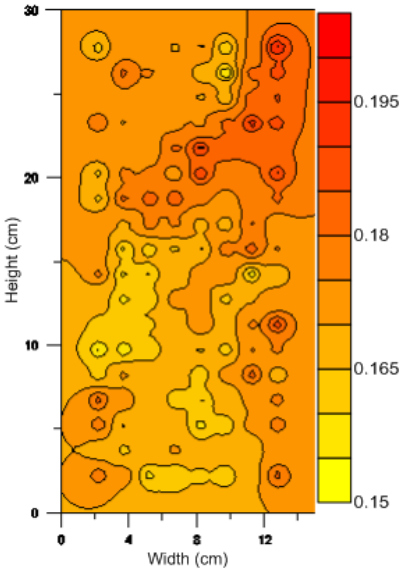

Figure 4-63 Porosity at 0.5 % axial strain (RB)

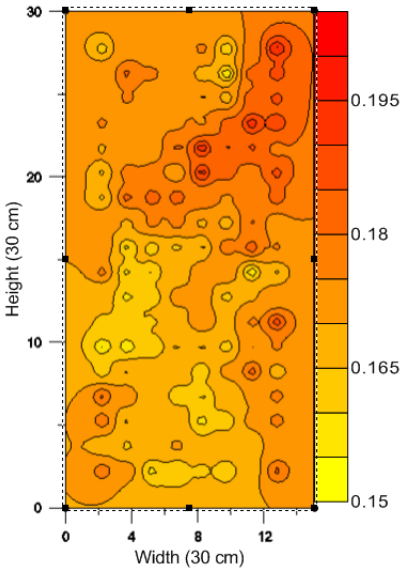

Figure 4-64 Porosity at 0.5 % axial strain (FB)

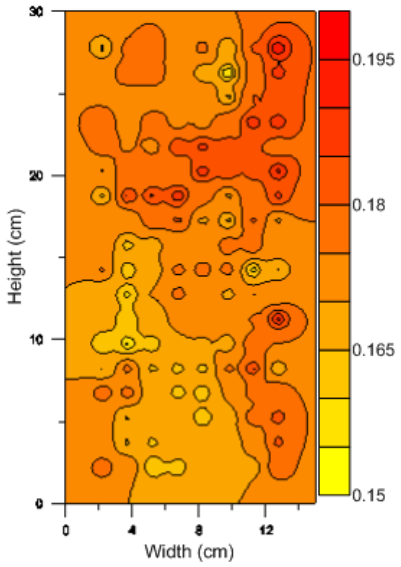

Figure 4-65 Porosity at 1.5 % axial strain (RB)

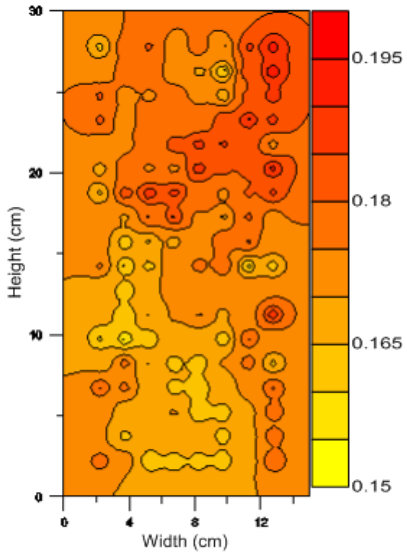

Figure 4-66 Porosity at 1.5 % axial strain (FB)

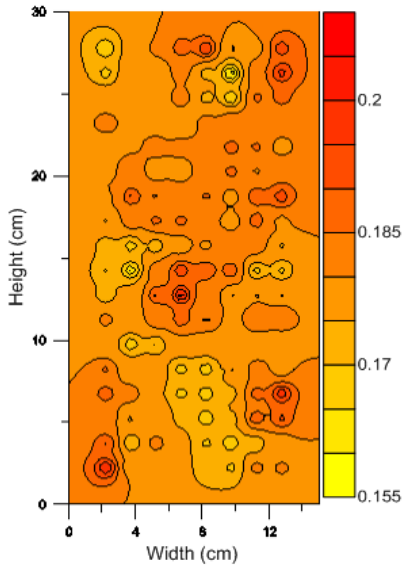

Figure 4-67 Porosity at 4.5 % axial strain (RB)

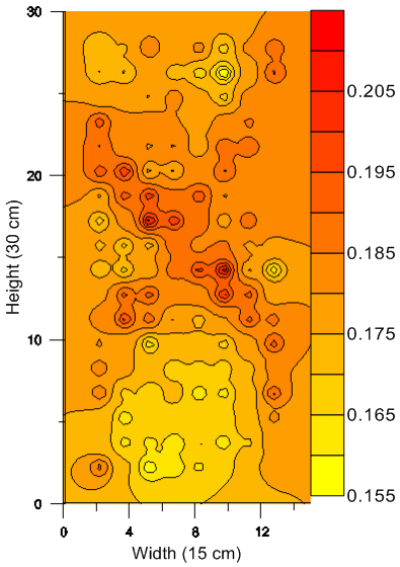

Figure 4-68 Porosity at 4.5 % axial strain (FB)

Figure 4-69 to Figure 4-76 compares the normal and shear forces at 1.5 % and 4.5 % axial strain for rigid boundary and flexible boundary samples. The comparison shows that the normal and shear forces did not vary significantly in terms of magnitude and orientation with boundary type.

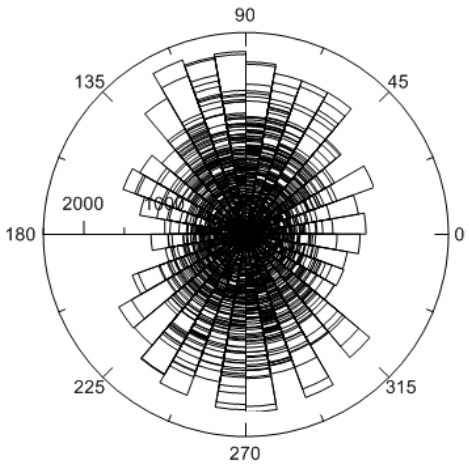

Figure 4-69 Normal force at 1.5 % axial strain (RB)

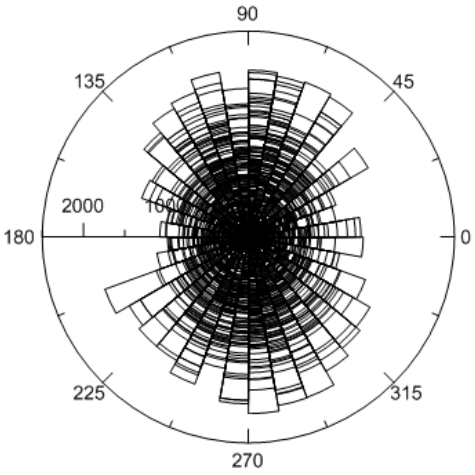

Figure 4-70 Normal force at 1.5 % axial strain (FB)

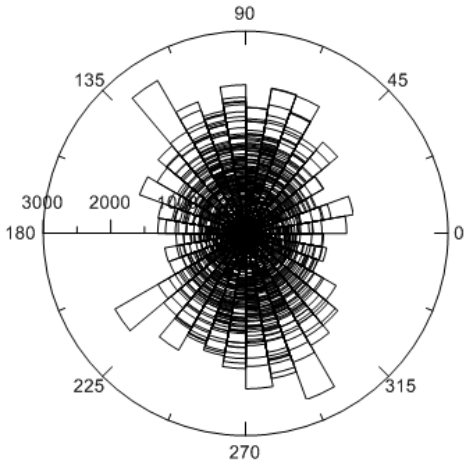

Figure 4-71 Normal force at 4.5 % axial strain (RB)

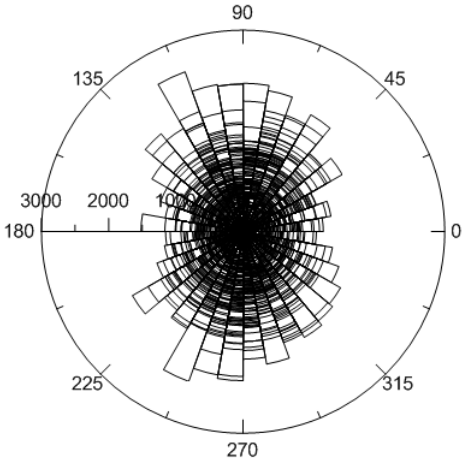

Figure 4-72 Normal force at 4.5 % axial strain (FB)

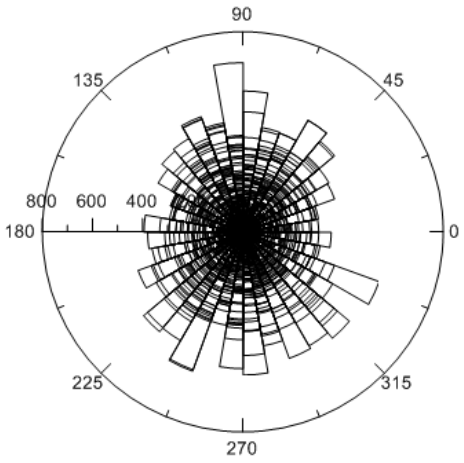

Figure 4-73 Shear force at 1.5 % axial strain (RB)

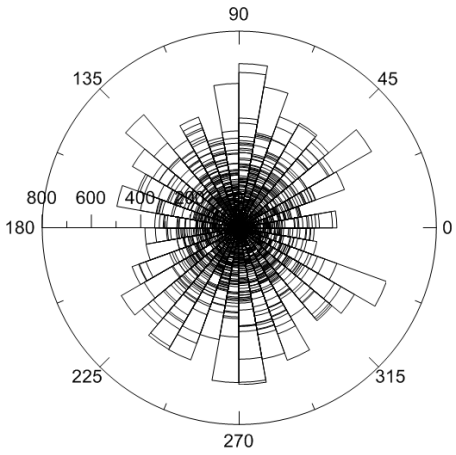

Figure 4-74 Shear force at 1.5 % axial strain (FB)

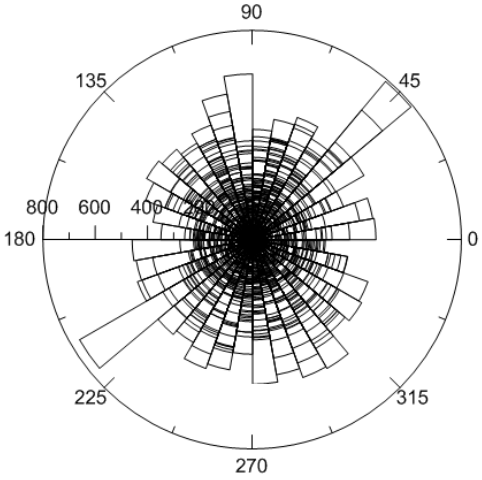

Figure 4-75 Shear force at 4.5 % axial strain (RB)

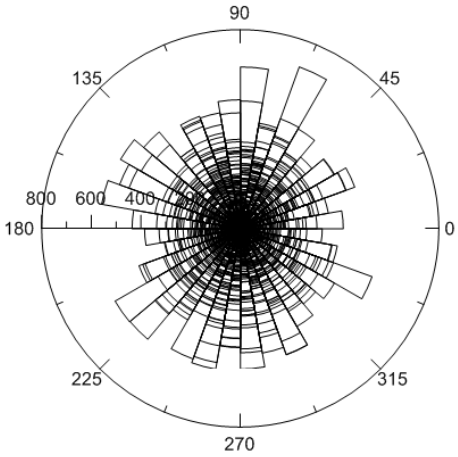

Figure 4-76 Shear force at 4.5 % axial strain (FB)

4.6.2.2 Geogrid reinforced circular sample

Geogrid reinforced samples did not behave differently with rigid and flexible boundary in terms of stress – strain relationship as shown in Figure 4-77. The samples

were loaded at the optimum loading rate of 0.005 m/s. The stress – strain relationships were found to be similar at confining pressure of 50 kPa, 100 kPa, and 400 kPa. The volumetric dilation behavior did not vary significantly at confining pressure of 400 kPa but significant differences were observed at lower confining pressures of 50 kPa and 100 kPa as shown in Figure 4-78. At lower confining pressures, the rigid boundary samples showed higher volumetric dilation compared to flexible boundary. In terms of boundary work and frictional work the differences were not significant but the rigid boundary showed slightly higher boundary and frictional work after 2 % axial strain as shown in Figure 4-79.

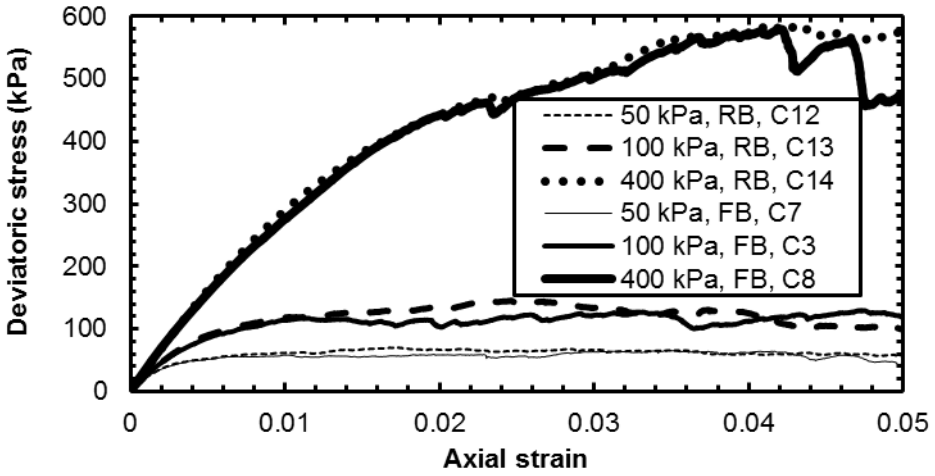

Figure 4-77 Deviatoric stress vs axial strain for optimum loading rate (0.005m m/s) for reinforced circular samples with flexible (FB) and rigid (RB) boundary

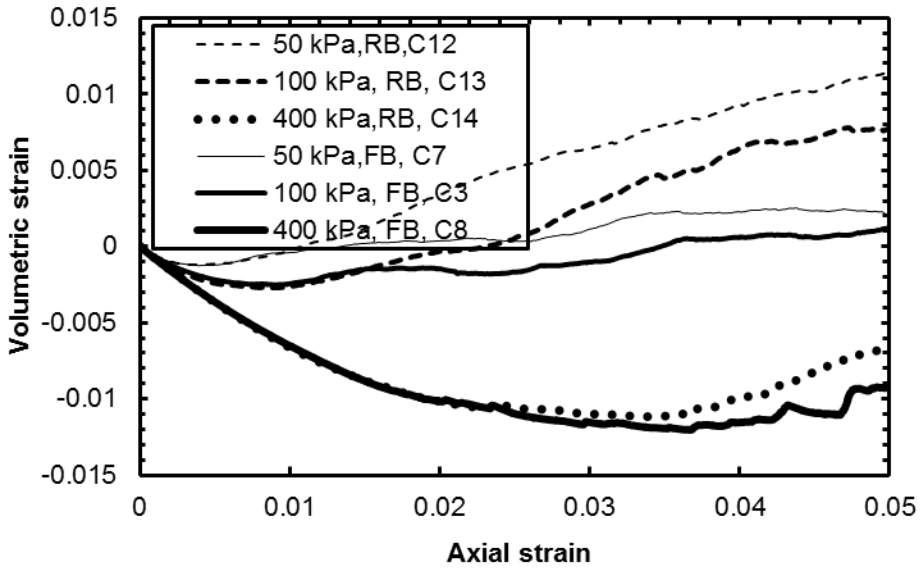

Figure 4-78 Volumetric strain vs axial strain for reinforced circular samples with flexible (FB) and rigid (RB) boundary

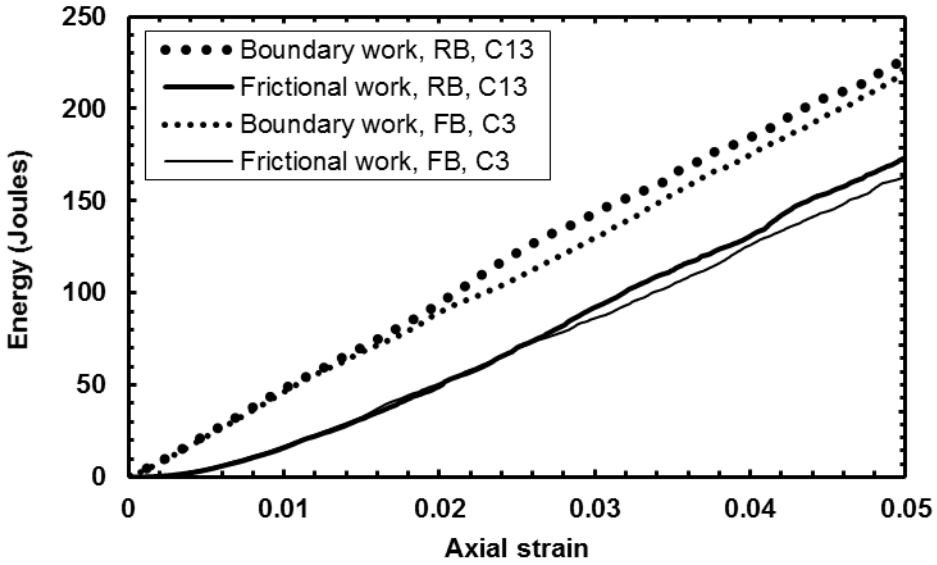

Figure 4-79 Boundary and frictional work for rigid and flexible boundary for reinforced circular sample

Figure 4-80 to Figure 4-83 shows the evolution of porosity in the geogrid reinforced circular sample with rigid boundary loaded at optimum loading rate. The porosity contours show that the rigid boundary sample finally achieve higher porosity than the flexible boundary sample based on the color scale. This fact is also supported by the higher volumetric dilation observed by the samples with rigid boundary as shown in Figure 4-78. Figure 4-84 to Figure 4-87 show the evolution of magnitude and orientation of normal and shear forces in the rigid boundary sample. The shear forces in Figure 4-86 and Figure 4-87 when compared to Figure 4-53 and Figure 4-55 did not show any significant variations due to boundary conditions.

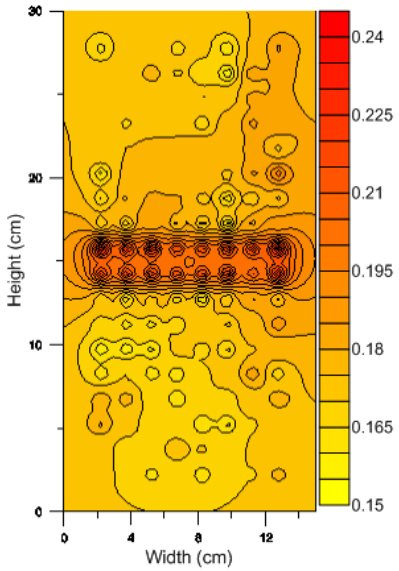

Figure 4-80 Porosity just before loading (RB)

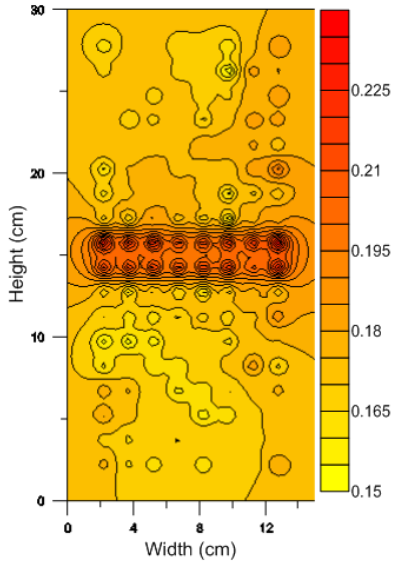

Figure 4-81 Porosity at 0.5 % axial strain (RB)

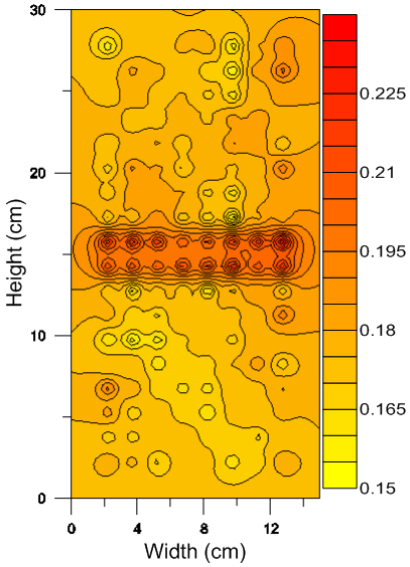

Figure 4-82 Porosity at 2.5 % axial strain (RB)

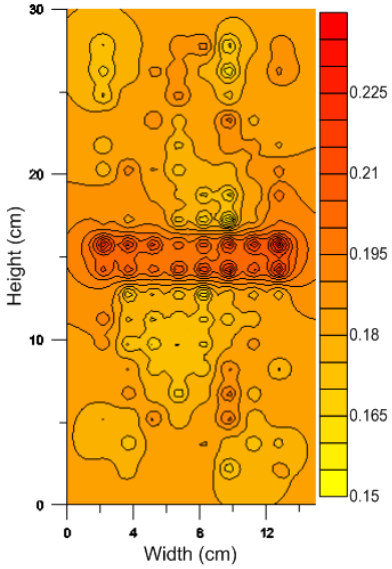

Figure 4-83 Porosity at 4.5 % axial strain (RB)

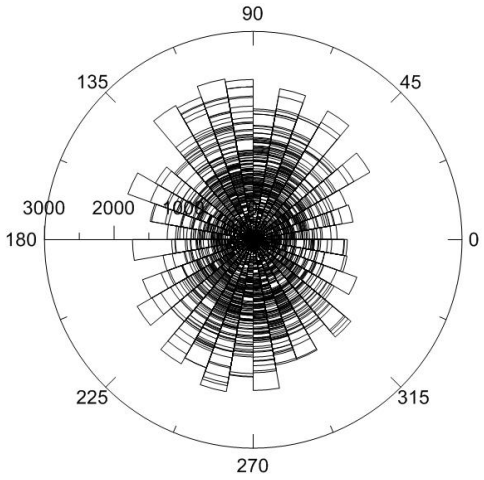

Figure 4-84 Normal force at 1.5 % axial strain (RB)

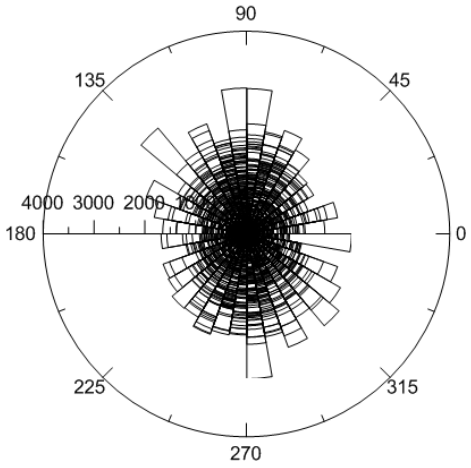

Figure 4-85 Normal force at 4.5 % axial strain (RB)

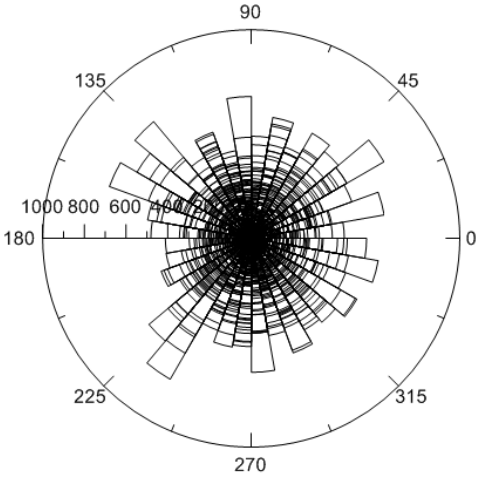

Figure 4-86 Shear force at 1.5 % axial strain (RB)

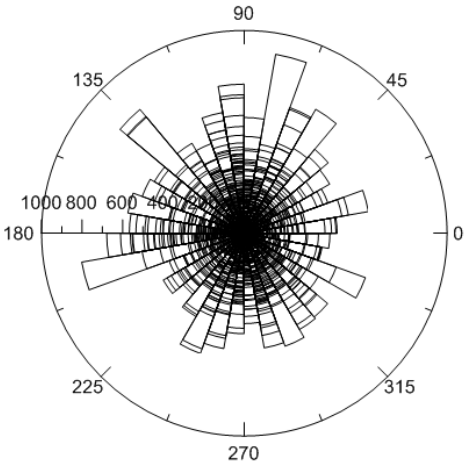

Figure 4-87 Shear force at 4.5 % axial strain (RB)

4.6.3 Effect of particle shape

4.6.3.1 Unreinforced clump sample

Unreinforced clump particle assembly were loaded at optimum loading rate of 0.005 m/s and faster loading rate of 0.05 m/s to study the effect of loading rate on particle shape with flexible boundary. The loading rate had similar effect on clump particles too as in circular particles, only the effect was amplified as shown in Figure 4-88. In term of volumetric behavior, the behavior did not vary much with respect to loading rate as shown in Figure 4-89.

In terms of energy, the energy dissipation due to frictional losses were similar for both faster and slower loading rates as in the case of circular samples as shown in Figure 4-90. Similarly, the faster loading rate produced higher boundary work and slower loading rate produced lower boundary work. Hence, in the case of the clumps too, the higher deviatoric stress due to faster loading rate did not result from the increase in shear strength of the sample.

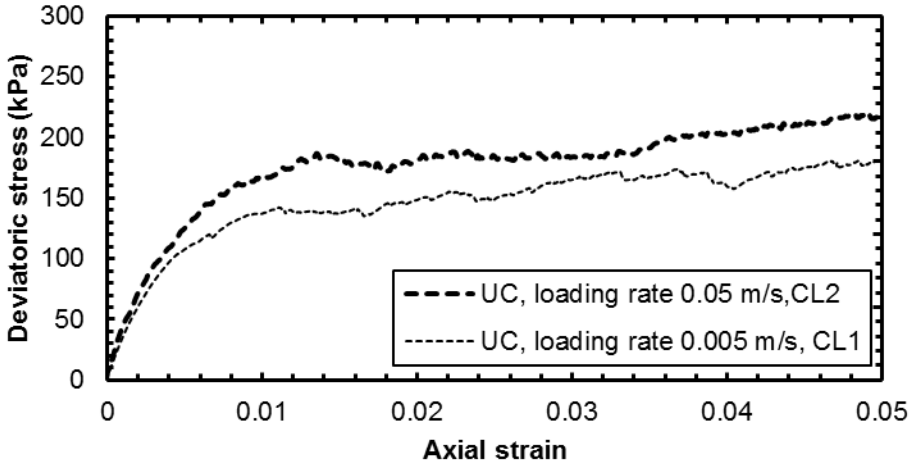

Figure 4-88 Deviatoric stress vs axial strain for optimum loading rate (0.005m m/s) for unreinforced clump sample with flexible boundary

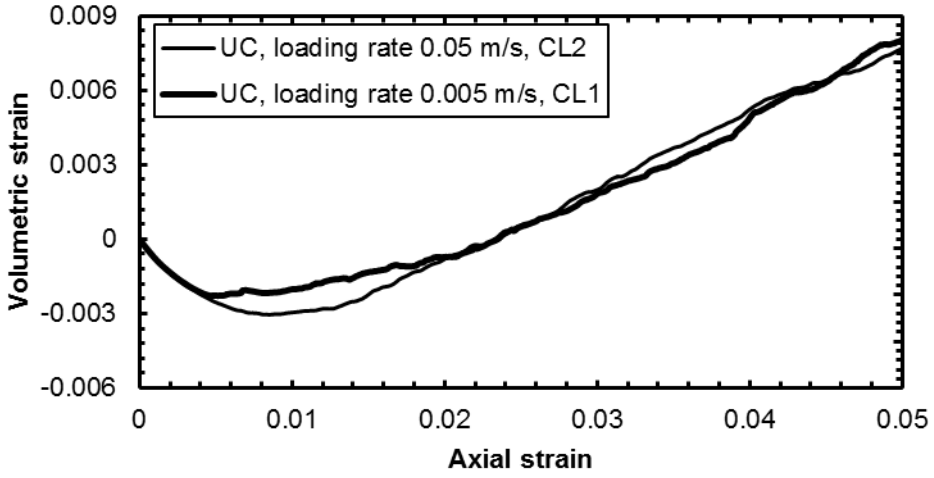

Figure 4-89 Volumetric strain vs axial strain for unreinforced clump with flexible boundary

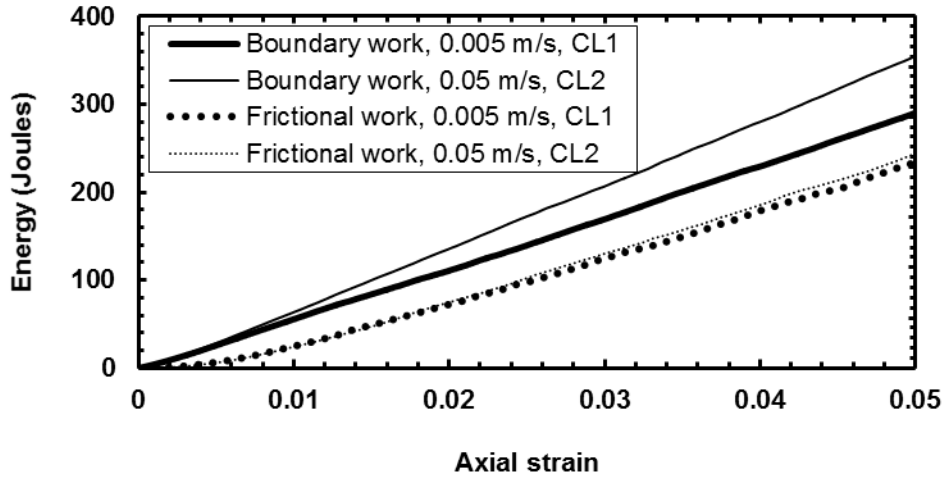

Figure 4-90 Boundary and frictional work for boundary for reinforced clump sample

Figure 4-91 shows the biaxial clump sample with flexible boundary loaded at 0.005 m/s at 5 % axial strain and Figure 4-92 shows the porosity contour in the sample before loading. Figure 4-93 to Figure 4-96 shows the evolution of porosity in the sample loaded at different rates. The optimum loading rate caused the low porosity areas to

coalesce and finally form a band of low porosity area diagonally across the sample resembling shear bands.

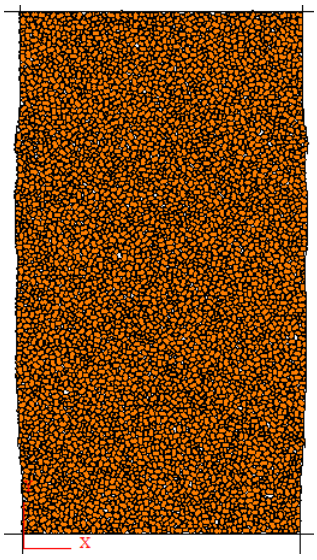

Figure 4-91 Unreinforced sample at 4.5 % axial strain with flexible wall

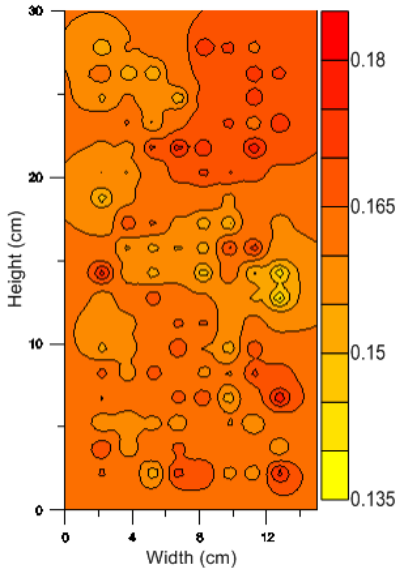

Figure 4-92 Porosity before loading

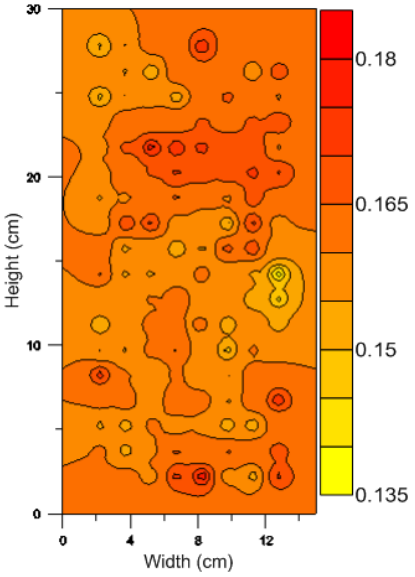

Figure 4-93 Porosity at 1.5 % axial strain (0.05 m/s)

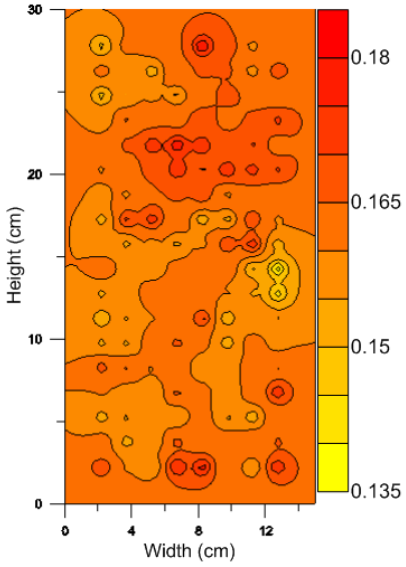

Figure 4-94 Porosity at 0.5 % axial strain (0.005 m/s)

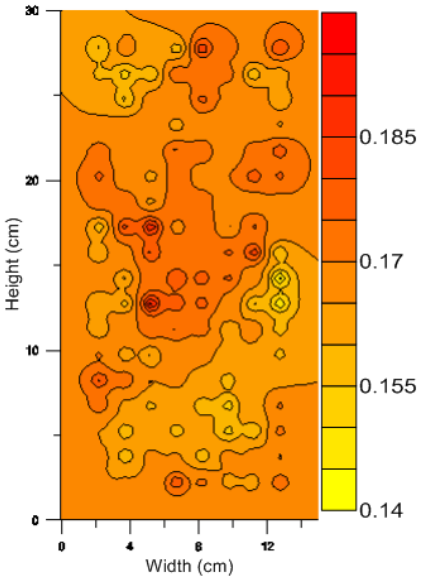

Figure 4-95 Porosity at 4.5 % axial strain (0.05 m/s)

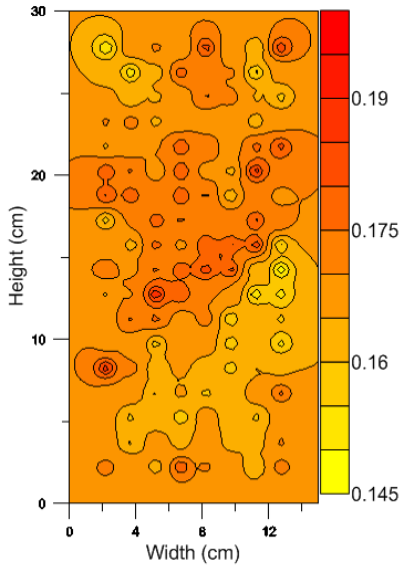

Figure 4-96 Porosity at 4.5 % axial strain (0.005 m/s)

Figure 4-97 shows the contact orientations in the sample just before loading. The almost circular shape shows that clump replacement technique worked properly creating an isotropic sample in terms of contact orientations which is also supported by the normal contact force orientation and magnitude in Figure 4-98. Figure 4-99 to Figure 4-102 show the normal force orientation and magnitude in the assembly at different loading stages and they show that the faster loading rate produced higher normal contact forces. Figure 4-101 to Figure 4-104 show the evolution of shear forces in the samples at different loading rates. The shear forces in sample loaded at faster loading rate showed slightly higher shear forces graphically and is supported by slightly higher frictional energy dissipated shown in Figure 4-90.

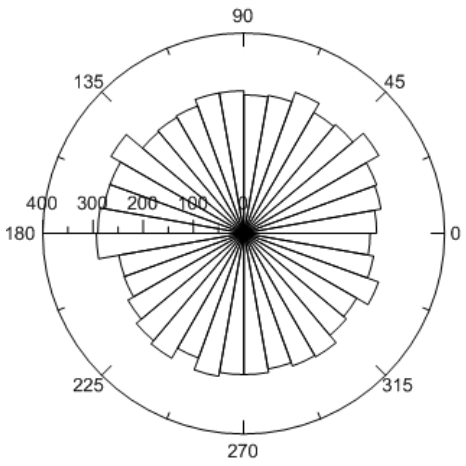

Figure 4-97 Contact orientation just before loading

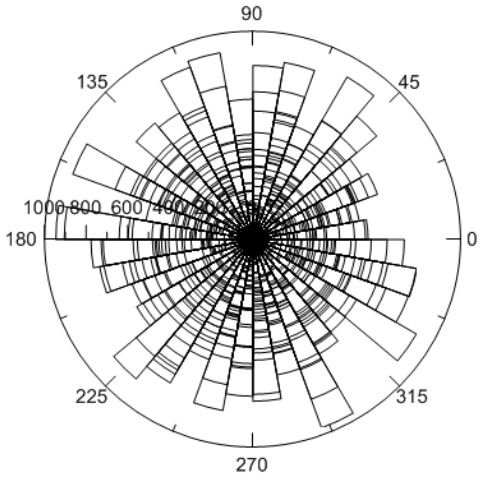

Figure 4-98 Normal force just before loading

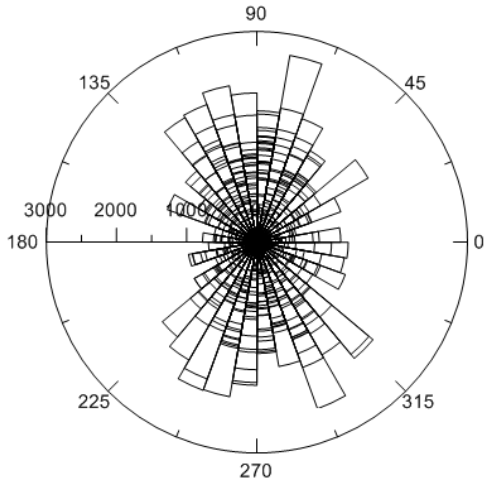

Figure 4-99 Normal forces at 1.5 % axial strain (0.05 m/s)

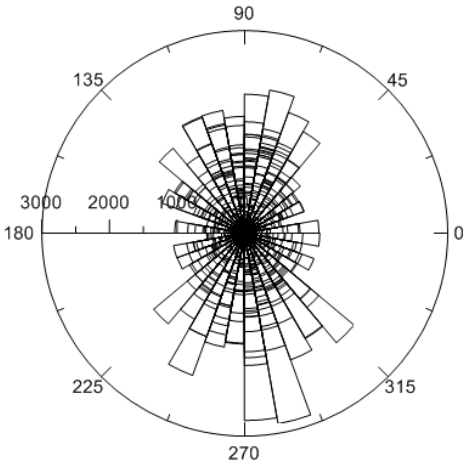

Figure 4-100 Normal forces at 1.5 % axial strain (0.005 m/s)

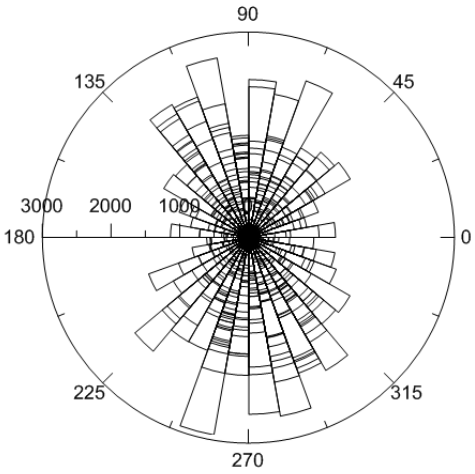

Figure 4-101 Normal forces at 4.5 % axial strain (0.05 m/s)

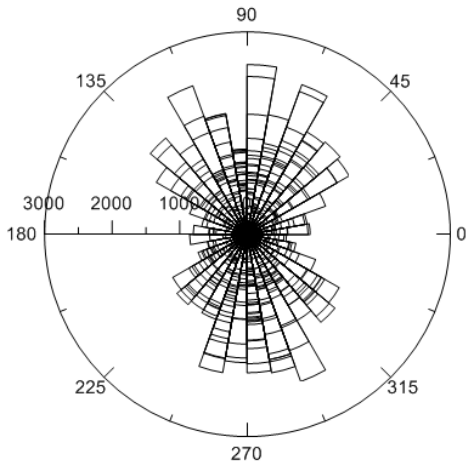

Figure 4-102 Normal forces at 4.5 % axial strain (0.005 m/s)

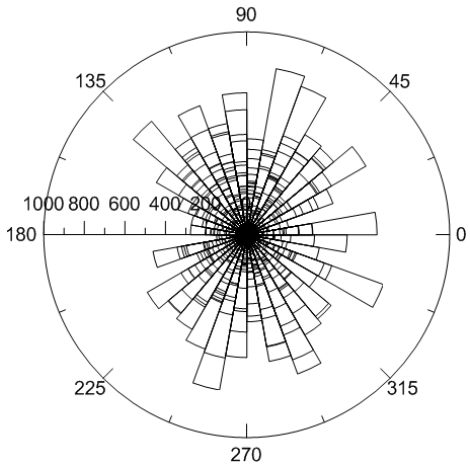

Figure 4-103 Shear force at 1.5 % axial strain (0.05 m/s)

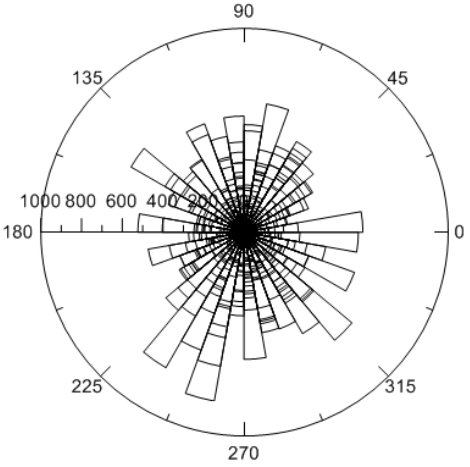

Figure 4-104 Shear force at 1.5 % axial strain (0.005 m/s)

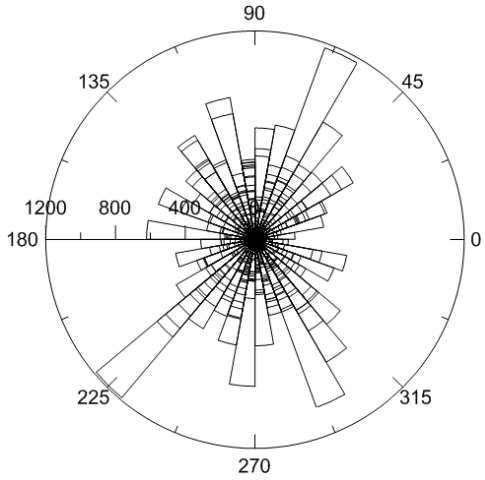

Figure 4-105 Shear force at 4.5 % axial strain (0.05 m/s)

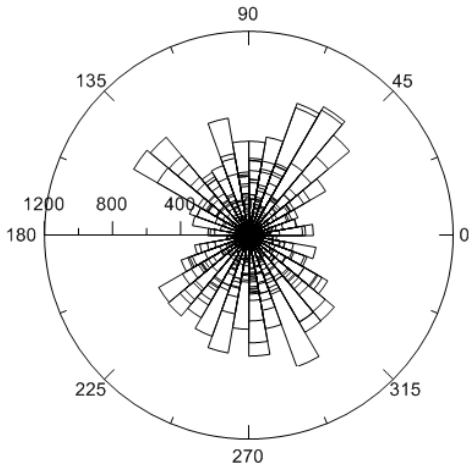

Figure 4-106 Shear force at 4.5 % axial strain (0.005 m/s)

4.6.3.2 Reinforced clump sample

Clump sample was reinforced by putting a single layer of geogrid reinforcement at the mid height of the sample. The sample was then loaded at faster loading rate of 0.05 m/s and slower loading rate of 0.005 m/s with flexible boundary. The faster loading rate produced significantly higher deviatoric stresses in the reinforced clump sample when compared to unreinforced sample as shown in Figure 4-107. Also the reinforced sample went significantly lower volumetric dilation than the unreinforced sample.

The frictional energy dissipated was similar for both the loading rates but as usual the boundary work was higher for the sample loaded with the faster loading rate as shown inFigure 4-109.

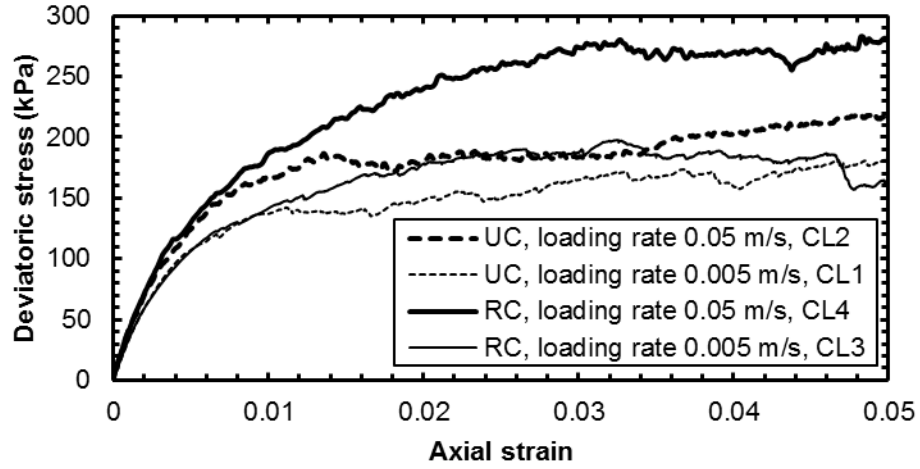

Figure 4-107 Deviatoric stress vs axial strain for different loading rates for reinforced and unreinforced clump samples with flexible boundary (UC – unreinforced clump, RC – reinforced clump)

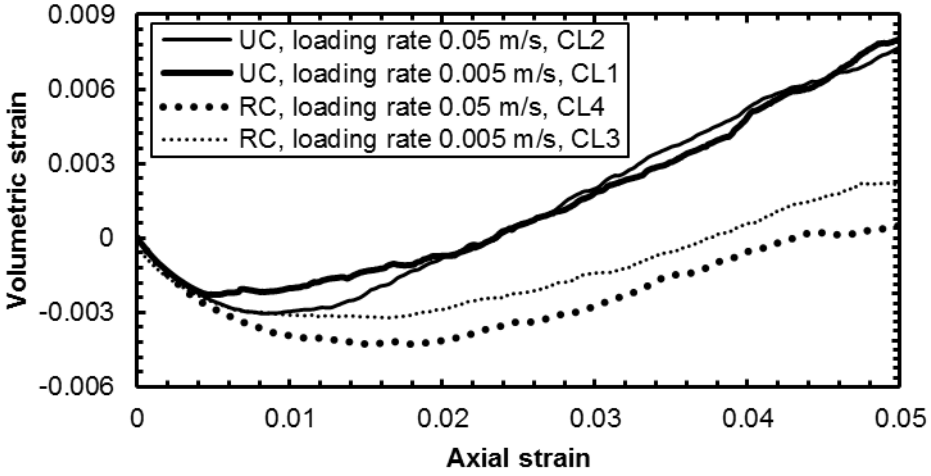

Figure 4-108 Volumetric strain vs axial strain for reinforced and unreinforced clump with flexible boundary

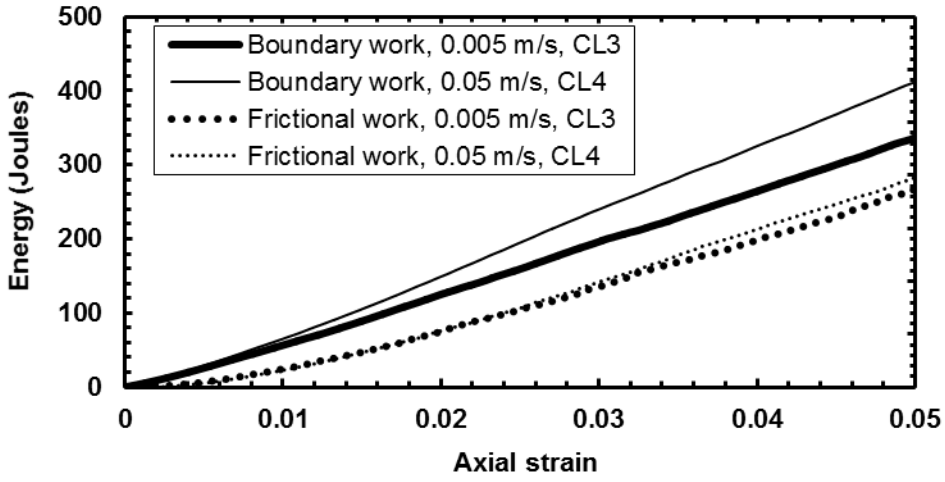

Figure 4-109 Boundary and frictional work for boundary for reinforced clump sample

Figure 4-110 shows the reinforced clump sample with flexible boundary loaded at 0.005 m/s at 5 % of axial strain. Figure 4-111 to Figure 4-115 show the evolution of porosity in the reinforced samples with different loading rates. When the Figure 4-114 and Figure 4-115 are compared we can observe larger areas of higher porosity in the sample loaded at slower loading rate of 0.005 m/s. This is also supported by the higher volumetric dilation in the slowly loaded sample as shown in Figure 4-108.

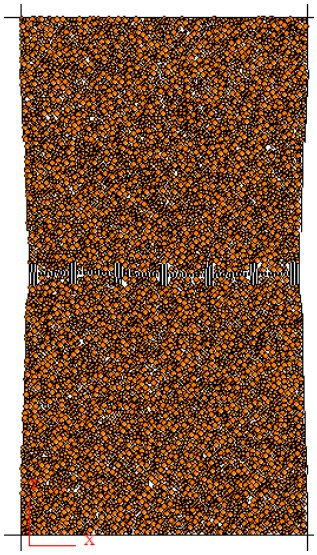

Figure 4-110 Reinforced sample at 5 % axial strain with flexible wall

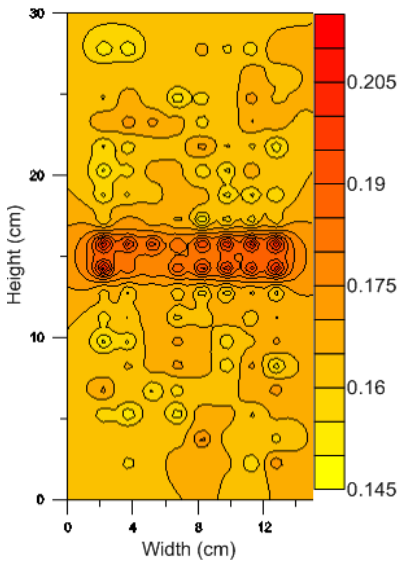

Figure 4-111 Porosity before loading

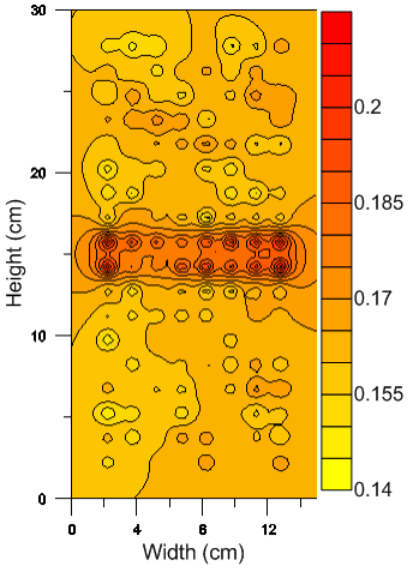

Figure 4-112 Porosity at 1.5 % axial strain (0.05 m/s)

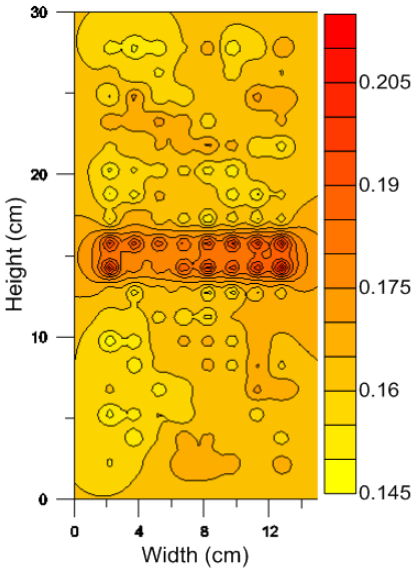

Figure 4-113 Porosity at 1.5 % axial strain (0.005 m/s)

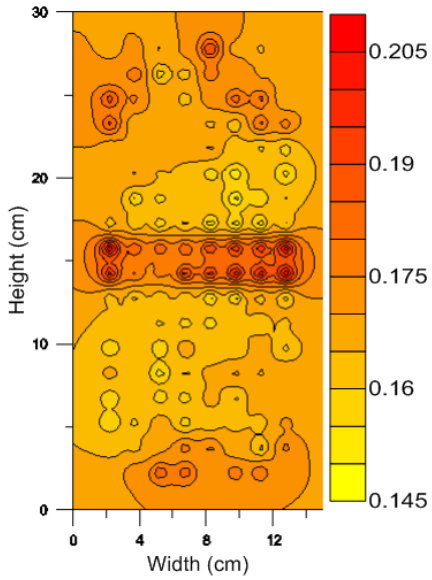

Figure 4-114 Porosity at 4.5 % axial strain (0.05 m/s)

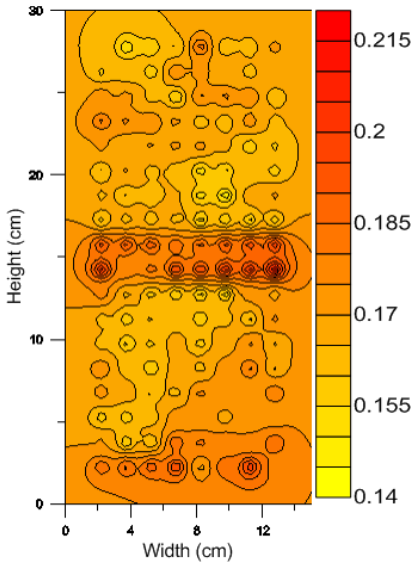

Figure 4-115 Porosity at 4.5 % axial strain (0.005 m/s)

Figure 4-116 to Figure 4-123 show the evolution of normal and shear forces in the clump sample for different loading rates. The normal forces in the faster loaded sample are higher than in the slowly loaded sample. Except for some isolated high shear forces, they remained similar for both rates of loading.

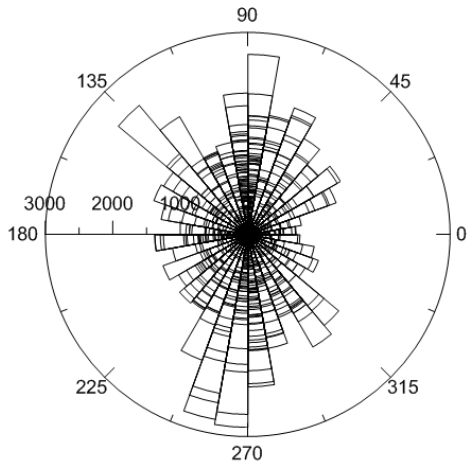

Figure 4-116 Normal force at 1.5 % axial strain (0.05 m/s)

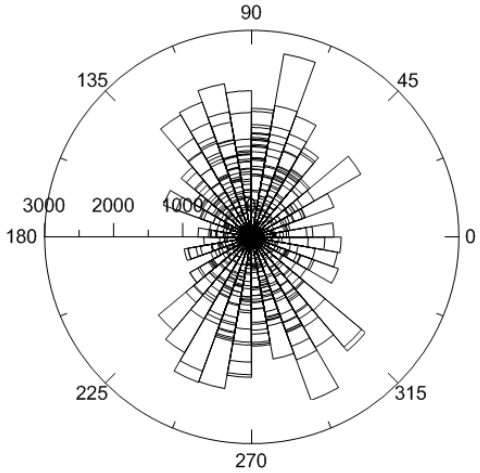

Figure 4-117 Normal force at 1.5 % axial strain (0.005 m/s)

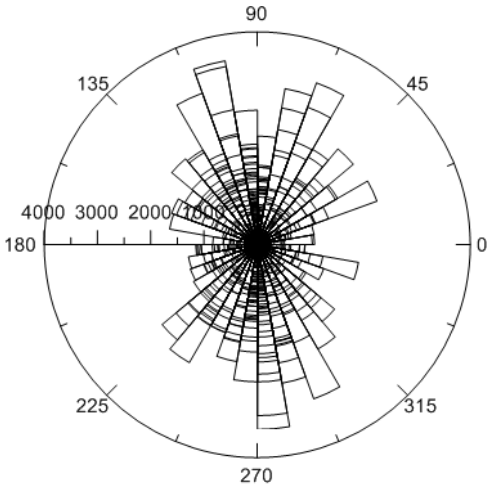

Figure 4-118 Normal force at 4.5 % axial strain (0.05 m/s)

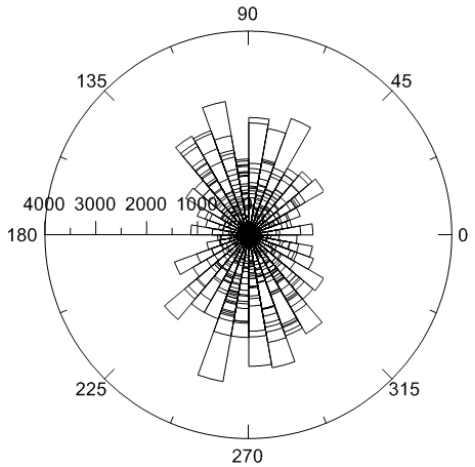

Figure 4-119 Normal force at 4.5 % axial strain (0.005 m/s)

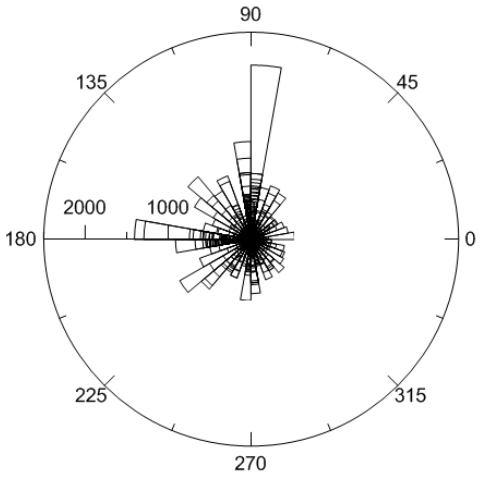

Figure 4-120 Shear force at 1.5 % axial strain (0.05 m/s)

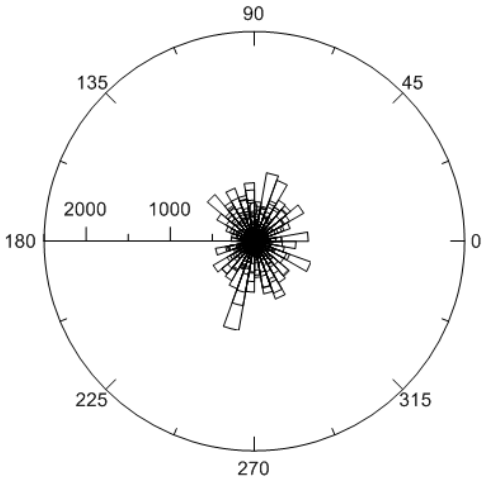

Figure 4-121 Shear force at 1.5 % axial strain (0.005 m/s)

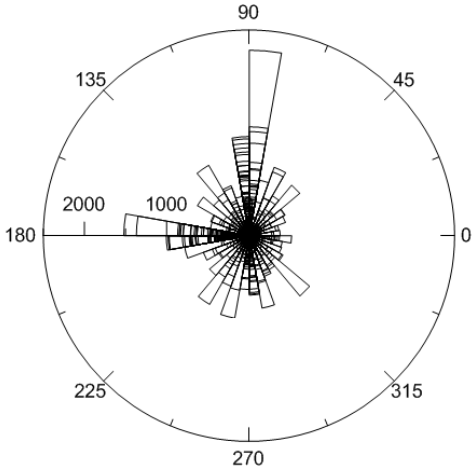

Figure 4-122 Shear force at 4.5 % axial strain (0.05 m/s)

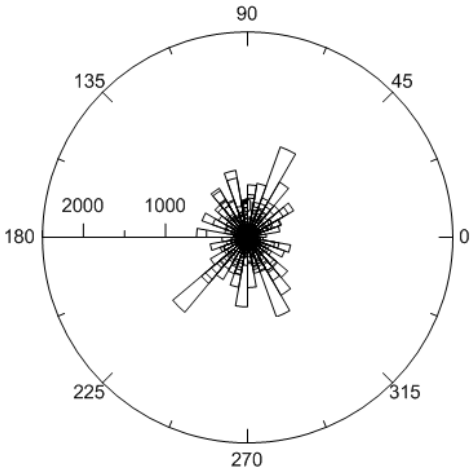

Figure 4-123 Shear force at 4.5 % axial strain (0.005 m/s)

4.6.4 Particle rotation

An advantage of numerical models such as DEM is that we can investigate what happens with each particle in terms of forces acting on it and its movements. During the

simulations of circular and clump particles, their rotations were monitored to provide deeper understanding on how particles interacted with each other. The particle rotations were taken as the difference between cumulative particle rotation at 5 % axial strain and just before loading. This provided the rotations the particles underwent from the beginning of loading until 5 % axial strain. Figure 4-124 to Figure 4-129 present these rotations. The x-axis is accumulated rotation in degree and the y-axis is the height along the sample.

The circular particle with flexible boundary displayed higher rotations around the mid height which matches the bulging at the mid height of the sample as shown in Figure 4-25. Higher rate of loading caused smaller particle rotation as in Figure 4-125 as well the rigid boundary as shown in Figure 4-126. Particles had uniform rotations throughout the sample height in the case of rigid walls. Particle rotations were reduced in the geogrid vicinity signifying some kind of interlocking effect of geogrid as seen in Figure 4-127 and Figure 4-129. Also, clump particles showed reduced particles rotations than circular particles both in the case of reinforced and unreinforced samples

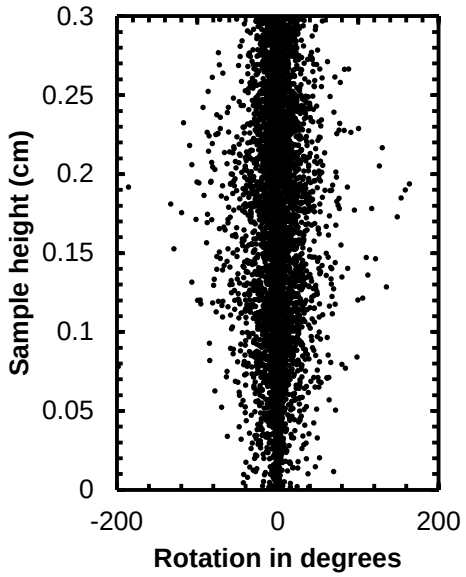

Figure 4-124 Rotation of circular particles with flexible boundary and loaded at 0.005 m/s

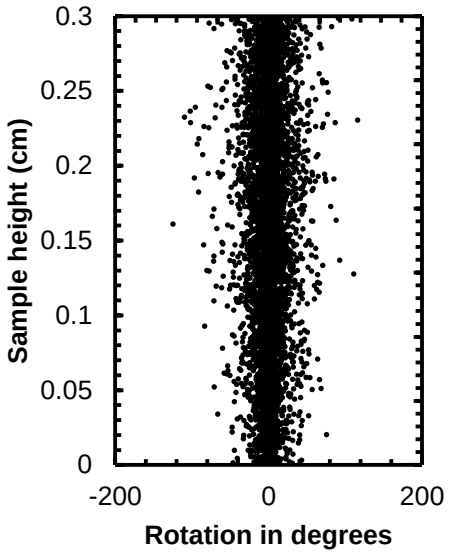

Figure 4-125 Rotation of circular particles with flexible boundary and loaded at 0.05 m/s

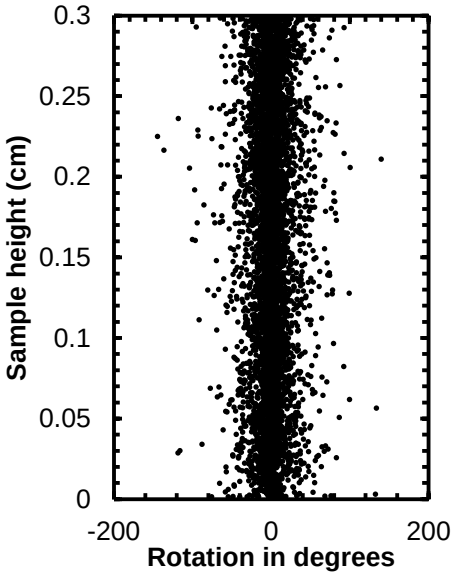

Figure 4-126 Rotation of circular particles with rigid boundary and loaded at 0.005

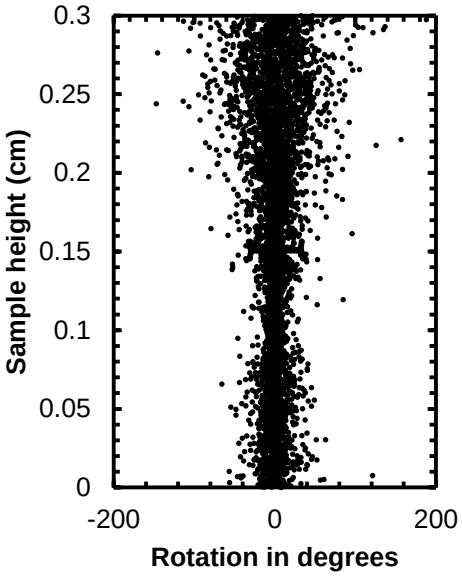

Figure 4-127 Rotation of circular particles reinforced with geogrid, flexible boundary

m/s

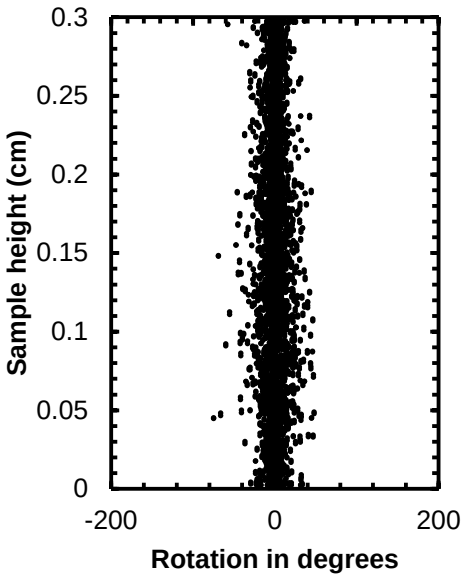

Figure 4-128 Rotation of clump particles with flexible boundary and loaded at 0.005 m/s

and loaded at 0.005 m/s

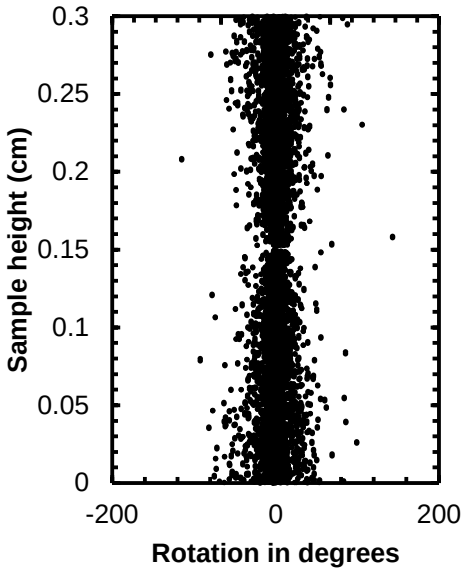

Figure 4-129 Rotation of clump particles reinforced with geogrid, flexible boundary and loaded at 0.005 m/s

4.6.5 Effect of 3 layers of geogrid in circular samples

A biaxial sample was reinforced with three layers of geogrid and loaded at optimum rate of 0.005 m/s. The sample was circular particle assembly with flexible boundaries.Figure 4-130 shows that the sample with three layers of reinforcement showed maximum increase in deviatoric stress as compared to single layer of geogrid reinforcement. With multiple layers of geogrid the sample showed distinct behavior in terms of volumetric dilation as shown in Figure 4-131. While the unreinforced and single layer reinforced samples were dilating the multiple layer reinforced sample was still compressing. The increase in peak deviatoric stress is due to the result of increase in energy dissipated in the form of frictional work as shown in Figure 4-132.

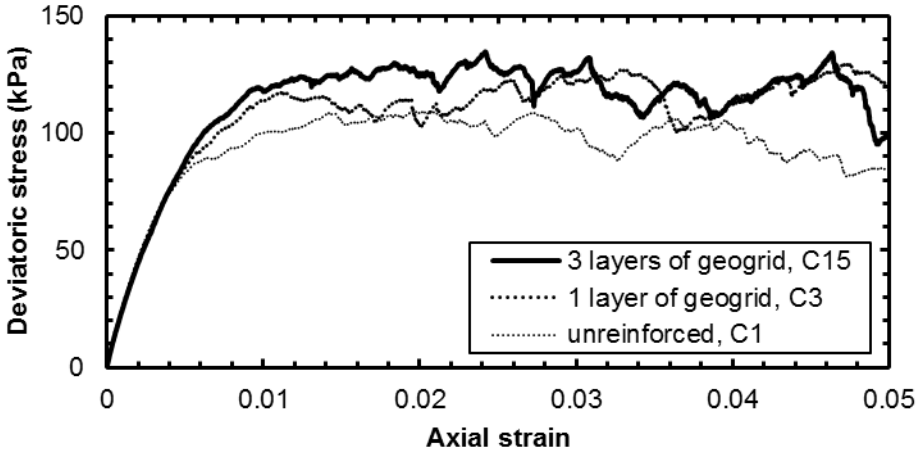

Figure 4-130 Deviatoric stress vs axial strain for three layers of geogrid reinforcement for circular particles

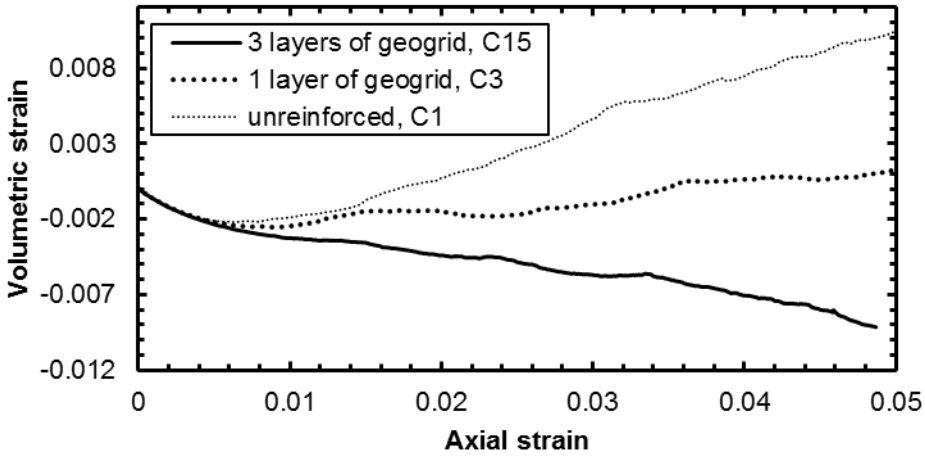

Figure 4-131 Volumetric strain vs axial strain for three layers of geogrid reinforcement for circular particles

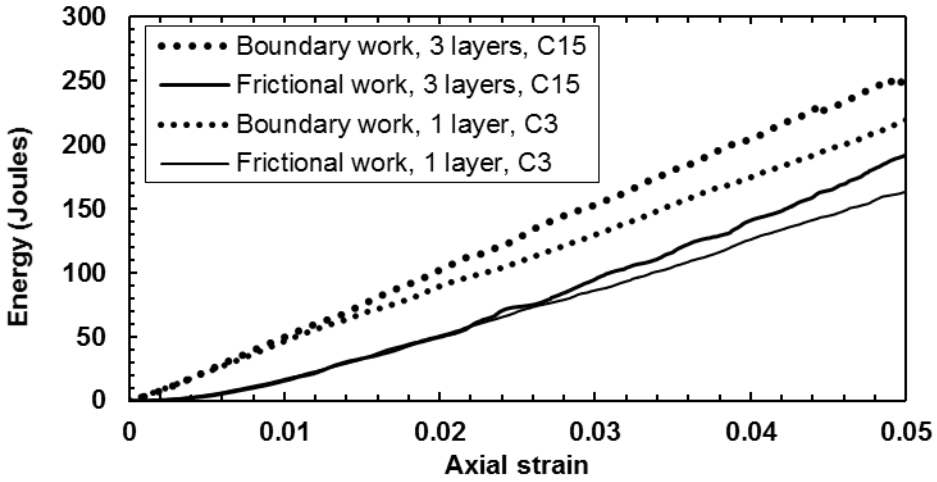

Figure 4-132 Boundary and frictional work for three layers of reinforcement

Figure 4-133 to Figure 4-135 show the evolution of porosity in the sample at various stages. As the axial strain increased the porosity of the sample overall decreased but the area confined within the geogrid layers retain relatively higher porosity. The rotation of particles were also subdued in the vicinity of the geogrid layers as shown in Figure 4-136. Additionally the normal forces and shear forces shown in Figure 4-137 and Figure 4-138 are higher when compared to single layer reinforcement shown in Figure 4-48 and Figure 4-49.

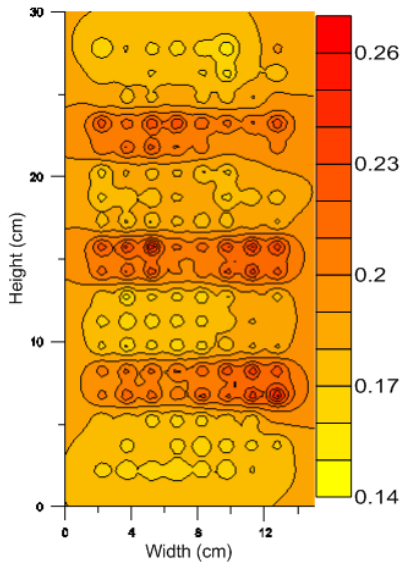

Figure 4-133 Porosity before loading

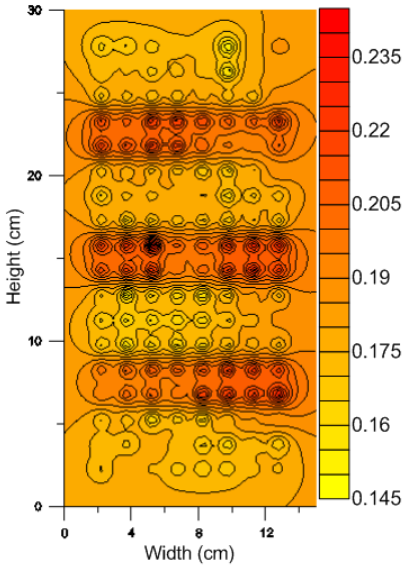

Figure 4-134 Porosity at 2 % axial strain

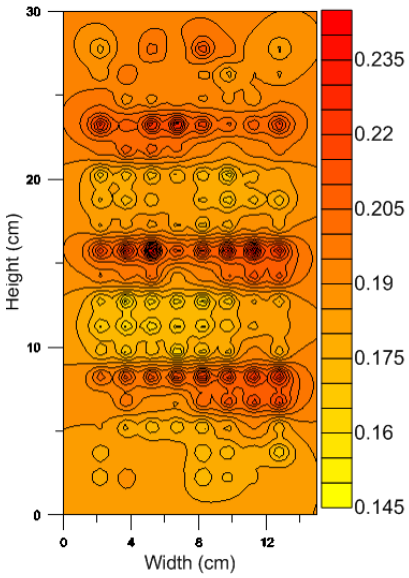

Figure 4-135 Porosity at 4.5 % axial strain

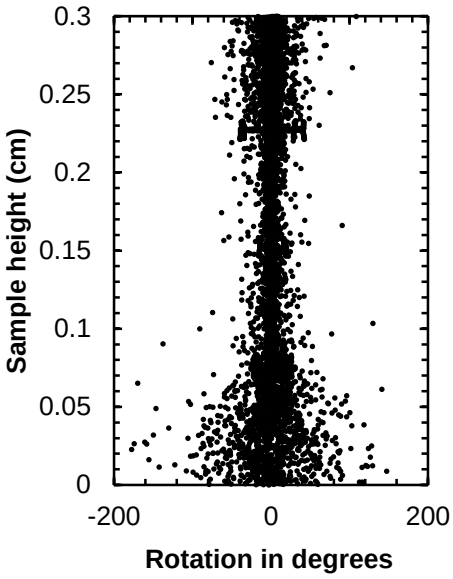

Figure 4-136 Particle rotation

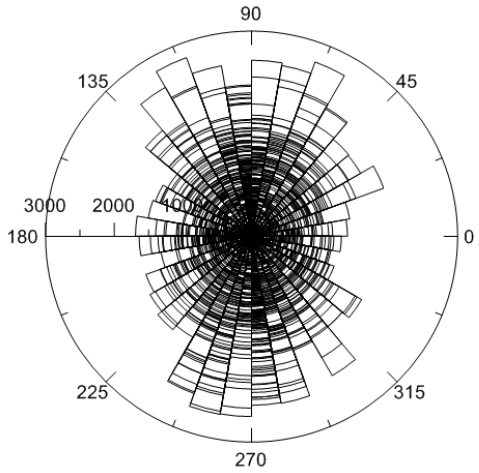

Figure 4-137 Normal force at 2 % axial strain

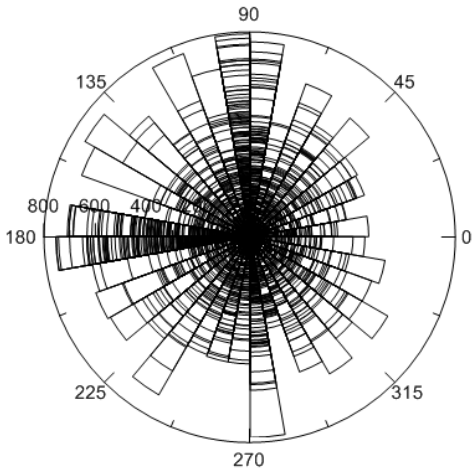

Figure 4-138 Shear force at 2 % axial strain

4.6.6 Effect of 3 layers of geogrid in clump samples

Similar to circular samples, a biaxial sample of clump particles were reinforced with three geogrid layers dividing the sample into four equal parts. The sample was then loaded at the optimum loading rate of 0.005 m/s at the confinement of 100 kPa and flexible boundary. The three layers of geogrid provided the highest peak deviatoric stress of more than 300 kPa as shown in Figure 4-139 and Figure 4-140. Since the stress-strain behavior of the sample changed, Figure 4-140 shows the peak deviatoric stress and beyond the point of occurrence of peak deviatoric stress. Additionally, the sample behaved as a dense soil with volumetric dilation beginning at the very start of loading state as shown in Figure 4-141.

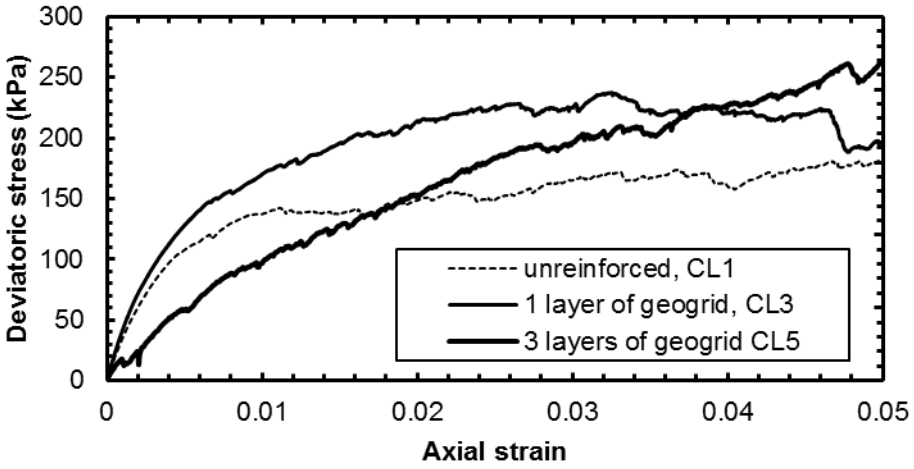

Figure 4-139 Deviatoric stress vs axial strain for three layers of geogrid reinforcement for clump particles

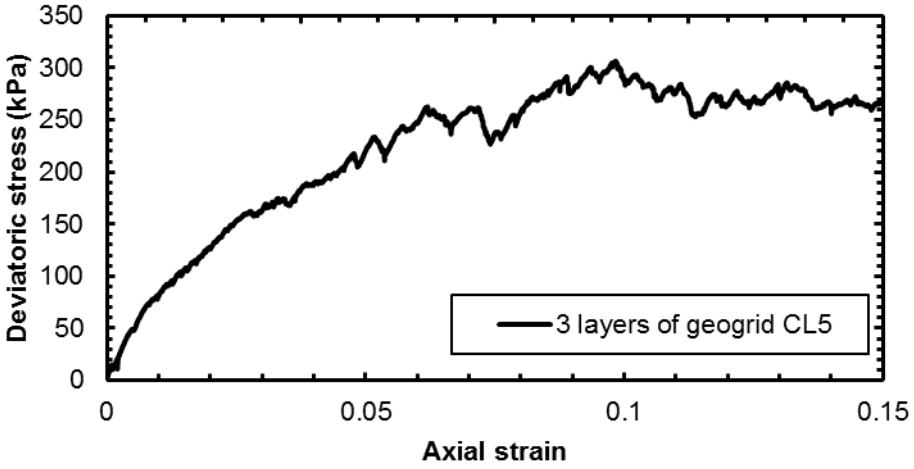

Figure 4-140 Deviatoric stress vs axial strain for three layers of geogrid reinforcement for clump particles beyond peak deviatoric stress

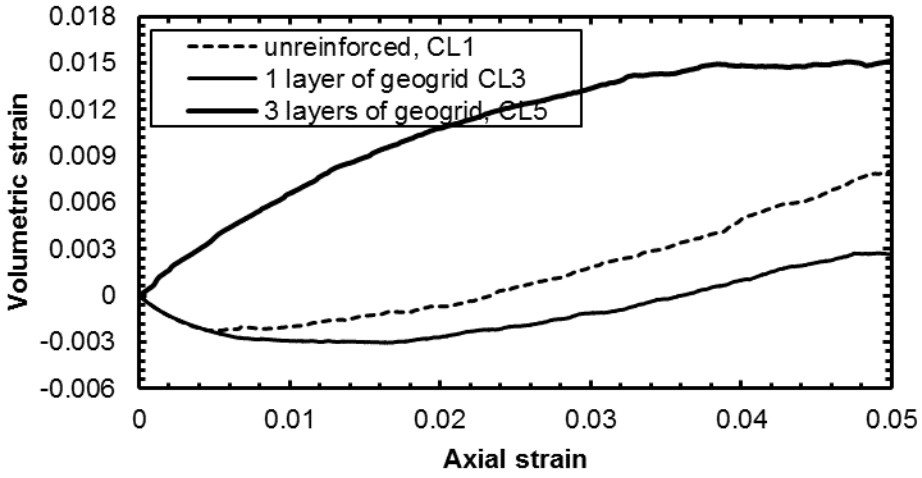

Figure 4-141 Volumetric strain vs axial strain for three layers of geogrid reinforcement for clump particles

Similarly, in Figure 4-142 we can observe there is not much difference in terms of boundary work but also in frictional work for 3 layers of geogrid resistance. However, the peak deviatoric stress in the three layers geogrid reinforced sample occurs only at much higher strain of 10 %. Hence, Figure 4-143 shows the boundary and frictional work of the sample up to 15 % axial strain. Based on the values of boundary and frictional work presented in Table 4-4 it can be concluded that ultimately at 10 % of axial strain the boundary and frictional work of the sample will be much higher than that of only one layer of reinforcement or no reinforcement at all. This concludes that the shear strength of the clump particle assembly increased with increasing number of geogrid layer reinforcements.

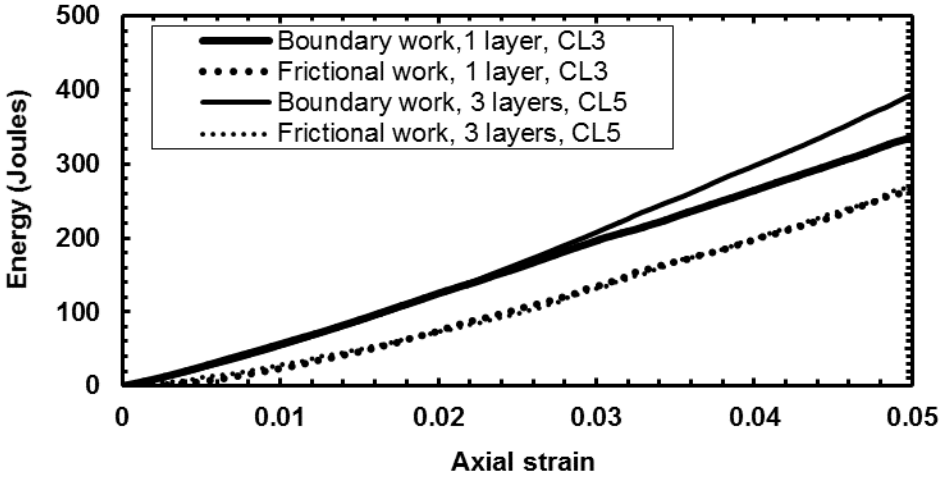

Figure 4-142 Boundary and frictional work for three layers of reinforcement

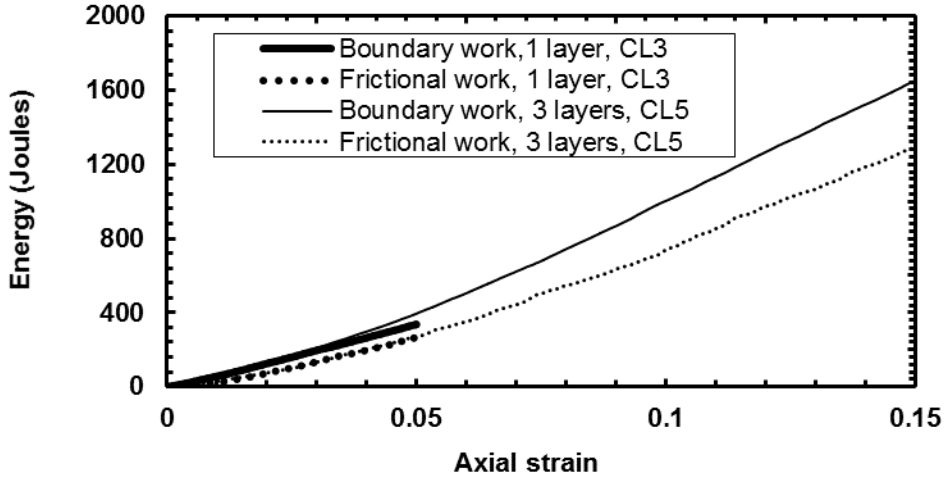

Figure 4-143 Boundary and frictional work for three layers of reinforcement up to 15 % axial strain

4.7 Geogrid performance

The performance of geogrid reinforcement was evaluated for circular and clump samples by evaluating several criteria as describe in the following sections.

4.7.1 Reinforcement factor

Reinforcement factor is the ratio of peak deviatoric stress of reinforced sample to that of unreinforced sample. The reinforcement factors were calculated for samples with flexible boundary for faster loading rate of 0.05 m/s and optimum loading rate of 0.005 m/s for 100 kPa of confining pressure for both circular and clump particle assemblies. The following Table 4-3 summarizes the reinforcement factor.

Table 4-3 Reinforcement factors

Sample	Shape	Reinforcement	Loading rate (m/s)	Peak strength (kPa)	Reinforcement factor
C2	Circular	None	0.05	140	1.31
C4	Circular	1 layer	0.05	184	
C1	Circular	None	0.005	108	1.09
C3	Circular	1 layer	0.005	118	
C1	Circular	None	0.005	108	1.30
C15	Circular	3 layers	0.005	140	
CL2	Clump	None	0.05	180	1.55
CL4	Clump	1 layer	0.05	280	
CL1	Clump	None	0.005	143	1.33
CL3	Clump	1 layer	0.005	190	
CL1	Clump	None	0.005	143	2.14
CL5	Clump	3 layers	0.005	306	

The reinforcement factor for single layer of geogrid reinforcement for the circular particles was only 1.09 for the optimum loading rate of 0.005 m/s. However, for faster loading rate of 0.05 m/s the factor was 1.3. Similar reinforcement factor for the circular particles was obtained using optimum loading rate but with three geogrid layers of

reinforcement. The clump particle assembly provided reinforcement factor of 1.33 for single layer of geogrid reinforcement with flexible boundary and loaded at optimum rate of 0.005 m/s. When loaded at faster rate of 0.05 m/s the sample provided the highest reinforcement factor. The highest reinforcement factor of 2.14 was provided by clump particle assembly reinforced with 3 layers of geogrid loaded at the optimum rate of 0.005 m/s.

A comparison between the experimental and numerical simulations results for stress vs strain is shown in Figure 4-144 for circular particles. The results compares the experimental results from unreinforced and reinforced glass bead with 2D simulation results of circular particle assemblies loaded at optimum loading rate and with flexible boundary with no, one, and three layers of geogrid reinforcement.

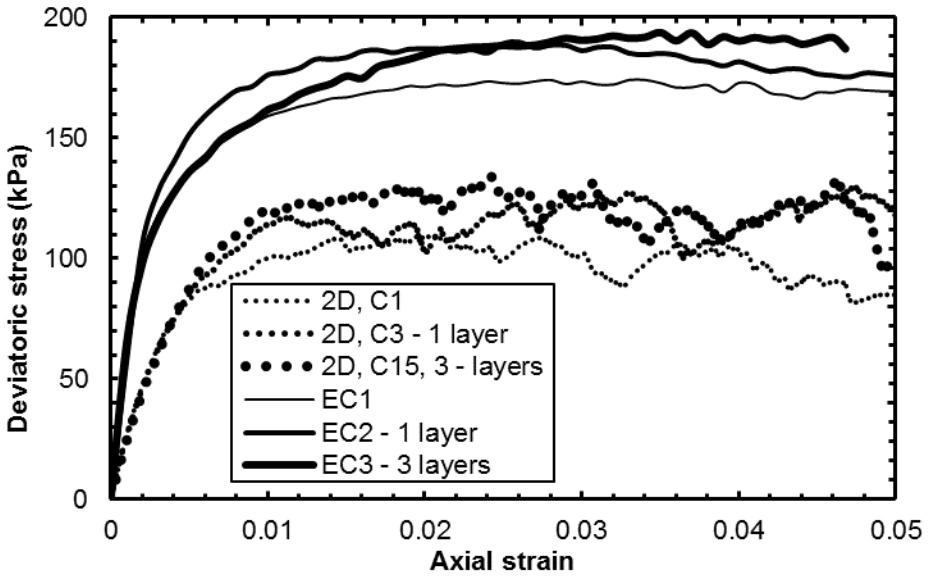

Figure 4-144 Comparisons of experimental and numerical results for circular particles

Similar comparison is showed for experimental test results for clump particles and 2D DEM models in Figure 4-145. The experimental tests for clump particles were performed only at low confining pressure of 50 kPa due to excessive breakage which was

not in the scope of modeling. Although the confinements used in the experimental and numerical tests were different the stress vs strain relationship can be used to understand the behavior.

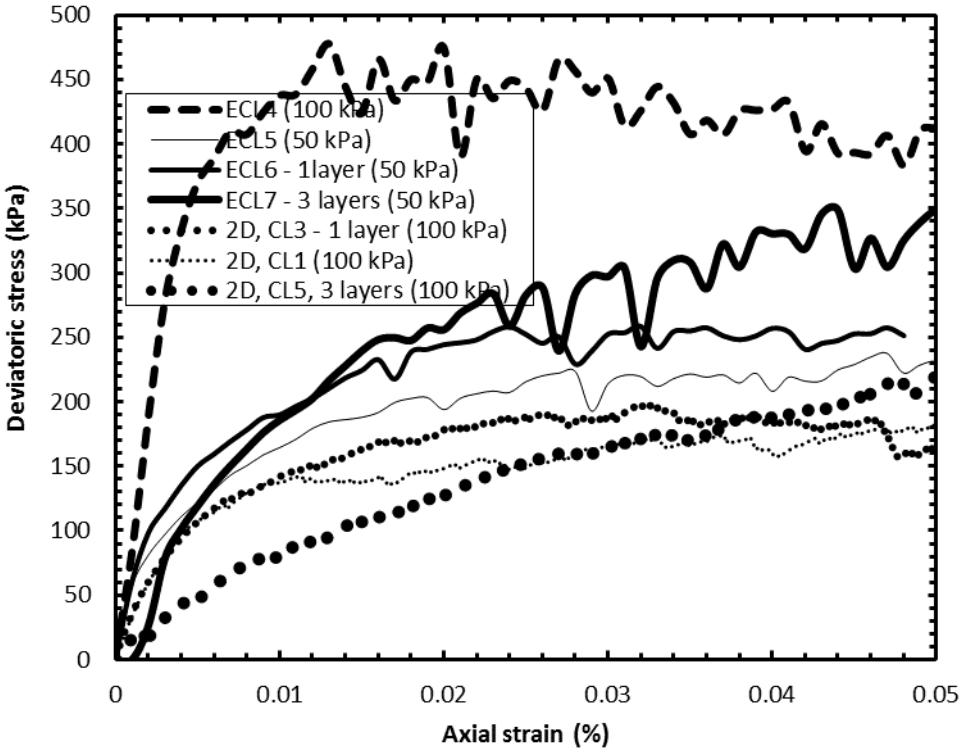

Figure 4-145 Comparisons of experimental and numerical results for clump particles

4.7.2 Lateral strain

The lateral strain at the mid height of reinforced and unreinforced circular sample with flexible boundary loaded at optimum rate was recorded and is presented in Figure 4-146. The geogrid reduced the lateral strain at the mid height considerably. Figure 4-146 shows the average wall displacement profile for the reinforced sample C3 at various axial strains.

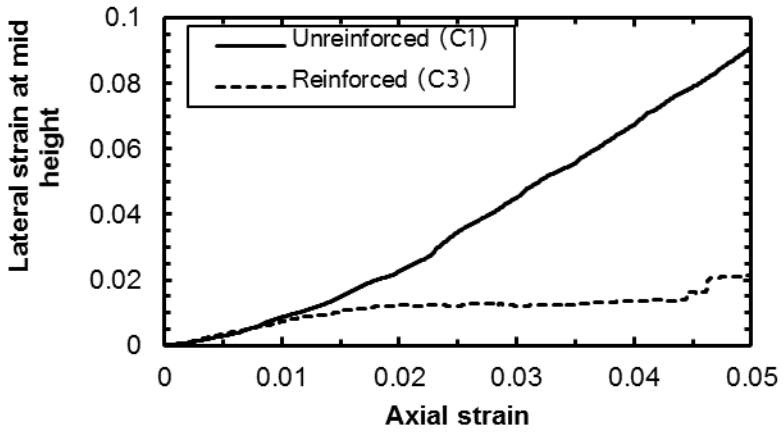

Figure 4-146 Lateral strain for reinforced and unreinforced circular sample at 100 kPa confinement

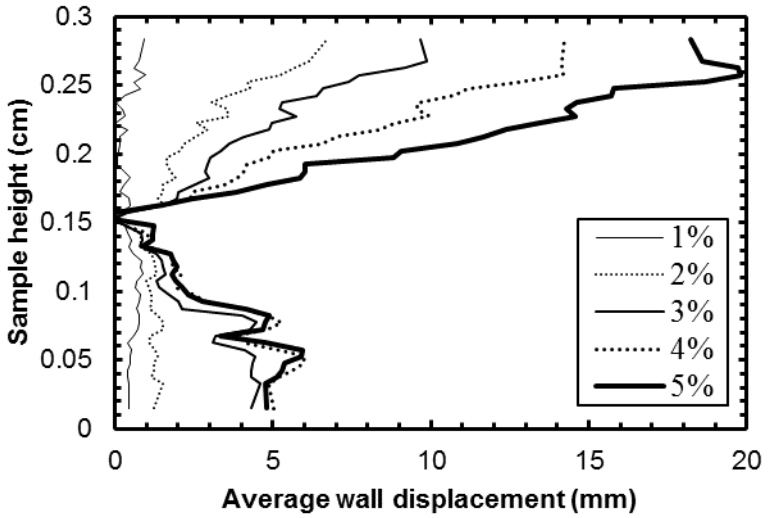

Figure 4-147 Average lateral wall movement (Sample C3)

4.7.3 Geogrid tension

The tension force developed in the geogrid in sample C3 was monitored at several locations during the loading phase as shown in Figure 4-148. The locations of such measurement points were measure from left to right and lied between nodes. Initially some portions of the geogrid were in compression due to sample preparation

method and confining pressure. As the axial strain increased major portions of the geogrid were intension.

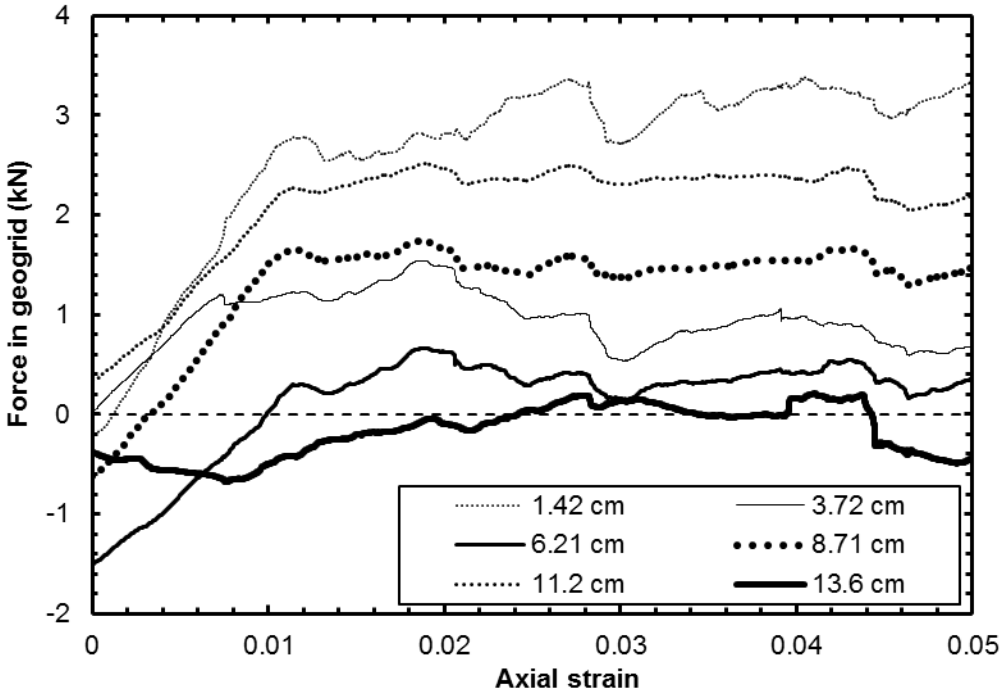

Figure 4-148 Tension force development in geogrid, sample C3

4.7.4 Failure mode

Figure 4-149 to Figure 4-154 are particle rotation contour maps. The x and y coordinates of particles are along x and y axis respectively and the accumulated rotations are the z values. In unreinforced sample C1 the particles along the diagonal of the sample showed maximum rotations forming a 'X' region represented by dark colors in Figure 4-149. These are the developments of shear bands along which the sample shears. Such shear bands have relatively high porosity as shown in Figure 4-31. Due to introduction of geogrid the particle rotations were greatly reduced shown my region

marked by oval dashed red line in Figure 4-150. The shear bands move up to the upper portion of the sample.

Some further modifications were done on the samples C1 and C3 to study the formation of shear bands as follows. The sample C1 at equilibrium was densified by setting the surface friction coefficient and shear stiffness value of the particles to zero. In the next stage servo control was applied and the friction and stiffness values were set back to the original values before loading. Similar adjustments were done for the reinforced sample C3. The particle rotation contour maps for the derivative samples are shown in Figure 4-151 and Figure 4-150. The shear bands in the reinforced and unreinforced samples are more distinct as compared to the original sample C1 and C3.

Similar results were observed in clump particles too as shown in Figure 4-153 and Figure 4-153. However, the intensities of particle rotations are much smaller compared to circular sample represented by lower density of dark colored spots along the shear bands.

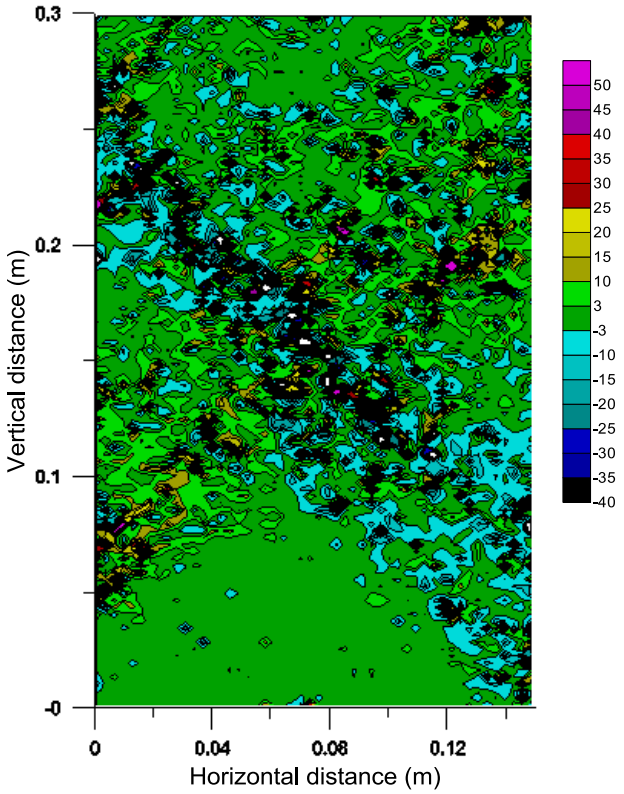

Figure 4-149 Rotation contour map, sample C1

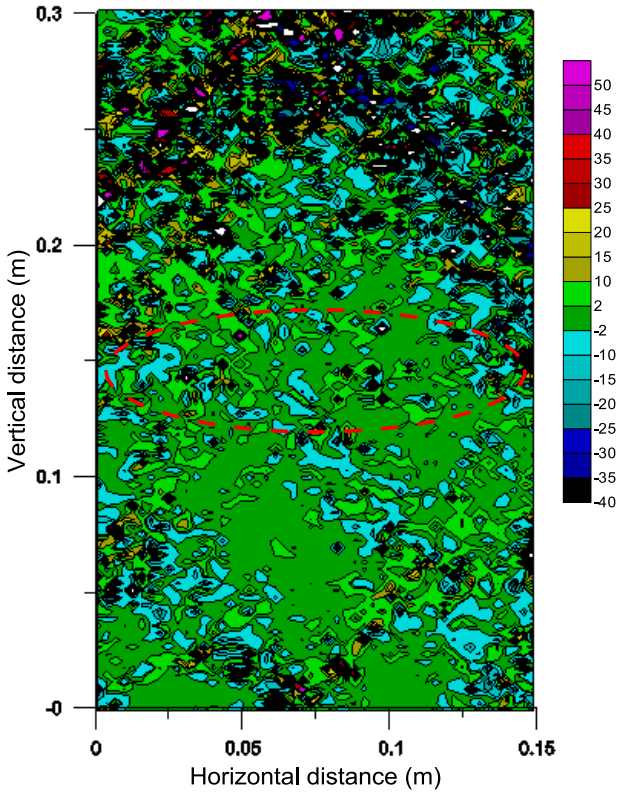

Figure 4-150 Rotation contour map, sample C3

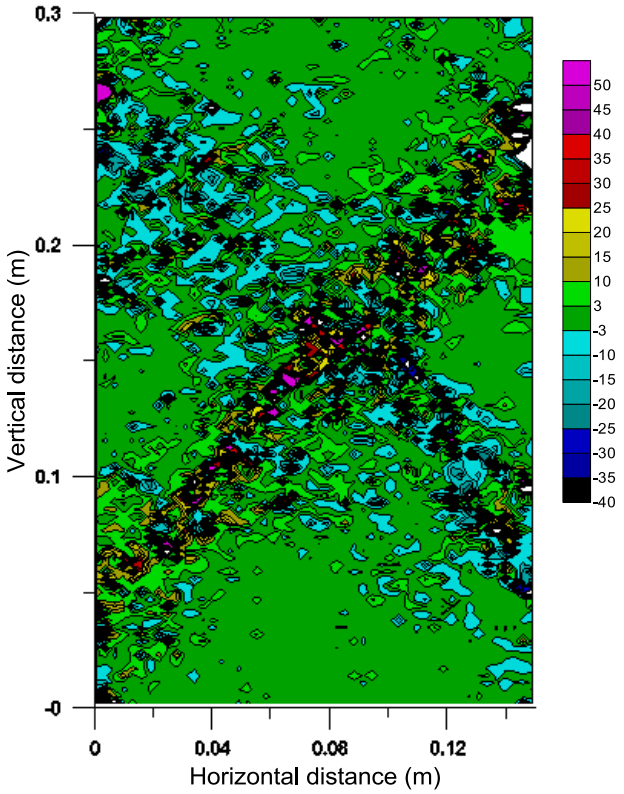

Figure 4-151 Rotation contour map, densified sample C1

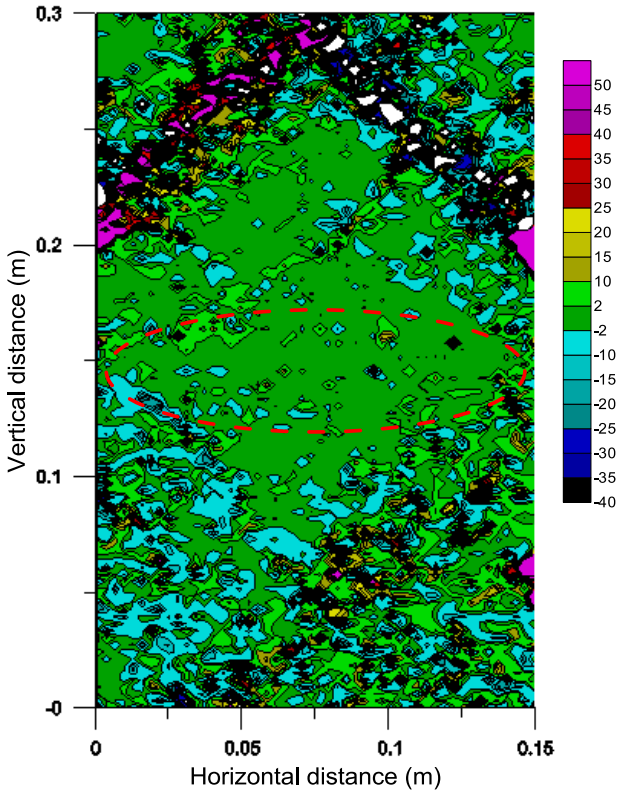

Figure 4-152 Rotation contour map, densified sample C3

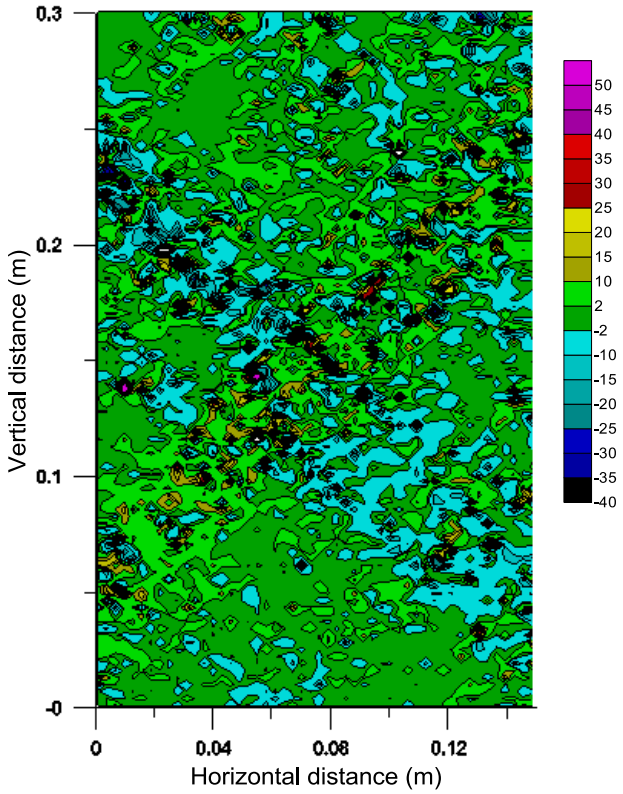

Figure 4-153 Rotation contour map, sample CL1

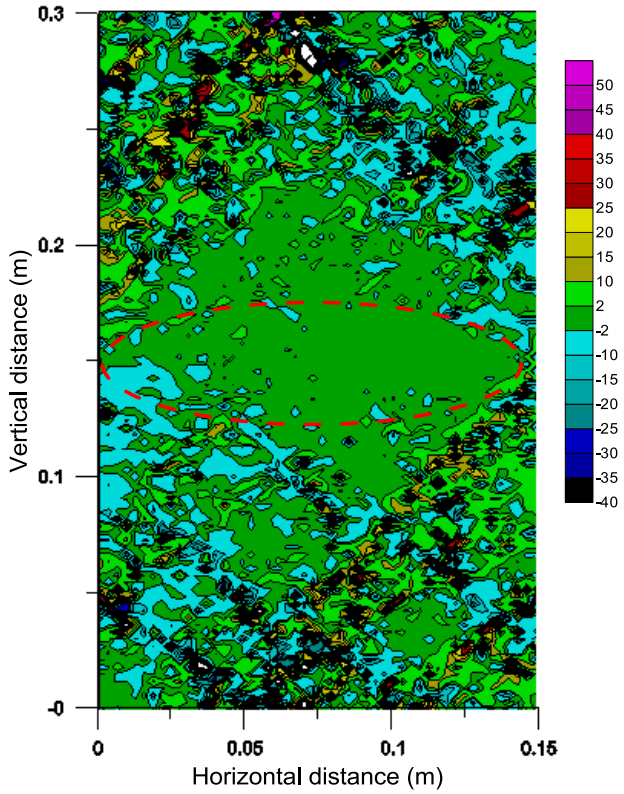

Figure 4-154 Rotation contour map, sample CL3

4.8 Summary

2D DEM samples were generated with and without reinforcement to study effect of parameters such as loading rate, flexible and rigid boundary, and effect of particle shape. First, the effect of these parameters were tested on unreinforced samples to understand the results. Then the study was then expanded to include geogrid reinforced samples to study possible effects and deviation of their behavior from unreinforced samples if any.

Faster loading rate resulted in higher deviatoric stresses in both reinforced and unreinforced circular samples. The amplification of higher deviatoric stress by faster loading rate was even higher in unreinforced and reinforced clump particles. Such effect was evaluated by calculating reinforcement factors presented in Table 4-3. The table shows that the reinforcement factor for the reinforced clump particles was the highest with the fastest loading rate and lowest for the reinforced circular particles loaded at optimum loading rate. In call cases faster loading rate produced higher reinforcement factors. However such improvement in reinforcement factor due to faster loading rate is fictitious. Under faster loading rate the circular and clump particles experienced higher normal contact stress with increase in boundary work but the shear strength of the particle assemblies did not increase. Polar plots of normal forces and shear forces also showed that normal forces increased with increase in loading rate but the shear force diagrams did not show any significant differences. Table 4-4 summarizes and presents energy dissipated in the form of boundary work and frictional work and can be used to evaluate boundary and frictional work across particle assemblies using parameters of loading rate, boundary type, and presence of reinforcement. Any increase in shear strength of particle assembly should be accompanied by increase in energy dissipated

due to frictional work. Table 4-4 shows that although increase in boundary work increased with loading rate the frictional work did not increase for any similar pair of samples whether reinforced or unreinforced such as in samples C1 and C2, and C3 and C4, . However, the frictional work did increase significantly with the presence of geogrid when compared between samples C1 and C3, CL1 and CL3.

Table 4-4 Energy dissipation

Sample	Boundary	Reinforcement	Loading	Boundary work (Joules)	Frictional work (Joules)
C1	Flexible	No	0.005	184	149
C2	Flexible	No	0.05	247	154
C3	Flexible	Yes	0.005	220	163
C4	Flexible	Yes	0.05	329	172
C10	Rigid	No	0.005	181	145
C13	Rigid	Yes	0.005	227	174
C15	Flexible	3 layers	0.005	245	192
CL1	Flexible	No	0.005	290	233
CL2	Flexible	No	0.05	355	244
CL3	Flexible	Yes	0.005	336	266
CL4	Flexible	Yes	0.05	412	282
CL5	Flexible	3 layers	0.005	395	269

Any loading rate faster than optimum loading rate produced smaller volumetric strain in unreinforced circular sample as shown in Figure 4-22. For the case of reinforced circular samples the loading rate did not have any significant effect in terms of volumetric

dilation. However, the volumetric dilation of reinforced circular samples were always smaller than the unreinforced samples in all the cases.

The effect of boundary on unreinforced circular samples were tested in confining pressures of 50 kPa, 100 kPa, 400 kPa, and 1000 kPa and no significant difference due to boundary were found. Whether flexible or rigid boundary was used the stress-strain behavior of circular samples for both reinforced and unreinforced case did no vary significantly except for slight deviation. This is also supported by small difference in frictional work done shown in Table 4-4 when compared between samples C1 and C10, and C3 and C13 but the difference are small enough to assert that the shear strength of the particle assemblies did not change. The polar plot of normal and shear forces in such boundary conditions for unreinforced circular sample assemblies essentially remained the same. Such was the case for polar plot of normal and shear forces in reinforced circular samples too with rigid and flexible boundary.

The boundary did not have any effect on the volumetric dilation behavior of the unreinforced circular samples in the tested confining pressure range. However, the sample with flexible boundary was able to develop diagonally aligned region of relatively lower porosity in the unreinforced sample representing shear band as shown in Figure 4-68. In the case of reinforced circular samples the volumetric dilation in rigid boundary were significantly higher than in flexible boundary at low confining pressures of 50 kPa and 100 kPa. The porosity contour of the reinforced sample with rigid boundary in Figure 4-83 shows that the sample developed larger area of relatively higher porosity than its counterpart with flexible boundary shown in Figure 4-47 at 100 kPa of confinement and 4.5 % of axial strain.

The higher deviatoric stresses in clump particle assemblies loaded at optimum rate were due to higher energy dissipation due to frictional work which is presented in

Table 4-4. The higher energy dissipation in frictional work is due to the interlocking of the clump particles between each other due to their angularity. The higher shear forces in unreinforced clump particles due to interlocking can be seen when comparing polar shear force diagrams shown in Figure 4-36 and Figure 4-104. Figure 4-104 shows higher values of shear forces in the particle assembly. The frictional work was even higher in reinforced clump particles loaded at the same optimum rate as can be seen in Table 4-4. Also, the reinforcement factor as presented in Table 4-3 is 1.33 which is higher than reinforced circular samples with the value of 1.09. Hence, clump particles by the virtue of their angularity showed higher increase in their shear strength due to geogrid reinforcement than circular particles.

The reinforcement factor for clump particles was the highest for the faster loading rate of 0.05 m/s. However the frictional work did not increase due to faster loading rate. Additionally the polar shear force diagram from Figure 4-120 to Figure 4-123 did not show any difference between the faster and optimum loading rates except for some single spikes.

The unreinforced clump particle assemblies showed insignificant differences in terms of volumetric strain due to loading rates but the sample loaded at optimum rate developed a diagonal region of relatively lower porosity representing shear band as shown in Figure 4-96. The volumetric dilation of reinforced clump particles were always smaller for all loading rates compared to unreinforced clump particles as compared between Figure 4-96 and Figure 4-115 but the assembly loaded at optimum loading rate showed higher volumetric dilation than the assembly loaded at faster loading rate.

Particle rotations in rigid boundary were uniform throughout the sample height in unreinforced circular particles whereas particles around mid-height showed increased rotation with flexible boundary. The particle rotations were highly reduced due to geogrid

reinforcement in circular particles. Also faster loading rate in circular particles caused reduced particle rotations. The clump particles showed much smaller particles rotations than circular particles for both reinforced and unreinforced case. Similar behavior was observed in clump particles for faster loading rate as in the case of circular particles. The reduction in particle rotation in the vicinity of geogrid for the circular and clump particles suggest that the geogrid provided some kind of interlocking mechanism.

Three layers of reinforcement was able to improve reinforcement factor in circular particle assembly with flexible boundary to 1.3 and was accompanied by increase in frictional work. The frictional work was more than that of its counterpart assembly C3 with only one layer of geogrid reinforcement. The reinforcement caused the sample to be in volumetric compression even up to 5 % axial strain. Particle rotations were found to be greatly reduced in the vicinity of the geogrid layers especially within the confinement of adjacent layers. Also the region of the assembly confined within the adjacent geogrid layers retained relatively lower porosity throughout the loading stage. In terms of shear forces, the polar plot of shear forces in Figure 4-138 showed higher shear forces than its counterpart sample C1 and C3. In the case of clump particles, the improvement in reinforcement factor was significant with three layers of geogrids and was higher than that of circular particle assembly with the same number of layers of geogrid.

Chapter 5

Conclusions and recommendations

Experimental and numerical studies in DEM were undertaken in the study to understand the reinforcement mechanism of geogrid. Laboratory tests were performed using triaxial testing of glass beads and clumped glass beads with and without reinforcement. The single glass bead assemblies were tested at 100 kPa of confinement. However, the assemblies of clumped glass beads were tested at lower confinement of 50 kPa since at higher confinement excessive breakage of clumped glass beads were observed and such particle breakage was not in the scope of this study. The results showed that clumped glass bead assemblies exhibited higher deviatoric stresses than spherical glass bead assemblies even with lower confinement. Since the clumped glass beads were the same material of the spherical glass beads but only joined together, the results point that relatively angular materials provide higher strength in quasi static compression. When geogrid reinforcement was used both assemblies of spherical glass beads and clumped glass beads showed improvement however, the improvement was more significant in clumped glass beads. The improvement was evaluated by calculating reinforcement factor. Additionally the reinforcement effect increased with 3 layers of geogrid reinforcement than just one layer in the experimental testing. The results show that geogrid reinforcement is more effective in relatively angular material.

The numerical study revealed several important factors and mechanism of geogrid reinforcement in 2D DEM samples. Faster loading rate produced higher deviatoric stresses in circular as well as in clumped particle assembly both in reinforced and unreinforced samples. The increase in deviatoric stress due to faster loading rate was much higher in clump particles than in circular particles. Such increase in deviatoric

stress was analyzed at micro level by looking into individual normal and shear forces acting on each particle and by considering energy considerations. Faster loading rate showed higher normal contact forces but did not show higher shear forces in the particles in both the reinforced and unreinforced circular and clump particles. Any increase in peak deviatoric would have to be accompanied by increase in shear strength of the sample for true increase in strength. To examine the phenomenon further analysis was performed by monitoring the work done by boundary walls on the sample and the energy dissipated at particle contacts due to frictional slip. The results showed that although boundary work increased with faster loading rate the frictional energy dissipated remained almost constant. Hence the increase in deviatoric stress due to faster loading rate was not the result of increase in shear strength of the sample assemblies. Hence optimum loading rate of an assembly should be determined prior to studying effect of geogrid reinforcement or any numerical study for that matter.

The effect of flexible and rigid boundary was studied on circular samples for both unreinforced and reinforced cases. Flexible and rigid boundary did not have any effect on in both unreinforced and reinforced case in terms of deviatoric stresses. However, reinforced circular particles showed higher volumetric dilation with rigid boundary than with flexible boundary at low confining pressures of 50 kPa and 100 kPa. Additionally, the porosity contour maps for assemblies at 100 kPa confinement showed development of shear bands in the samples with flexible boundary. Hence, boundary type might not be important factor to be considered while studying bulk behavior but are favorable for studying localization like shear bands.

Particle shape played important role in the numerical model. Clumped particles showed reduced particle rotation than circular particles and also higher deviatoric stresses. Such was the case for both reinforced and unreinforced samples. The higher

deviatoric stresses were accompanied by higher energy dissipation due to frictional work. Also, higher reinforcement factor in clumped particles suggested that geogrid performance is better in relatively angular particles than in circular particles. The numerical result was supported by similar trend observed in the experimental testing.

Reinforcement factor was calculated to study performance of geogrid. The reinforcement factor increased with increase in layers of geogrid reinforcement in both circular and clumped particles in experimental and numerical model. In both types of studies the geogrid reinforcement factor was higher in clumped particles than in circular particles. Presence of geogrid reduced particle rotations significantly in the vicinity of geogrid in both circular and clump particles in the numerical model thereby exhibiting interlocking effect. Geogrid also caused shear band to shift its position in circular and clump particle assemblies. Additionally, the lateral strain and average boundary wall movements were greatly reduced at the locations of geogrid.

Further studies in 3D DEM model for fully understanding the geogrid performance and reinforcement mechanism are undergoing at the moment. The 3D DEM models are being calibrated to the results from the experimental studies of glass beads and clumped glass beads.

References

Abu-Farsakh, M., Souci, G., Voyiadjis, G., and Chen, Q. (2012). "Evaluation of Factors Affecting the Performance of Geogrid-Reinforced Granular Base Material Using Repeated Load Triaxial Tests." *Journal of Materials in Civil Engineering*, 24(1), 72-83.

Abu-Farsakh, M. Y., and Chen, Q. (2011). "Evaluation of geogrid base reinforcement in flexible pavement using cyclic plate load testing." *International Journal of Pavement Engineering*, 12(3), 275-288.

Abu-Farsakh, M. Y., and Nazzal, M. (2009). "Evaluation of the Base/Subgrade Soil under Repeated Loading." Louisianan Transportation Research Center, Baton Rouge, 1-139.

Al-Quadi, I., Tutumluer, E., and Dessouky, S. "Construction and Instrumentation of Full-Scale Geogrid-Reinforced Flexible Pavement Test Sections." *Airfield and Highway Pavement*, 131-142.

Arulrajah, A., Rahaman, M., Piratheepan, J., Bo, M., and Imteaz, M. (2014). "Evaluation of Interface Shear Strength Properties of Geogrid-Reinforced Construction and Demolition Materials Using a Modified Large-Scale Direct Shear Testing Apparatus." *Journal of Materials in Civil Engineering*, 26(5), 974-982.

Bakeer, R. M., Sayed, S. M., Cates, P., and Subramanian, R. (1998). "Pullout and shear tests on geogrid reinforced lightweight aggregate." *Geotextiles and Geomembranes*, 16(2), 119-133.

Brown, S. F., Kwan, J., and Thom, N. H. (2007). "Identifying the key parameters that influence geogrid reinforcement of railway ballast." *Geotextiles and Geomembranes*, 25(6), 326-335.

Chen, C., McDowell, G. R., and Thom, N. H. (2012). "Discrete element modelling of cyclic loads of geogrid-reinforced ballast under confined and unconfined conditions." *Geotextiles and Geomembranes*, 35(0), 76-86.

Chen, X., Zhang, J., and Li, Z. (2014). "Shear behaviour of a geogrid-reinforced coarse-grained soil based on large-scale triaxial tests." *Geotextiles and Geomembranes*, 42(4), 312-328.

Cheng, Y. P., Nakata, Y., and Bolton, M. D. (2003). "Discrete element simulation of crushable soil." *Géotechnique*, 633-641.

Cheung, G., and O'Sullivan, C. (2008). "Effective simulation of flexible lateral boundaries in two- and three-dimensional DEM simulations." *Particuology*, 6, 483-500.

Chung, Y. C., and Ooi, J. Y. (2007). "Influence of Discrete Element Model Parameters on Bulk Behavior of a Granular Solid under Confined Compression." *Particulate Science and Technology*, 26(1), 83-96.

Di Renzo, A., and Di Maio, F. P. (2004). "Comparison of contact-force models for the simulation of collisions in DEM-based granular flow codes." *Chemical Engineering Science*, 59(3), 525-541.

Ferellec, J.-F., and McDowell, G. (2010). "A method to model realistic particle shape and inertia in DEM." *Granular Matter*, 12(5), 459-467.

Geosynthetics (2015). "Geosynthetics ", <http://www.geosyn.co.uk/product/Details/tenax-geogrids/56e9c373-7f43-419f-972f-3490071cd727>. (23/7/2015, 2015).

Holtz, R. D., Christopher, B. R., and Berg, R. R. (1998). *Geosynthetic Design and construction guidelines*.

Indraratna, B., Ionescu, D., and Christie, H. (1998). "Shear Behavior of Railway Ballast Based on Large-Scale Triaxial Tests." *Journal of Geotechnical and Geoenvironmental Engineering*, 124(5), 439-449.

Indraratna, B., Thakur, P., Vinod, J. (2010). "Experimental and Numerical Study of Railway Ballast Behavior under Cyclic Loading." *International Journal of Geomechanics*, 10(4), 136-144.

Itasca Consulting Group , I. 2008. 3DEC (3-Dimensional Distinct Element Code), version 4.0, Minneapolis.

Jersey, S. R., Tingle, J. S., Norwood, G. J., Kwon, J., and Wayne, M. (2012). "Full-Scale Evaluation of Geogrid-Reinforced Thin Flexible Pavements." *Transportation Research Record: Journal of the Transportation Research Board*, 2310(1), 61-71.

Johnstone, M. W. (2010). "Calibration of DEM models for granular materials using bulk physical tests." Doctoral, The University of Edinburgh, Edinburgh.

Koerner, R. M. (2005). *Designing with Geogrids*, Pearson Prentice Hall, New Jersy.

Konietzky, H., Kamp, L. t., Groeger, T., and Jenner, C. (2004). "Use of DEM to model the interlocking effect of geogrids under static and cyclic loading." *Numerical modeling in micromechanics via particle methods*, 3-11.

Lanier, J., and Jean, M. (2000). "Experiments and numerical simulations with 2D disks assembly." *Powder Technology*, 109(1–3), 206-221.

Litertystone (2015). "8 & Under wall program." <http://liberty-stone.net/8-under-program.html>. (23/7/2015, 2015).

Liu, N., and Zhang, C. S. (2011). "Simulation on influence of different loading rates on Jinping marble in uniaxial compression test by PFC2D." *Rock Mechanics: Achievements and Ambitions*, CRC Press, 327-329.

Lu, M., and McDowell, G. R. (2010). "Discrete element modelling of railway ballast under monotonic and cyclic triaxial loading." *Géotechnique*, 459-467.

Markauskas, D., and Kačianauskas, R. (2006). "Compacting of particles for biaxial compression test by the discrete element method." *Journal of Civil Engineering and Management*, 12(2), 153-161.

McDowell, G., Harireche, O., Konietzky, H., Brown, S., and Thom, N. (2006). "Discrete element modelling of geogrid-reinforced aggregates." *Proceedings of the ICE-Geotechnical Engineering*, 159(1), 35-48.

Moraci, N., and Recalcati, P. (2006). "Factors affecting the pullout behaviour of extruded geogrids embedded in a compacted granular soil." *Geotextiles and Geomembranes*, 24(4), 220-242.

O'Sullivan, C. (2011). "Particle-Based Discrete Element Modeling: Geomechanics Perspective." *International Journal of Geomechanics*, 11(6), 449-464.

Palmeira, E. M. (1987). "The study of soil-reinforcement interaction by means of large scale laboratory tests." PhD, University of Oxford, UK.

Perkins, S. W. (1999). "Mechanical Response of Geosynthetic-Reinforced Flexible Pavements." *Geosynthetics International*, 347-382.

Qian, Y., Han, J., Pokharel, S., and Parsons, R. (2013). "Performance of Triangular Aperture Geogrid-Reinforced Base Courses over Weak Subgrade under Cyclic Loading." *Journal of Materials in Civil Engineering*, 25(8), 1013-1021.

Rothenburg, L., and Bathurst, R. J. (1992). "Micromechanical features of granular assemblies with planar elliptical particles." *Géotechnique*, 79-95.

Schuettpelz, C., Fratta, D., and Edil, T. B. (2009). "Evaluation of the zone of influence and stiffness improvement from geogrid reinforcement in granular materials." *Journal of the Transportation Research Board*, 76-84.

Tannant, D. D., and Wang, C. (2007). "DEM boundary conditions for modeling uniaxial and biaxial tests." *Rock Mechanics*, 385-392.

Tensar (2015). "Rail Track Support." <http://www.tensar.co.uk/Applications/Rail-Track-Support#>. (3/7/2015, 2015).

Thomas, P. A., and Bray, J. D. (1999). "Capturing Nonspherical Shape of Granular Media with Disk Clusters." *Journal of Geotechnical and Geoenvironmental Engineering*, 125(3), 169-178.

Ting, J., Corkum, B., Kauffman, C., and Greco, C. (1989). "Discrete Numerical Model for Soil Mechanics." *Journal of Geotechnical Engineering*, 115(3), 379-398.

Tutumluer, E., Huang, H., and Bian, X. (2012). "Geogrid-Aggregate Interlock Mechanism Investigated through Aggregate Imaging-Based Discrete Element Modeling Approach." *International Journal of Geomechanics*, 12(4), 391-398.

Vinod, J. S., Nagaraja, S., Sitharam, T. G., and Dinesh, S. V. (2011). "Numerical Simulation of reinforced granular soils using DEM." *Geo-Frontiers*, 4242-4250.

Wilson-Fahmy, R., Koerner, R., and Harpur, W. (1995). "Long-Term Pullout Behavior of Polymeric Geogrids." *Journal of Geotechnical Engineering*, 121(10), 723-728.

Xu, X., and Pradhan, A. (2014). "Study of Geogrid Reinforcement Using Two-Dimensional Discrete Element Method." *Ground Improvement and Geosynthetics*, 299-311.

Zhang, J., Yasufuku, N., and Ochiai, H. (2009). "Discrete Element Modelling of Geogrid Pullout Test." *Geosynthetics in Civil and Environmental Engineering*, G. Li, Y. Chen, and X. Tang, eds., Springer Berlin Heidelberg, 11-14.

Zhu, H. P., Zhou, Z. Y., Yang, R. Y., and Yu, A. B. (2007). "Discrete particle simulation of particulate systems: Theoretical developments." *Chemical Engineering Science*, 62(13), 3378-3396.

Zhu, H. P., Zhou, Z. Y., Yang, R. Y., and Yu, A. B. (2008). "Discrete particle simulation of particulate systems: A review of major applications and findings." *Chemical Engineering Science*, 63(23), 5728-5770.

Zornberg, J., and Gupta, R. "Geosynthetics in pavements: North American contributions."

Biographical Information

Asheesh Pradhan was born in Lalitpur district of Nepal, a south Asian country situated between India and China. He graduated with Bachelors of Civil Engineering in 2004 from Institute of Engineering under prestigious Tribhuvan University in Nepal. He immediately joined the civil engineering industry and lunched himself into professional practice working in diverse projects involving building and water resource infrastructures until 2007.

In pursuit of higher education, he started his Masters in Civil Engineering at McNeese State University, Lake Charles, Louisiana in the spring of 2008 and graduated in fall of 2009. After brief stint in voluntary work he then pursued his doctoral degree in Civil Engineering at University of Texas at Arlington in the fall of 2011 and successfully defended his thesis on April of 2015. During his doctoral studies he worked under the guidance of supervising Professor Dr. Xinbao Yu and also worked as teaching assistant for Dr. Anand Puppala. Mr. Pradhan successfully publishes several technical papers.